REPORT ON RESEARCH ACTIVITIES FOR THE QUARTER JULY 1 THROUGH SEPTEMBER 30, 1990

Prepared for

Nuclear Regulatory Commission
Contract NRC-02-88-005

Prepared by

Center for Nuclear Waste Regulatory Analyses
San Antonio, Texas

November 1990

REPORT ON RESEARCH ACTIVITIES FOR THE QUARTER JULY 1 THROUGH SEPTEMBER 30, 1990

Prepared for

Nuclear Regulatory Commission
Contract NRC-02-88-005

Edited by

Wesley C. Patrick

**Center for Nuclear Waste Regulatory Analyses
San Antonio, Texas**

November 1990

TABLE OF CONTENTS

TABLE OF CONTENTS (Cont'd)

iii

TABLE OF CONTENTS (Cont'd)

TABLE OF CONTENTS (Cont'd)

APPENDICES

  A Fine-Scale Spatial-Statistical Distributions and Correlations:
      Effects of Cross-Correlations Between Intercept and Slope of
      Unsaturated Log-Conductivity Field
          by R. Ababou

  B Identification of Effective Conductivity Tensor in Randomly
      Heterogeneous and Stratified Aquifers
          by R. Ababou

LIST OF FIGURES

LIST OF FIGURES (Cont'd)

LIST OF FIGURES (Cont'd)

LIST OF TABLES

ACKNOWLEDGMENTS

1. EXECUTIVE SUMMARY

1.1 INTRODUCTION

This is the third in a series of research quarterly reports which document and make available to the technical community work that has been undertaken by the Center for Nuclear Waste Regulatory Analyses (Center) as part of its contract with the U.S. Nuclear Regulatory Commission (NRC). Reports will be prepared each calendar quarter, with the fourth such report each year constituting the annual progress report.

Each of the research projects discussed here is being conducted in accordance with approved Research Project Plans, which were developed in response to research needs identified by the NRC and the Center. These Plans are the vehicle for establishing the objectives, technical approach, justification, and funding for each of the studies. In addition, the Project Plans describe the interrelationships among the various projects which provide sound basis for integrating research results. Because the Plans address primarily planning and management matters, they are not discussed further here (with the exception of objectives).

In reading this report, it is important to realize that several of the projects have recently been approved. Consequently, there is relatively little work to report at this time. In such cases, this quarter's report provides basic information on the objectives of the new projects as well as early activities such as literature assessments. Other projects have been in progress long enough that significant technical progress in laboratory, calculational, or field studies can be reported.

This report is organized to provide, first, an Executive Summary that documents in capsule form the progress of each research project over the past quarter. The Executive Summary is followed by Chapters 2-7 representing respectively each of the six currently active research projects. Project objectives and a report of research activities and results (as appropriate) to date are given in each chapter.

1.2 UNSATURATED MASS TRANSPORT (GEOCHEMISTRY)

1.2.1 Experimental Studies

A major geologic feature potentially affecting the suitability of Yucca Mountain, Nevada, as a repository site for high-level nuclear wastes is the presence of thick lateral zones of zeolitic tuffs. Because of their sorptive properties, zeolites could provide important geologic barriers to migration of radionuclides away from the repository to the accessible environment. To support the NRC's high-level waste (HLW) program, the Center is conducting experimental studies on the thermodynamic and ion exchange properties of zeolites under Task 3 of the Geochemistry Research Project. These studies are designed to generate data needed to evaluate the effectiveness of zeolitic tuffs as barriers to radionuclide migration.

Ion exchange behavior of zeolites is a function of various parameters, including composition of the aqueous and solid phases, aqueous solution concentration, and temper-

ature. To understand the composition and concentration dependence of ion exchange between zeolites and groundwater, isotherm experiments were initiated this quarter on binary exchange reactions between clinoptilolite and aqueous solutions containing K^+, Cs^+, Ca^{2+}, or Sr^{2+}. Isotherms for the $Na^+ = K^+$, $Na^+ = Cs^+$, $2Na^+ = Ca^{2+}$, and $2Na^+ = Sr^{2+}$ exchange reactions were studied at 25°C by equilibrating nearly homoionic Na-clinoptilolite with aqueous solutions containing various equivalent mole ratios of Na^+/K^+, Na^+/Cs^+, Na^+/Ca^{2+}, and Na^+/Sr^{2+}. The dependence of isotherm shapes and exchange selectivities on aqueous solution concentration was investigated by conducting the experiments at solution normalities of 0.05 and 0.50 N (equiv/liter).

Results are given for the $Na^+ = K^+$ and $2Na^+ = Ca^{2+}$ equilibria. Initial analytical results for $Na^+ = Cs^+$ and $2Na^+ = Sr^{2+}$ showed lack of analytical precision required for generating isotherms. Thus the samples from these experiments are being reanalyzed. The isotherms for $Na^+ = K^+$ and $2Na^+ = Ca^{2+}$ indicate that the concentration dependence of the isotherm is small for exchanges involving ions of the same charge (e.g., Na^+ and K^+), while it is significant for exchanges involving ions of different valences (e.g., Na^+ and Ca^{2+}). The use of thermodynamic models in describing and predicting ion exchange equilibria will be evaluated using these and other data next quarter.

1.2.2 Geochemical Modeling

A thermodynamic analysis of the aqueous solution chemistry employed in experiments conducted as part of the CNWRA integrated waste package experiments research project (Sridhar and Cragnolino, this volume) provides an explanation for pH variations during the experiments and identifies details of the aqueous speciation at the experimental temperature of 95°C. The EQ3/6 software package was employed for the modeling calculations making use of the open-system, equilibrium (Rayleigh) gas fractionation capabilities developed in the geochemistry research project (Murphy, 1989a). The observed increases in pH were shown to be compatible with equilibrium, open-system CO_2 volatilization accompanying a small fraction of water vaporization. The calculations identified significant variations in carbonate speciation as a consequence of volatilization. Furthermore, the calculations showed that $NaSO_4^-$ was a significant species at 95°C (12 percent of total sulfate).

1.3 THERMOHYDROLOGY

Technical issues and uncertainties for the proposed Yucca Mountain HLW repository site indicate a need for research on thermohydrological phenomena, i.e., phenomena associated with heat and fluid flow, to provide information relevant to performance assessment and design criteria. The class of thermohydrological phenomena examined in this project includes phenomena driven by heat emanating from HLW emplaced in a geologic repository. Information derived principally from research is used to establish a knowledge base of thermohydrologic phenomena; the base will be used to assess models of processes used in performance assessments.

Work continued in three areas during the past quarter: experimentally, numerically, and analytically. Test 5 had provided interesting thermohydrological phenomena but did not provide sufficiently quantified results. Separate-effects experiment Test 6 has been designed and is currently being assembled. The objective of Test 6 is to perform an

experiment similar to Test 5 but with a higher level of control so as to provide more meaningful resulting data for analysis and comparison with analytical results and numerical simulations.

Preliminary results of the numerical simulations accomplished using a modified version of the TOUGH code have been obtained. It is the intention of these numerical exercises to evaluate the capabilities of TOUGH to simulate the two significant flow patterns observed in Test 5, the apparent formation of a convection cell, and the reluctance to flow across the simulated fracture under less-than-saturated conditions. The experiment was simulated using the TOUGH code for a period of about 35 days, similar to the duration of laboratory experiment Test 5. The degree of saturation was set at 65 percent and the boundary temperatures were 20° and 60°C. The simulated movement of water and water vapor responded to the effect of gravity and to effects of the constant temperature in a manner similar to that observed in the laboratory. A notable exception to this was the predicted liquid water in the elements modeled as the fracture. The amount of liquid water predicted for the fracture elements was greater than the liquid-water levels for the adjoining matrix elements. Seven hours simulation contradicted the observed results of Test 5.

The dynamic similitude analysis has been refined. Data gathered using the numerical simulations with the TOUGH code are being used to assess the various dimensionless quantities to identify those that appear to be the most sensitive. Based upon a review of the technical literature and on the observations from the earlier separate effects experiments, inclusion of several physical processes in the similitude analysis has been neglected at this time. These processes or attributes include liquid buoyancy, liquid infiltration, and viscosity. If these omissions do not prove to be prudent, they can be included in future analyses. Processes of interest that will be analyzed include vapor buoyancy, properties and number of fractures, capillarity, latent heat, and specific heat of the matrix. After this analysis, a reduced set of parameters and pi terms will have been identified. A dynamic similarity law can be formulated using these analysis.

1.4 SEISMIC ROCK MECHANICS

Seismic effects calculations performed to date on underground structures have not been subjected to an adequate level of experimental and field investigations. Computer programs are currently available to model dynamic events of underground structures in rock formations. However, these programs have not been validated using well-planned and rigorous experimental and field protocols. This seismic Rock Mechanics Research Project is aimed at developing a better understanding of the key parameters affecting the repository under seismic loadings and consequently validation of computer programs for use in seismic assessment of underground structures in tuff media.

During this reporting quarter, activities such as pre-test analysis for rock-joint dynamic shear test, instrumented field studies, calibration of field instruments to be used at Lucky Friday Mine, rock-joint specimen preparation, capability development on rock-joint profile measurement, Nevada Test Site (NTS) data collection on ground shock excitation, and preparation and testing of cylindrical specimens for tuff material characterization were carried out.

Pre-test analysis was performed to provide guidance to assist in evaluating the effects of shear test apparatus on dynamic response of the tuff joint specimen. A series of numerical calculations were performed with the three-dimensional distinct-element code, 3DEC, to simulate the shear test apparatus and the dynamic shear test of a naturally jointed tuff specimen. The results of the calculations for the typical range of frequencies of earthquake loadings (i.e., less than 50 Hz) showed that the response of the shear test apparatus, given the assumed properties, did not influence joint response significantly.

Preparation of direct shear test specimens and cylindrical specimens for material characterization is currently underway. Ten direct shear test specimens were prepared in this reporting period. Tests were conducted on 45 uniaxial compression specimens, 5 triaxial compression specimens, and 27 Brazilian disk tension specimens. The average uniaxial compressive strength was found to be 23,255 psi and 28,674 psi for the average triaxial compressive strength with a confining pressure of 500 psi. Typical values for Young's modulus and Poison's ratio of the Apache Leap tuff are 5.4 x 10^6 psi and 0.2, respectively.

Development and assemblage were completed of a rock profiler for profile measurement of rock-joint surfaces. A custom computer program written in Borland's TurboC was developed to perform profile measurement, and to format and store the measured data to a PC/AT data file. The measured profile data will be processed to calculate the corresponding joint roughness coefficient to be used for analyzing the Barton-Bandis rock-joint model.

Collection of available data is ongoing on ground motion under impulsive loading generated in the course of underground nuclear explosions at the Nevada Test Site and during other field tests related to weapons performance. A database has been constructed that contains test information and results regarding five sites.

The instrumentation network was completed to monitor the short- and long-term response of excavations to repeated seismic events, and the changes in water pressure in faults or other structural features in the rock mass as a result of seismic loading. Instrument calibrations were also completed on ten 5-anchor extensometers and two triaxial velocity gauges (transducers).

1.5 INTEGRATED WASTE PACKAGE EXPERIMENTS

The objectives of the Integrated Waste Package Experiments (IWPE) Research Project are to critically evaluate the current material degradation data and to determine parameters affecting long-term container performance. Following extensive peer review and a thorough assessment of recently available information, a new Project Plan for this project (IWPE, Revision 2) was completed and sent to NRC staff for review on May 23, 1990. Since the new Plan is not yet approved, reporting for this period is done in accordance with Revision 1 of the IWPE Project Plan. The Project Plan is organized according to three tasks: Task 1 deals with the critical review of the information available on corrosion of materials for waste-package containers; Task 2 refers to the Waste Package Experimental Program, which includes corrosion and material stability tests; and Task 3 comprises general support and reporting. The report for this quarter is focused on specific accomplishments within Task 2.

During this reporting period, the experimental work was concentrated in the study of the effect of environmental variables on the localized corrosion of alloy 825. A two-level, full factorial design was used to examine the main effects and interactions of chloride, sulfate, nitrate, fluoride, and temperature. These four anions together with bicarbonate, which was maintained at a constant concentration in all the tests, are the predominant anionic species in J-13 well water, the reference water for the experimental work in the Yucca Mountain Project (YMP).

Cyclic, potentiodynamic polarization tests were used to determine the susceptibility of the alloy to localized corrosion. It was found that the electrochemical parameters measured in these tests (pitting potential, repassivation potential, and the difference between them) were not accurate indicators of the extent of localized corrosion observed visually. Therefore, the visual observation of the specimens with a low magnification microscope, which was expressed in terms of a rating number, was combined with the electrochemical parameters in an index, termed localized corrosion index (LCI), to quantify the extent of localized corrosion and the effect of the environmental factors. Chloride and sulfate were found to be promoters of localized corrosion, whereas nitrate and fluoride acted as inhibitors. No effect of temperature was found in the 60 to 95°C range. Only at very high chloride concentrations (10,000 ppm) was a pronounced effect of temperature on the pitting and repassivation potentials observed.

1.6 STOCHASTIC ANALYSIS OF FLOW AND TRANSPORT

A quantitative characterization of large-scale flow and radionuclide transport through the heterogeneous unsaturated fractured rock of Yucca Mountain will be necessary to evaluate compliance with the siting criteria and performance objectives associated with the proposed Yucca Mountain HLW repository (10 CFR 60.112 and 60.113). Realistic modeling of the complex, heterogeneous flow and transport processes at Yucca Mountain will require incorporating the effects of relatively small-scale space-time variability in modeling large-scale unsaturated flow and radionuclide transport.

The specific objectives of the project are to: perform a review of the literature and assess available models and data relevant to the subject site, select a global approach to model large-scale flow and transport in unsaturated fractured rock, develop submodels for incorporation into the global model, and perform large-scale simulations and participate in the validation of flow/transport models for the Yucca Mountain repository. The project is divided in three tasks. The currently active task is Task 1: "Review, Analysis, and Development of Modeling Approach," including Subtask 1, "Literature Review of Modeling Approaches"; Subtask 2, "Data Review and Assessment"; and Subtask 3, "Selection and Initial Development of Global Modeling Approach." Preliminary aspects of the work accomplished during this quarter, particularly concerning Subtask 1, are described in Section 6; the complete results of literature review, initial data assessment, model selection, and first stages of model development will be integrated into the next quarterly report and in the forthcoming technical report for Task 1.

1.7 GEOCHEMICAL NATURAL ANALOGS

The Geochemical Analog Project is designed to provide knowledge of the state of the art in natural analog studies applied to contaminant transport. Activities in Task 1 of the

project, "Literature Review," were underway during the third quarter of 1990. Objectives of Task 1 include: compilation and evaluation of research conducted on natural analogs relevant to contaminant transport at the candidate HLW repository at Yucca Mountain; review of literature on potential sites for a natural analog study to be undertaken; and evaluation of these sites with respect to the degree of relevance to understanding contaminant transport at Yucca Mountain, the possibility of constraining initial and boundary conditions, the feasibility of research at the sites, and the potential usefulness for unsaturated zone contaminant transport model validation.

During this quarter, work continued on literature identification and review. A draft of the *Geochemical Natural Analog Literature Review Report* was written. A summary of that draft report comprises this Quarterly Report. Literature pertinent to the HLW has been reviewed for applications of natural analog studies. From these studies, the usefulness and the limitations of natural analogs have been ascertained and are considered in light of the regulatory interest in natural analog investigations in support of the siting of an HLW repository. Processes and events likely to control contaminant transport at Yucca Mountain are identified herein, and those processes which are amenable to natural analog study are discussed. A set of criteria for the successful use of natural analog studies is presented; and based on this information, candidate sites for a natural analog study relevant to Yucca Mountain are proposed. These sites are the Pena Blanca, Mexico, uranium deposits and the Santorini, Greece, archaeologic sites. Descriptions of these sites and discussions of their potential usefulness are included.

2. UNSATURATED MASS TRANSPORT (GEOCHEMISTRY)
by Roberto T. Pabalan and William M. Murphy

Investigators: Roberto T. Pabalan (CNWRA), William M. Murphy (CNWRA), and Paul Bertetti (CNWRA)

2.1 EXPERIMENTAL STUDIES

2.1.1 Technical Objectives

A major technical consideration in evaluating the suitability of Yucca Mountain, Nevada, as a potential site for high-level nuclear wastes is the presence of thick lateral zones of zeolitic tuffs. Because of their sorptive properties, zeolites could potentially sequester radionuclides initially present in the groundwater, and provide geologic barriers to migration of radionuclides from the repository to the accessible environment. To support the NRC's HLW program, the Center is conducting experimental studies on the thermo-dynamic and ion exchange properties of zeolites under Task 3 of the Geochemistry Research Project. These studies are designed to generate data needed to evaluate the effectiveness of zeolitic tuffs as barriers to radionuclide migration.

The work conducted during this quarter was designed to generate data on the dependence of ion exchange equilibria on the compositions of the aqueous and zeolite phases and on the concentrations of aqueous species. Isotherm experiments were conducted at 25°C involving the exchange of Na^+ with other cations K^+, Cs^+, Ca^{2+}, and Sr^{2+}. The isotherms were determined at two solution normalities to evaluate the effect of solution concentrations on isotherm shapes and exchange selectivities. The data derived in this study will be used in the future to evaluate thermodynamic models for describing and predicting ion exchange behavior.

2.1.2 Ion Exchange Isotherm Experiments

2.1.2.1 Materials and Pretreatment

The clinoptilolite used in the experiments was from zeolitized tuff specimens from Death Valley, California, and was characterized previously using X-ray diffraction, petrographic analysis, and scanning electron microscopy with energy dispersive spectrometry (CNWRA, 1990a). The Na-enriched form of the clinoptilolite powder (100-200 mesh size) was prepared by prolonged treatment with 3m NaCl at 70°C, subsequent to purification by heavy-liquid separation (CNWRA, 1990b). The Na-enriched clinoptilolite was washed repeatedly with deionized water at 70°C in a shaker water bath to remove excess or imbibed NaCl until no Cl⁻ was detected in the washings with 0.1 M $AgNO_3$ solution. The Na-enriched powder was then dried in an oven at 80°C, and equilibrated with water vapor over saturated NaCl solution in a desiccator until constant weight was attained. This last step is required to provide a constant moisture content prior to chemical analysis and exchange experiments (Dyer et al., 1981).

2.1.2.2 Ion Exchange Experiments

Isotherm experiments for the binary exchange reactions $Na^+ = K^+$, $Na^+ = Cs^+$, $2Na^+ = Ca^{2+}$, and $2Na^+ = Sr^{2+}$ were conducted at 25°C and at total solution concentrations of 0.05 and 0.50 N (equivs/liter). The points on the isotherms were obtained by equilibrating accurately weighed amounts of the near homoionic Na-form of the clinoptilolite with a series of solutions containing the two competing cations in different concentration ratios, but at a constant normality of either 0.05 or 0.50 N. The 0.50 N aqueous mixtures were prepared by weight from reagent-grade chloride salts of the respective cations. The 0.05 N solutions were prepared by a ten-factor dilution of the 0.50 N mixtures. Weights of the clinoptilolite powder used in the experiments ranged from 0.05 to 1.0 gram, and solution volumes ranged from 5 to 100 ml. The ratios of zeolite weight/solution volume used in the experiments were optimized to yield significant differences in the initial and final concentrations of the cations in solution. The clinoptilolite+solution mixtures were contained in 15 ml to 125 ml screw-cap plastic bottles. These were kept agitated in a shaker water bath thermostatted at 25.0±0.1°C for at least 3 days. Previous kinetic experiments indicate that equilibrium is closely approached in about 2 days (CNWRA, 1990b).

After the specified period, aliquots of the aqueous solutions were taken and analyzed for the cations K^+, Cs^+, Ca^{2+}, and Sr^{2+}. The cations K^+ and Ca^{2+} were analyzed using Orion ion selective electrodes (ISE) and an Orion EA 920 pH/mV/ISE/°C meter. Sr^{2+} and Cs^+ were analyzed by inductively coupled plasma emission spectrometry (ICP) and atomic absorption spectrometry (AA), respectively. For some solutions, Na^+ was also analyzed by ISE or ICP to check the stoichiometry of the exchange reactions by charge balance constraints.

The exchange levels were calculated from the initial and final concentrations of the cation of interest, and from the weight of clinoptilolite and the volume of solutions used in the exchange experiments.

2.1.2.3 Results

Ion exchange isotherms for the $Na^+ = K^+$ equilibria are shown in Figure 2-1, while isotherms for the $2Na^+ = Ca^{2+}$ equilibria are shown in Figure 2-2. The analytical results for Cs^+ and Sr^{2+}, which were analyzed using AA and ICP, respectively, were not precise enough to use in generating the isotherms. The samples from those mixtures were submitted for reanalysis. The isotherms were calculated using a cation exchange capacity (CEC) value of 2.2 milliequivalents/gram zeolite. This value is considered preliminary pending the results of the zeolite chemical analysis, but is consistent with the CEC derived by Townsend and Loizidou (1984) on clinoptilolite specimens from Hector, California.

Figures 2-1 and 2-2 plot the equivalent mole fraction of K^+ (or Ca^{2+}) in the aqueous solution phase versus the equivalent mole fraction of K^+ (or Ca^{2+}) in the zeolite phase. The results for solution concentrations equal to 0.05 N are given in Figures 2-1a and 2-2a, while those for 0.50 N are shown in Figures 2-1b and 2-2b. As illustrated in these figures, the concentration dependence of the isotherm is small for exchanges
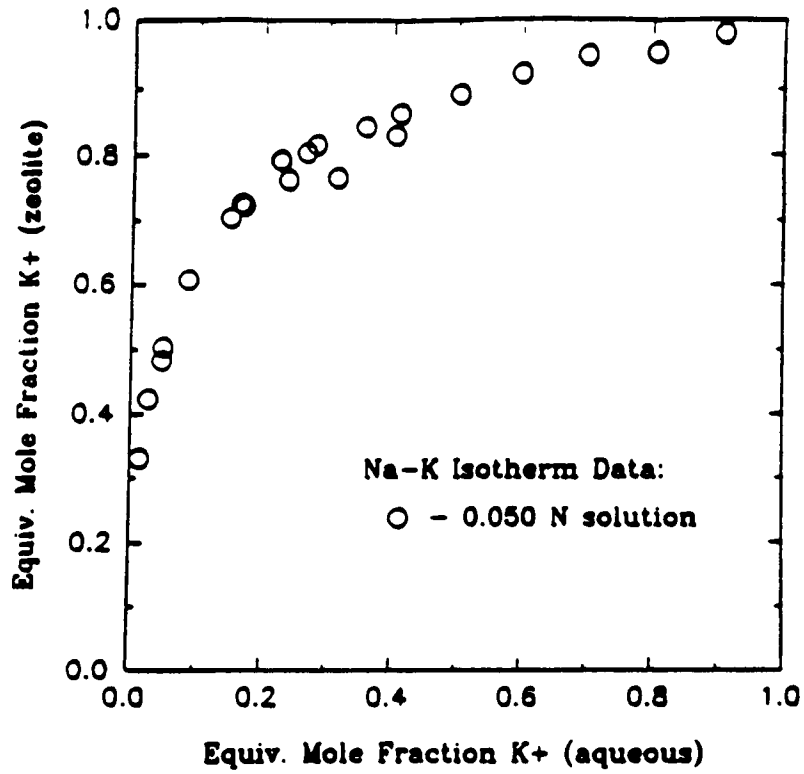
2-1a
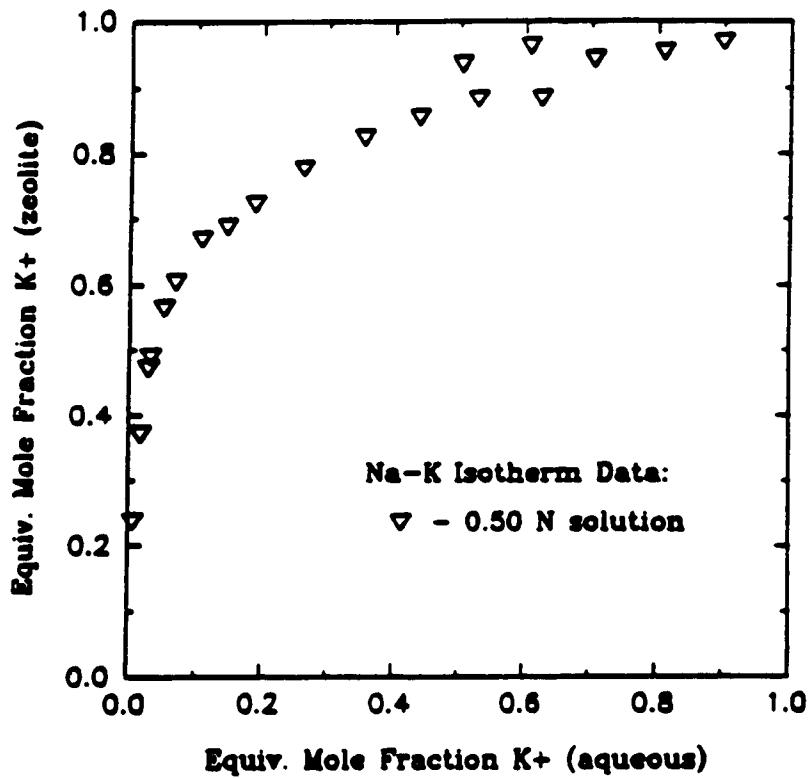
2-1b

Figure 2-1. Isotherm data for the exchange reaction Na^+ K^+ at total solution concentrations of 0.05 and 0.50 N.
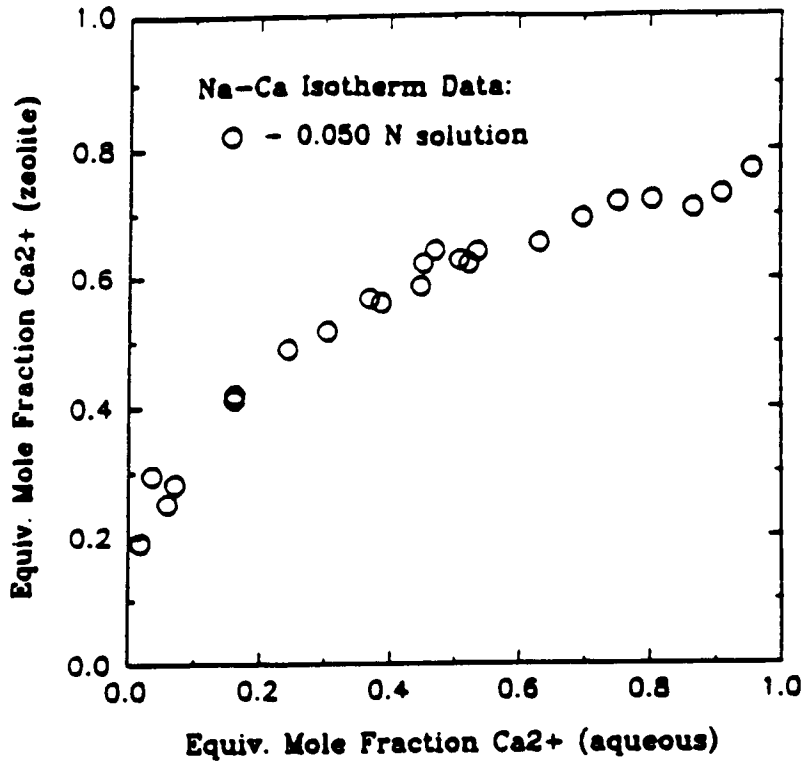
2-2a
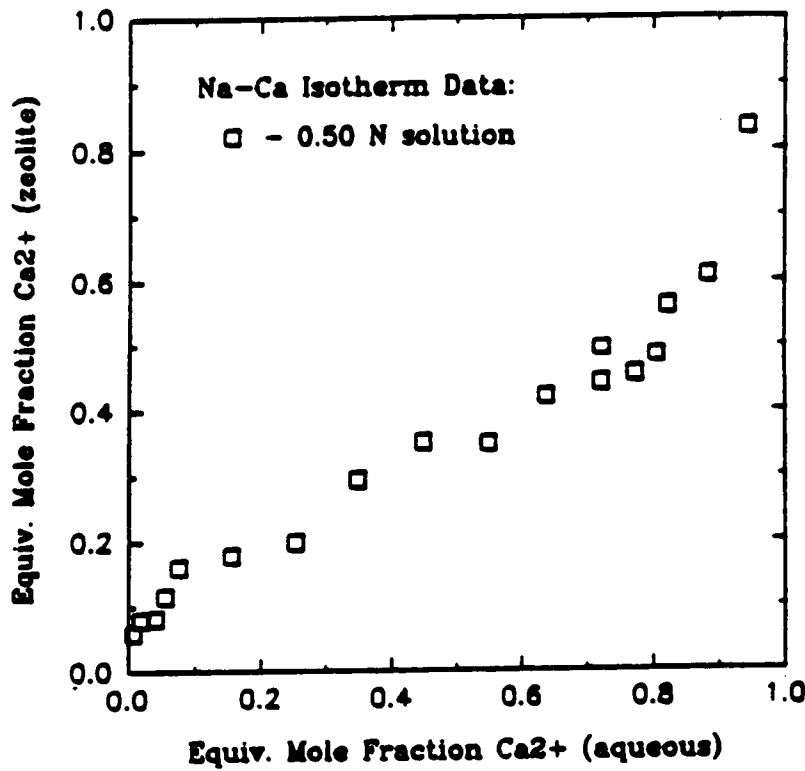
2-2b

Figure 2-2. Isotherm data for the exchange reaction $2Na^+$ Ca^{2+} at total solution concentrations of 0.05 and 0.50 N.

involving ions of the same charge (e.g., Na^+ and K^+), while it is significant for exchanges involving ions of different valences (e.g., Na^+ and Ca^{2+}).

Understanding the composition and concentration dependence of ion exchange processes is important for geochemically complex systems such as Yucca Mountain. The use of thermodynamic models facilitates the evaluation of experimental data and the prediction of ion exchange behavior under various conditions. In particular, it may be possible to predict *a priori* the shape of an isotherm and exchange selectivities at some aqueous solution concentration based on an isotherm measured at a single concentration (Barrer and Klinowski, 1974). The mathematical basis of a thermodynamic model for predicting isotherm shapes will be discussed, and a quantitative evaluation of the model using data determined in this study will be conducted next quarter.

2.2 GEOCHEMICAL MODELING

2.2.1 Technical Objective

An objective of the geochemical modeling task of the Geochemistry Research Project is to develop tools to guide experimentation and to interpret experimental results in geochemistry and related fields. This report presents the results of a thermodynamic analysis of the aqueous solution chemistry employed in experiments conducted as part of the CNWRA Integrated Waste-Package Experiments Research Project (Chapter 5, this volume). An unresolved issue in this research is the control on the evolution of solution pH in corrosion experiments conducted at 95°C. The pH measured at room temperature after experimentation was observed to be significantly greater than the initial solution pH. In addition to pH, a detailed understanding of the equilibrium aqueous speciation of the solutions at the elevated temperatures of the experiments may be useful for the interpretation of the localized corrosion results. The EQ3/6 software package was used to address this problem making use of the open-system, equilibrium (Rayleigh) gas fractionation capabilities developed in the Geochemistry Research Project (Murphy, 1989a).

2.2.2 Thermodynamic Analysis of Aqueous Solution Chemistry in Localized Corrosion Experiments

2.2.2.1 *Initial Solution Chemistry*

Initial solutions were prepared for localized corrosion experiments by dissolving sodium salts to obtain specific total anion concentrations (Chapter 5, this volume). One solution found to be relatively corrosive was selected for this modeling study. Total concentrations of anions and sodium in this solution reported by Sridhar and Cragnolino (Chapter 5, this volume) are given in Table 2-1. The measured pH of this solution at room temperature was reported to be 8.15 ±0.08 (1σ).

The equilibrium aqueous speciation for the test solution was calculated for 25°C with the program EQ3NR (version 3245R110; database 3245R54; Wolery, 1983). Concentrations of sodium salts were used as input mass constraints, and the pH was calculated by adjusting the H^+ (and OH^-) species to obtain charge neutrality. An oxidation state was selected for all calculations for which aqueous species remained oxidized (e.g., the calculated equilibrium nitrite concentration was over 12 orders of magnitude lower than nitrate).

Table 2-1. WATER CHEMISTRY DATA FOR CORROSION POTENTIAL STUDIES

SPECIES	INPUT mg/kg (A)	25°C EQUIL. molal (B)	95°C INITIAL molal (C)	95°C 0.36% VOLAT. molal (D)	95°C 1.8% VOLAT. molal (E)	25°C COOLED 0.36% VOL. molal (F)	25°C COOLED 1.8% VOL. molal (G)
Cl^-	1000	2.82e-2	2.81e-2	2.82e-2	2.86e-2	2.83e-2	2.87e-2
SO_4^{2-}	1000	9.42e-3	9.16e-3	9.19e-3	9.31e-3	9.45e-3	9.58e-3
$NaSO_4^-$		9.93e-4	1.25e-3	1.26e-3	1.29e-3	9.98e-4	1.02e-3
NO_3^-	10	1.61e-4	1.61e-4	1.62e-4	1.64e-4	1.62e-4	1.64e-4
F^-	2	1.05e-4	1.04e-4	1.04e-4	1.06e-4	1.05e-4	1.07e-4
NaF		4.53e-7	1.23e-6	1.24e-6	1.27e-6	4.56e-7	4.68e-7
HCO_3^-	85.5	1.31e-3	1.33e-3	1.08e-3	8.00e-4	8.86e-4	4.49e-4
$NaHCO_3$		5.92e-5	1.66e-5	1.36e-5	1.01e-5	4.02e-5	2.06e-5
$CO_2(aq)$		1.81e-5	4.60e-5	6.32e-6	2.15e-6	6.09e-7	8.46e-8
CO_3^{2-}		1.52e-5	9.00e-6	4.37e-5	6.98e-5	2.08e-4	3.86e-4
$NaCO_3^-$		1.06e-6	8.31e-8	4.04e-7	6.52e-7	1.45e-5	2.72e-5
Na^+	1165.466	4.96e-2	4.93e-2	4.95e-2	5.02e-2	4.98e-2	5.05e-2
pH	8.15±.08	8.137	7.780	8.554	8.888	9.440	10.002
log fCO_2		-3.29	-2.41	-3.28	-3.74	-4.76	-5.62

Notes: (A) Reported (Chapter 5, this volume) total input concentrations for anions. Na^+ concentration calculated based on salt stoichiometry and atomic masses.

(B) Equilibrium aqueous speciation calculated with EQ3 at 25°C. pH calculated based on charge neutrality. Only major species of each component are reported.

(C) Equilibrium aqueous speciation calculated with EQ3 at 95°C. pH calculated based on charge neutrality. Only major species of each component are reported.

(D) Equilibrium aqueous speciation calculated with EQ6 at 95°C after 0.36 percent vaporization of water and equilibrium open system fractionation of CO_2. Only major species of each component are reported.

(E) Equilibrium aqueous speciation calculated with EQ6 at 95°C after 1.8 percent vaporization of water and equilibrium open system fractionation of CO_2. Only major species of each component are reported.

(F) Equilibrium aqueous speciation calculated with EQ3 at 25°C. Total concentrations of components are equivalent to the 95°C solution after 0.36 percent vaporization. pH calculated based on charge neutrality. Only major species of each component are reported.

(G) Equilibrium aqueous speciation calculated with EQ3 at 25°C. Total concentrations of components are equivalent to the 95°C solution after 1.8 percent vaporization. pH calculated based on charge neutrality. Only major species of each component are reported.

Equilibrium was assumed to be obtained among all aqueous species. Dominant calculated aqueous species in the 25°C test solution are reported in Table 2-1. The calculated pH was 8.137, in excellent agreement with the analytical result, which serves to validate the water-chemistry model. Notably, neutral $NaHCO_3$ accounts for over 4 percent of total carbonate, and $NaSO_4^-$ accounts for nearly 10 percent of total sulfate at 25°C. The calculated equilibrium CO_2 fugacity is $10^{-3.29}$ bar, which is slightly greater than the atmospheric CO_2 fugacity of $10^{-3.5}$ bar. This indicates a small potential for CO_2 to exsolve from the solution as a gas at 25°C.

2.2.2.2 Initial Solution Chemistry at Elevated Temperature

The mass constraints noted above were used in EQ3 to calculate the equilibrium aqueous solution composition at 95°C, the temperature of the localized corrosion experiments. The temperature dependence of aqueous equilibria leads to modest changes in the solution (Table 2-1). The calculated pH under the experimental conditions is 7.78. Over 1 percent of the total carbonate exists as $NaHCO_3$, and $NaSO_4^-$ represents 12 percent of the sulfate and 2.5 percent of the sodium at 95°C. The most significant effect is due to the change in carbonate speciation and the decreasing solubility of CO_2 with increasing temperature. $CO_2(aq)$ (which includes all neutral carbonate such as H_2CO_3) accounts for over 3 percent of the total carbonate at 95°C. The equilibrium CO_2 gas fugacity increases to $10^{-2.4}$ bar at 95°C, which is over 10 times greater than the atmospheric CO_2 partial pressure. The water vapor (steam) fugacity increases to 0.82 bar at 95°C from 0.03 bar at 25°C. At 95°C there is a significant potential for release of both H_2O and CO_2 to the atmosphere from this solution.

2.2.2.3 Equilibrium Open-System Volatilization at 95°C

The program EQ6 (e.g., Wolery, 1979; Wolery et al., 1989) can be used to model the evolution of mineral and aqueous solution chemistry for a wide variety of reversible and irreversible reactions. Version 3245R100 of EQ6 has recently been modified to simulate equilibrium, open-system gas fractionation analogous to Rayleigh distillation (Murphy, 1989a,b). In this process, volatile species are released from the aqueous solution at rates that are proportional to their equilibrium fugacities. This code was used to simulate the effects of vaporization of H_2O and CO_2 from the corrosion test water at 95°C.

The amount of volatilization of H_2O and CO_2 in the experimental studies is unknown. Results of two sample calculations are reported here (Table 2-1) representing vaporization of 0.2 mole of H_2O per kilogram (0.36 percent) and 1 mole of H_2O per kilogram (1.8 percent). The pH of the 95°C solution increased markedly from the initial value of 7.78, and the carbonate speciation changed significantly because of CO_2 volatility associated with water vaporization. After 0.36 percent vaporization, the pH increased to 8.55 at 95°C and HCO_3^- decreased from 1.33×10^{-3} molal to 1.08×10^{-3} molal. After 1.8 percent vaporization, the pH increased to 8.89 and HCO_3^- decreased to 7.86×10^{-4} molal. The increase in pH led to an increase of CO_3^{2-} from 9.00×10^{-6} to 6.86×10^{-5} molal after 1.8 percent vaporization. The solution chemistry other than carbonate speciation and pH was not greatly affected.

2.2.2.4 Cooling of Solutions to 25°C

Total concentrations of sodium and anionic components in the partially vaporized 95°C solutions calculated using EQ6 (modified for Rayleigh distillation) were used as input constraints in EQ3 to calculate the pH at 25°C following cooling of the experimental solutions. The pH was calculated by adjusting the H^+ (and OH^-) concentrations to obtain charge conservation in the equilibrium solutions. Results are shown in Table 2-1. For the model solution that sustained 0.36 percent vaporization, the calculated pH was 9.44 at 25°C. This corresponds closely to the measured pH of 9.34 ±0.27 (1σ) at room temperature (Chapter 5, this volume). For the solution that sustained 1.8 percent vaporization, the calculated pH was 10.00 at 25°C.

2.2.3 Conclusions

Thermodynamic calculations using EQ3 and EQ6 modified to perform simulations of open-system, equilibrium gas fractionation have provided an explanation for the observed difference between the initial low temperature pH and pH measurements made in cooled solutions following corrosion experiments conducted at 95°C. An excellent correspondence was observed between the pH measured in the initial solution at room temperature prior to heating and the calculated pH based on input concentrations of salts, charge neutrality, and equilibrium aqueous speciation. This correspondence lends credibility to the accuracy of the pH measurements and the calculations. The observed increases in pH were shown to be compatible with equilibrium, open-system CO_2 volatilization accompanying a small fraction of water vaporization. The calculations identified significant variations in carbonate speciation as a consequence of volatilization. Furthermore, the calculations showed that $NaSO_4^-$ was a significant species at 95°C (12 percent of total sulfate).

2.3 REFERENCES

Barrer R. M., and J. Klinowski. 1974. Ion exchange selectivity and electrolyte concentration. *J. Chem. Soc. Far. Trans. 1.* 70:2080-2091.

CNWRA. 1990. *Report on Research Activities for the Quarter January 1 Through March 31, 1990.* 90-01Q. San Antonio, Texas: CNWRA.

CNWRA. 1990. *Report on Research Activities for the Quarter April 1 Through June 30, 1990.* 90-02Q. San Antonio, Texas: CNWRA.

Dyer, A., H. Enamy, and R. P. Townsend. 1981. The plotting and interpretation of ion-exchange isotherms in zeolite systems. *Separate on Sci. Tech.* 16:173-183.

Murphy, W. M. 1989. Constraints on the chemistry of groundwater in the unsaturated zone at Yucca Mountain, Nevada, and in the proposed repository at that site. *Geochemistry Project Report 1989.* 89-005. San Antonio, Texas: CNWRA.

Murphy, W. M. November 1989. Kinetic calculations of nonisothermal gas-water-rock interactions in hydrologically unsaturated tuff. *Chemistry and Migration Behavior of Actinides and Fission Products in the Geosphere: Abstracts.* Monterey, California: Lawrence Livermore National Laboratory (LLNL).

Townsend, R. P., and M. Loizidou. 1984. Ion exchange properties of natural clinoptilolite, ferrite, and mordenite: 1. Sodium-ammonium equilibria. *Zeolites.* 4:191-195.

Wolery, T. J. 1979. *Calculation of chemical equilibrium between aqueous solution and minerals: The EQ3/6 software package.* LLNL UCRL-52658. Livermore, California: LLNL.

Wolery, T. J. 1983. *EQ3NR A computer program for geochemical aqueous speciation-solubility calculations: User's guide and documentation.* LLNL UCRL-53414. Livermore, California: LLNL.

Wolery, T. J., K. J. Jackson, W. L. Bourcier, C. J. Bruton, B. E. Viani, K. G. Knauss, and J. M. Delany. 1990. Current status of the EQ3/6 software package for geochemical modeling. *Chemical Modeling of Aqueous Systems II.* Melchior, D. C., and R. L. Bassett, eds. American Chemical Society (ACS) Symposium Series 416. Washington, D.C.: ACS:104-116.8.1.

3. THERMOHYDROLOGY
by Ronald T. Green

Investigators: **Ronald T. Green (CNWRA), Frank Dodge (SwRI), Steve Svedeman (SwRI) and Ronald Martin (CNWRA)**

3.1 TECHNICAL OBJECTIVES

The specific objectives of the Thermohydrology Research Project are summarized as follows:

(1) To perform a critical assessment of the state-of-knowledge of thermohydrology in unsaturated fractured media, in the context of present HLW-NRC program activities. This assessment will require an in-depth review of existing literature and on-going programs. The assessment will focus on flow processes, heat transfer mechanisms, and state-of-knowledge experimental methods in porous media.

(2) To perform a detailed dynamic similarity or similitude analysis on the complete set of governing equations relevant to unsaturated flow and to determine the set of dimensionless parameters required to conduct appropriate laboratory simulations. In this analysis of modeling parameters, the range of parameter applicability and limitation on the magnitude of these parameters, as constrained by the principles of dynamic similarity, will be determined.

(3) To identify potential problems associated with the design and performance of laboratory simulations with scaled geometry, fluid, media, and other relevant properties subject to modeling distortion.

(4) To perform a series of separate-effects experiments in order to identify and understand the role of each effect in the overall coupled processes involved in thermohydrologic phenomena.

(5) To design and perform comprehensive experiments whose results will continue to identify key dependent and independent parameters and their relationships to each other in the context of thermohydrologic issues.

(6) To develop the laboratory facilities, experimental methods, measurement techniques, and associated analytic skills to evaluate and validate other program results and to provide a high quality of technical assistance and research in support of NRC's licensing of an HLW repository.

(7) To examine and correlate laboratory results with field data that will aid in the design of future field experiments.

The research project has been delineated into five tasks for accomplishing these objectives.

(1) Task 1 - Assessment of the State-of-Knowledge of Thermohydrology in Unsaturated Media

(2) Task 2 - Design and Execution of Preliminary Separate Effects Experiments

(3) Task 3 - Design of Unsaturated Zone Thermohydrological Experiments

(4) Task 4 - Thermohydrologic Phenomena Induced by the Aggregate of Emplaced HLW in Unsaturated Geologic Media

(5) Task 5 - Unsaturated Zone Thermohydrologic Phenomena Induced by Multiple Packages of HLW

Tasks 1 and 2 are active at this time and are discussed in the following subsections.

3.2 EXPERIMENTAL DEVELOPMENTS

Various thermohydrological phenomena were observed during Test 5, but sufficiently quantified results were not provided. Separate-effects experiment Test 6 has been designed and is currently being assembled. The objective of Test 6 is to perform an experiment similar to Test 5 but with a higher level of control to provide more meaningful resulting data for analysis and comparison with analytical results and numerical simulations.

The experimental apparatus being used in Test 6 was improved in comparison to the apparatus used in Test 5 in several important areas. The cross-sectional width has been increased from 0.75 to about 2.25 inches. This added depth will improve the resolution of the gamma-beam densitometer. Instead of a cumulative water thickness of 0.25 inch at full saturation which existed with the former slender chamber, the new wider chamber will have a cumulative water thickness of about 0.75 at full saturation. The greater range in detection with the densitometer for media between zero and full saturation will permit greater resolution in measuring water content.

Several other technical improvements have been incorporated into the experimental apparatus to improve the resolution of the densitometer. A lead shield has been added to the gamma source to further restrict the cross-sectional area of the gamma-beam. The beam is collimated through an aperture with a 0.25-inch diameter. Therefore, both the gamma-ray source and the detector now have lead shielding for this purpose.

An additional refinement to the densitometer has been the increase of the sampling time of each measurement to about 3 minutes. This adaptation and the application of extra insulation to reduce fluctuations in temperature should increase the signal-to-noise ratio of the recorded gamma-beam measurements.

Additional instrumentation has been installed in the test chamber. Two tensiometers have been added to allow direct measurement of suction pressures. Three thermistors are attached to the exterior of the plexiglass side panels. The thermistors are located equidistantly along the side. Therefore, temperature will be recorded at a total of five locations (the three new thermistors in addition to thermistors located in the two heat exchangers). Thermal fluctuations observed during earlier experiments should also be reduced by the use

of thicker plexiglass side walls (0.75-inch walls versus 0.5-inch walls used in Test 5) and the application of additional insulation.

An additional hole has been installed in both the top and bottom of the test chamber. These holes will permit fully saturating the medium and fully evacuating the medium at the end of the test to permit baseline, gamma-beam densitometer measurements of the test chamber at zero and full saturation.

Several other aspects of Test 6 are similar to Test 5. The matrix is constructed of a mixture of equal portions of 40- and 80-micron diameter glass beads. A vertically oriented fracture is again simulated using 160-micron diameter glass beads. The heat exchangers are oriented in the vertical direction. Dyes will also be used to visually track the movement of the liquid water. Photographs will be taken periodically to record the liquid movement. The temperatures of the two heat exchangers will be maintained at 20° and 60°C using circulated fluid from constant temperature water baths as in Test 5.

The duration of Test 6 is anticipated to be 45 to 60 days; however, the experiment may be conducted longer if the chamber has maintained integrity and meaningful data are still being collected.

3.3 NUMERICAL SIMULATIONS

Preliminary results of the numerical simulations using a modified version of the TOUGH code have been evaluated. The intention of performing the simulation is to evaluate the theory incorporated into the TOUGH code and to determine if the numerical simulation adequately represents the phenomena observed in the laboratory experiment. Particular phenomena of interest include direction of liquid water flow, liquid and water vapor saturation, and matrix/fracture interactions.

In particular, it is the intention of these numerical exercises to evaluate the capabilities of TOUGH to simulate the two significant flow patterns observed in Test 5, the apparent formation of a convection cell, and the reluctance to flow across the simulated fracture under less-than-saturated conditions. Although the difficulty of simulating these complex processes has been documented (Runchal et al., 1985; Nitao and Buscheck, 1989; and Pruess et al., 1990, for examples), it is thought that such an assessment will provide valuable insight into the thermohydrological phenomena expected in the geologic medium near HLW.

The simulated medium is a vertically oriented, two-dimensional (8.15 by 5.75 inches) grid with variably sized elements that decrease in width proximal to the vertically oriented, simulated fracture. The two vertical edges of the container are simulated as constant-temperature (20 and 60°C), no-flow boundaries; and the two horizontal edges are treated as adiabatic, no-flow boundaries. The simulated fracture is vertically oriented and located approximately halfway between the two vertical boundaries. A schematic of the finite-difference grid is illustrated in Figure 3-1. A list of the input parameters of interest that were included in this simulation are included as Table 3-1.
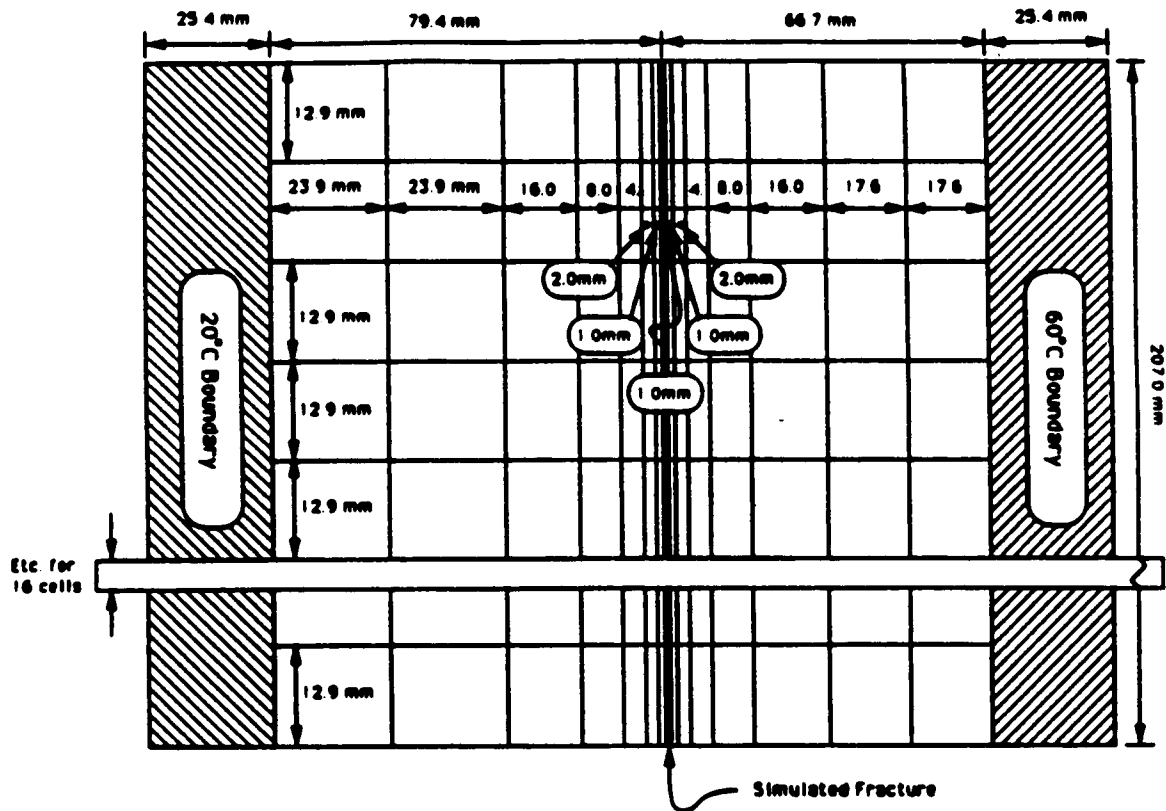
Figure 3-1. Schematic of finite-difference grid used in the numerical simulation of Test 5

Although densitometer measurements from Test 5 correlated positively with moisture movement observed in the test chamber, moisture content in the test chamber measured with the densitometer had insufficient resolution to be used quantitatively. More useful information gathered during the experiment was photographs of the locations of the dyes injected into the medium to visually track the movement of water.

The experiment was simulated for a period of about 35 days using the TOUGH code. This length of time was similar to the duration of laboratory experiment Test 5. Included in this report are liquid and gas saturation levels computed for the last time step of the simulation (Figures 3-2 and 3-3). As illustrated in the figures, the simulated movement of liquid water and water vapor responded to the effect of gravity and to effects of the constant temperature in a manner similar to what was observed in laboratory Test 5. The liquid-water saturation levels vary from about 52 percent at the top near the heated (right) boundary to a maximum liquid saturation of about 78 percent at the base of the cooler (left) boundary.

Table 3-1. INPUT PARAMETERS FOR TOUGH

Grid:	• 2-dimensional with 16 x 17 elements
Physical:	• 8.15 x 5.75 inches
Porosity:	• 35 percent
Permeability:	• matrix 1.2×10^{-14} m^2 • boundary 4.0×10^{-40} m^2 • fracture 1.2×10^{-12} m^2
Specific heat:	• matrix 800 J/kg-C • boundary 1.0e+10 J/kg-C
Temperature:	• right boundary 60°C • left boundary 20°C • matrix initial temperature 20°C

Van Genuchten:	• Matrix:
	    - α = 0.759 1/KPa
	    - n = 7.38
	    - θ = 0.341
	
	 • Fracture:
	    - α = 0.920 1/KPa
	    - n = 7.38
	    - θ = 0.341

A notable exception to this was the moisture movement in the elements modeled as the fracture. Closer inspection of the fracture elements revealed that the simulated fracture had liquid saturation levels greater than adjoining matrix elements in contrast to what would be expected with respect to capillary forces and the relatively larger pore size of the fracture. The possible source for this discrepancy may in the selection of the van Genuchten parameters of the fracture relative to those selected for the matrix. Although the van Genuchten parameters for the matrix were based upon experimental measurements, the van Genuchten parameters for the fracture were estimated.

Additionally, the moisture content of the two sections of the medium separated by the simulated fracture in Test 5 appeared to be substantially different at the end of the experiment. This qualitative observation was based on the hue of the medium as seen through the plexiglass side walls. The observation is interpreted as an indication that the section on the cool side of the fracture had a substantially higher moisture content than on the heated side. The simulation did not reflect this observation; i.e., it did not display an abrupt change in moisture content on the cool side of the fracture compared to the warm
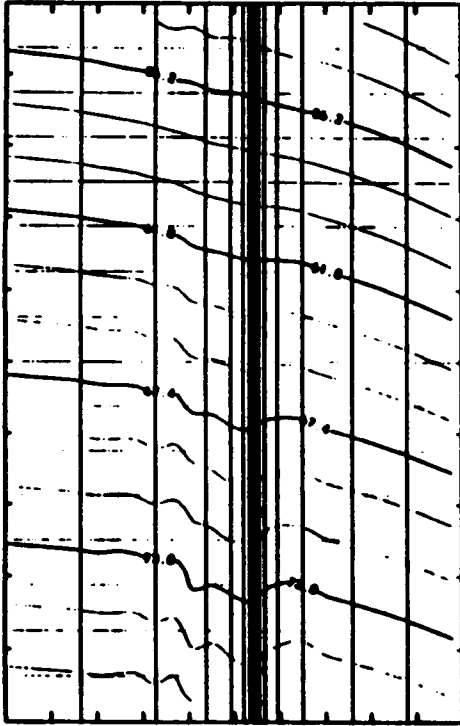
Figure 3-2. Liquid-water distribution simulated at 35 days using the TOUGH code
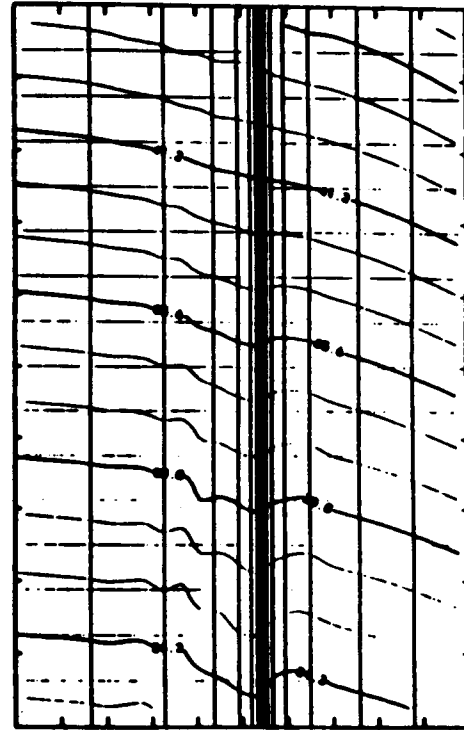
Figure 3-3. Water-vapor distribution simulated at 35 days using the TOUGH code

side. This inconsistency may again be attributed to inappropriate van Genuchten parameters assigned to the fracture. Further refinements in the model are being attempted in an effort to more accurately simulate the above mentioned nonisothermal physical processes, in general, and those processes affected by the fracture, in particular.

3.4 ANALYTICAL DEVELOPMENTS

The dynamic similitude analysis, including the parameters and dimensionless terms, has been refined to reflect the data gathered during Test 5. Data gathered using the numerical simulations with the TOUGH code will be used to assess the various dimensionless quantities to identify those that appear to be the most sensitive.

A list of the values of the nominal or baseline properties of the test-case parameters is being compiled from which the comparisons will be made. The refined list of baseline parameters includes temperature, pore diameter, liquid surface tension, liquid and vapor density, porosity, saturated liquid permeability of matrix, specific heat of medium, fracture width, fracture roughness, saturated liquid permeability of fracture, fracture saturation, and heat and water flux, where applicable. Additional parameters that will be part of the similitude analysis include gravity, length scales, and time.

Based upon a review of the technical literature and on the observations during the earlier separate-effects experiments, inclusion of several physical processes in the similitude

analysis has been neglected at this time. These processes or attributes include liquid buoyancy, liquid infiltration, and viscosity. If these omissions do not prove to be prudent, the terms can be included in future analyses. Processes of interest that will be analyzed include vapor buoyancy, properties and number of fractures, capillarity, latent heat, and specific heat of the matrix.

The list of dimensionless pi terms has also been refined and now totals fourteen, two of which are dependent and the remaining twelve are independent. The two independent terms are nondimensional temperature and nondimensional saturation and are expressed as follows:

$$\left(\frac{K_o}{q_o L^2}\right)(\delta T), \quad \delta S$$

The twelve pi terms are expressed as

$$\Pi_1 = \frac{L K_o t}{C_o \rho_o}, \quad \Pi_2 = \frac{\rho_{v_o}^2 g \beta_{vo} d_o^3 T_o}{\mu_{v_o}^2}, \quad \Pi_3 = \phi_o, \quad \Pi_4 = \frac{k_o}{k_{fo}},$$

$$\Pi_5 = \frac{q_o L \mu_v}{\rho_{v_o} \sigma_o h_{fg}}, \quad \Pi_6 = \frac{\rho_{l_o} g d_o^2}{\sigma_o}, \quad \Pi_7 = \frac{h_{fg}}{C_o T_o}, \quad \Pi_8 = \frac{q_o L^2}{K_o T_o},$$

$$\Pi_9 = \frac{d_{fo}}{d_o}, \quad \Pi_{10} = \frac{r_{fo}}{d_{fo}}, \quad \Pi_{11} = S_{io}, \quad \Pi_{12} = S_{fo}$$

where:

d	=	pore diameter
σ	=	liquid surface tension
ρ	=	density
ϕ	=	porosity
k	=	saturated hydraulic conductivity
C	=	specific heat of medium
S_i	=	matrix saturation
K	=	matrix thermal conductivity
d_f	=	fracture width
r_f	=	fracture roughness
S	=	saturation
h_{fg}	=	latent heat of vaporization
g	=	gravity
t	=	time
β	=	coefficient of thermal expansion
μ	=	viscosity
g	=	heat source
L	=	characteristic length (e.g., of model size or heater)

and where the subscript l denotes liquid, v denotes vapor, f denotes fracture, and o denotes the nominal or baseline case.

After the parameters have been assigned nominal values, the twelve pi terms will be computed using the TOUGH code and compared to nondimensional saturation and temperature. The values of each of the parameters will be varied while the remaining parameters are held constant. The pi terms for each varied set of perturbed parameters will be computed. If a pi term does not vary significantly as the parameters are perturbed, the implication exists that the particular pi term can be varied without adversely affecting the scale model. This pi term can then be eliminated from further analysis. Pi terms that do vary significantly will need to be simulated dynamically (exactly) in the scale model.

After this analysis, a reduced set of parameters and pi terms will have been identified. For completeness, parameters neglected earlier in the analysis can be assessed in similar fashion if there is any indication to warrant this action. A dynamic similarity law can be formulated using these analyses.

3.5 REFERENCES

Pruess, K. 1987. *TOUGH Users Guide*. NUREG/CR-4645. Berkeley, California: Livermore Berkeley Laboratory (LBL).

Pruess, K., J. S. Y. Wang, and Y. W. Tsang. 1990. On thermohydrologic conditions near high-level nuclear wastes emplaced in partially saturated fractured tuff, 1, simulation studies with explicit consideration of fracture effects. *Water Resources Research*. 26(6), pp 1235-1248.

Nitao, J. J., and T. A. Buscheck. 1989. *On the Movement of a Liquid Front in an Unsaturated, Fractured Porous Medium*. LLNL UCID report. NNA 891130.0051. Livermore, California: LLNL.

Runchal, A. K., B. Sagar, R. G. Baca, and N. W. Kline. 1985. *PORFLO-A Continuum Model for Fluid Flow, Heat Transfer, and Mass Transport in Porous Media: Model Theory, Numerical Methods and Computational Tests*. Rockwell International, DE-AC06-77RL01030. Hanford, Washington: Rockwell.

4. SEISMIC ROCK MECHANICS
by Simon M. Hsiung and Asadul H. Chowdhury

Investigators: **Mikko P. Ahola (CNWRA), Asadul H. Chowdhury (CNWRA), Jaak J. Daemen (Consultant), Roger Hart (ITASCA), Simon H. Hsiung (CNWRA), Daniel D. Kana (SwRI)**

4.1 TECHNICAL OBJECTIVES

The overall objectives of the Seismic Rock Mechanics Research Project have been outlined in the second CNWRA research program quarterly report (CNWRA, 1990). The work conducted during this quarter includes pre-test analysis for the rock-joint dynamic shear test; specimen preparation and laboratory testing of welded tuff materials; Nevada Test Site (NTS) data collection on ground-shock excitation; and instrumented field studies at the Lucky Friday Mine, Mullan, Idaho, for

- Dynamic effects on underground openings and
- Seismic effects on the geohydrologic regime.

4.2 PRE-TEST ANALYSIS FOR THE ROCK-JOINT DYNAMIC SHEAR TEST

The objective of this pre-test analysis for the rock-joint dynamic shear test is to provide preliminary insight to assist in evaluating the effects of shear-test apparatus on dynamic response of the tuff joint specimen. A series of numerical calculations using the three-dimensional distinct-element code, 3DEC, were performed to simulate the shear-test apparatus and the dynamic shear test of a naturally jointed tuff specimen.

This analysis is considered the first step in the evaluation and development of an analytical model representation of a naturally jointed tuff specimen. The Coulomb and continuously yielding joint models are used in 3DEC to demonstrate the evaluation procedure. The Coulomb slip model is the standard used in rock mechanics to describe primarily the static response of a rock joint. The continuously yielding model is a more complex algorithm that simulates continuous-yielding, displacement-weakening, and hysteretic effects, and has greater potential to represent joint behavior associated with dynamic loading. These models are described in detail by Kana, et al. (1989a). The results of this analysis must be considered preliminary because actual test data from naturally jointed tuff specimens are not yet available. Nevertheless, these simulations serve as a starting point for correlation to laboratory test results once the experimental program has begun.

4.2.1 3DEC Models of the Dynamic Shear Test

Two 3DEC models have been used in the preliminary investigations: a simple base model of a jointed tuff specimen and a full model consisting of a jointed tuff specimen inside the shear box. The geometries of the two models are shown in Figures 4-1 and 4-2. The base model of the jointed tuff specimen consists of two blocks and assumes uniform normal and shear stresses along the interface joint plane of these two blocks. The relative shear motion between the two blocks of the specimen is prescribed directly according to a given shear-displacement time history. Normal and shear stresses and
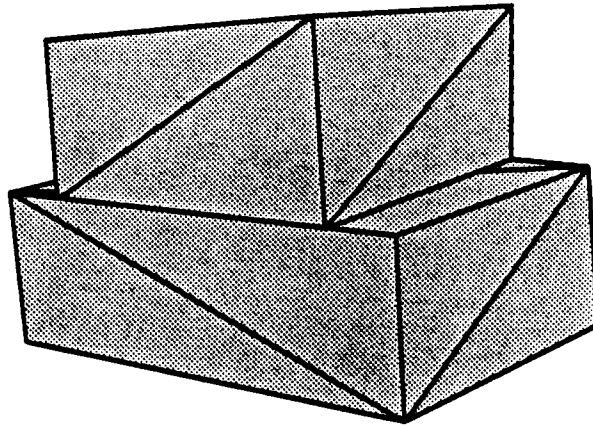
Figure 4-1. 3DEC simple base model of a jointed tuff specimen
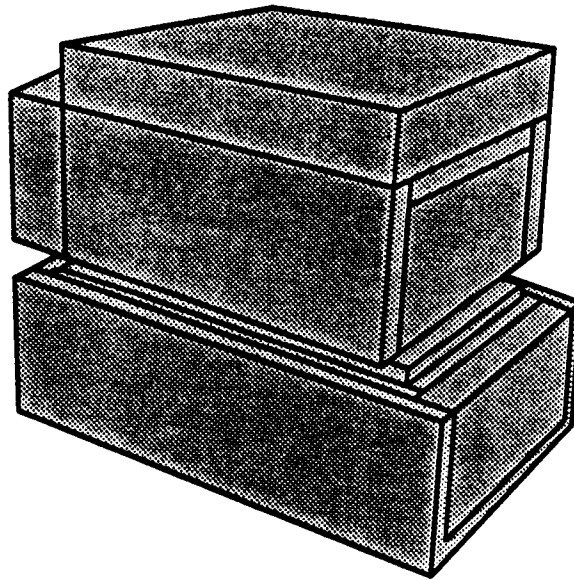
Figure 4-2. 3DEC full model consisting of a jointed tuff specimen inside the shear box

normal displacements along the joint are calculated according to the prescribed Coulomb and continuously yielding joint models. This base 3DEC model is the primary tool for investigating the analytical representations for joint mechanical behavior.

The full model of the jointed specimen inside the shear box is a more elaborate representation of the shear test condition, as described by Kana, et al. (1989b), and can be used to assess the influence of the actual experimental conditions on the dynamic response of the tuff joint specimens.

4.2.2 Simulation of the Demonstration Test on Concrete Joint Specimen

The application of the 3DEC base model is illustrated by simulating the pseudostatic demonstration test on a concrete joint specimen, reported by Kana, et al. (1989b). The continuously yielding model is used for these simulations. Comparisons are illustrated below for both joint normal stress versus joint closure and joint shear displacement versus joint shear stress.

In the continuously yielding model, the joint normal and shear stiffnesses are normal stress dependent and are given by:

$$K_n = a_n \sigma_n^{en}$$

$$K_s = a_s \sigma_n^{es}$$

where K_n is joint normal stiffness, K_s is joint shear stiffness, and a_n, e_n, a_s, and e_s are constants.

The joint normal stress versus joint closure curve obtained from the 3DEC base model using the normal stiffness parameters derived from experimental results on concrete joint specimen (Kana, et al., 1989b) is compared to the experimental curve in Figure 4-3.

The best fit of the results from the continuously yielding model in 3DEC to the laboratory test results for joint shear stress versus joint shear displacement provides the following continuously yielding model parameters (Cundall and Lemos, 1988):

- ϕ (intrinsic friction angle) = 37°

- ϕ_{mo} (initial friction angle) = 85.9°

- R   (joint roughness parameter) = 0.31 mm

The best-fit curve is shown in Figure 4-4.

4.2.3 Preliminary Numerical Simulations of Tuff Joints

Joint and basic material properties for the jointed tuff specimens to be tested are not available. Therefore, "recommended" tuff joint properties given in the Site Characterization Plan Conceptual Design Report (SCP-CDR)(MacDougall et al., 1987) were used to the extent possible to perform simulations for providing preliminary assessments of tuff the continuously yielding model are not directly available from the SCP-CDR, two condi-
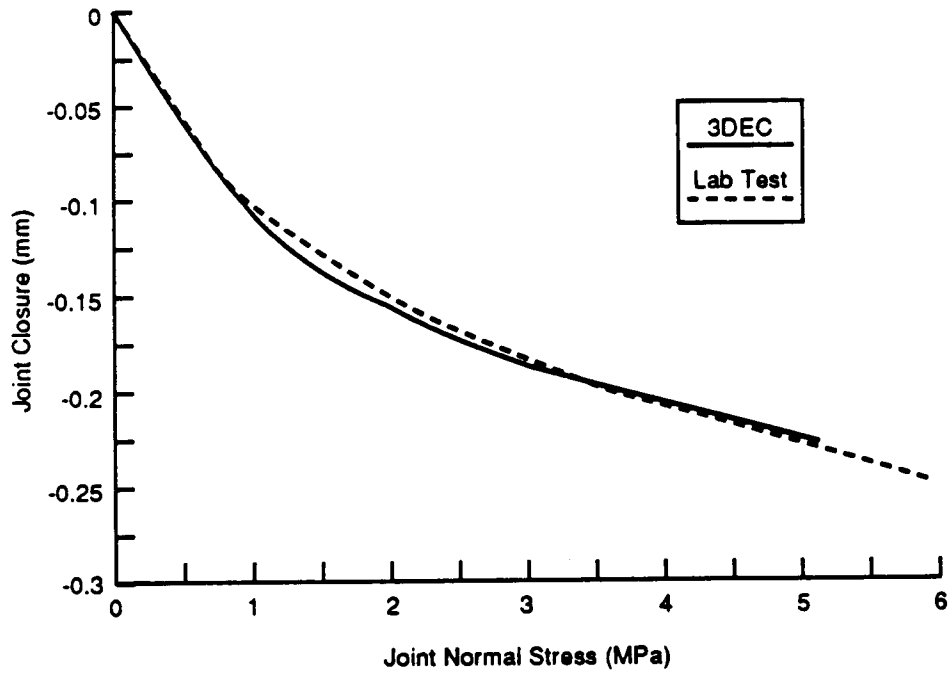
Figure 4-3. Comparison of 3DEC model to laboratory test results for joint closure variation with pseudostatic normal stress
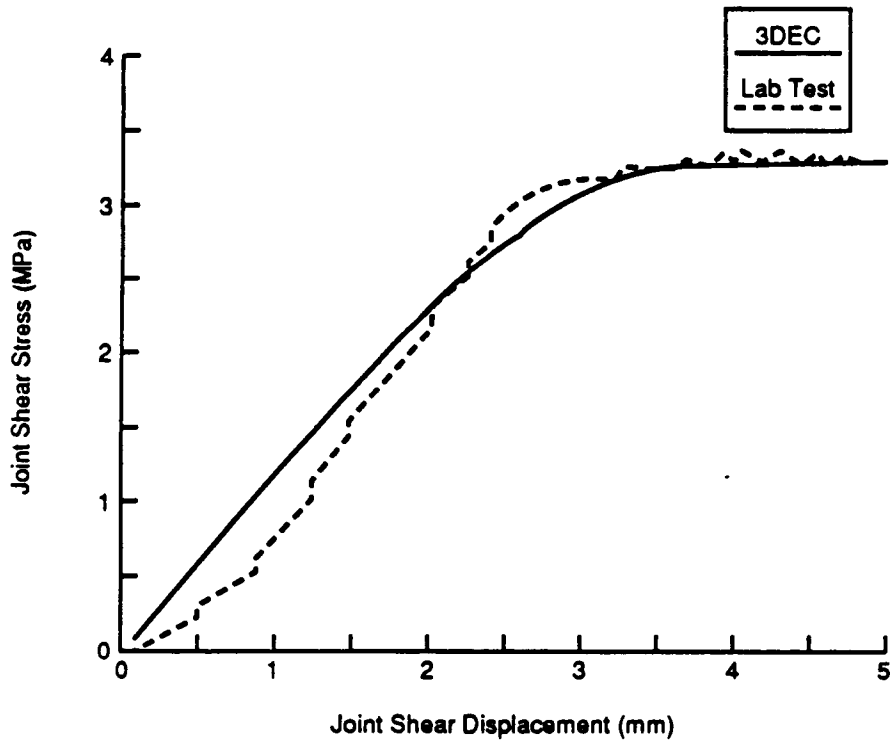
Figure 4-4. Comparison of 3DEC model to laboratory test results for joint stress variation with joint shear displacement at normal stress = 4.36 MPa

tions of properties, one for a smooth joint and one for a rough joint, were investigated. The properties used in the joint models are listed in Table 4-1.

Table 4-1. ASSUMED TUFF JOINT MODEL PARAMETERS

Parameters	Coulomb Model	Continuously Yielding Model Case 1	Continuously Yielding Model Case 2
Normal Stiffness (GPa/m)	100.0	100.0	100.0
Shear Stiffness (GPa/m)	10.0	10.0	10.0
Cohesion	0.0	0.0	0.0
Tensile Strength	0.0	0.0	0.0
Intrinsic Friction Angle	28.4	28.4°	28.4°
Initial Friction Angle	--	42.6°	56.7°
Roughness Parameter (mm)	--	0.1	0.1

The 3DEC base model was used with an assumed constant normal stress of 5 MPa during shear testing. Joint responses to monotonic loading, load reversal, harmonic loading, and earthquake loading conditions were evaluated. The loading conditions were applied as displacement histories to the joint, and inertial effects were neglected. Because neither the Coulomb model nor the continuously yielding model is a velocity-dependent model, the time scale does not influence the shear stress-displacement results.

4.2.3.1 Monotonic Loading

Figure 4-5 presents the resulting shear stress-displacement curves for the Coulomb model and continuously yielding model Cases 1 and 2. Both continuously yielding cases display yielding before the residual shear stress is reached. The properties assumed for Case 1 lead to a curve without a peak while Case 2 displays a peak shear stress of 2.96 MPa, corresponding to a friction angle of $30.6°$. The maximum dilation angle calculated at the peak shear stress for the continuously yielding model Case 2 is $2.2°$. The Coulomb model and continuously yielding model Case 1 display no joint dilation.

4.2.3.2 Load Reversal

Reversal in shear loading is simulated by prescribing a shear-displacement history, as shown in Figure 4-6. The resulting shear stress-displacement curves are shown in Figures 4-7 and 4-8 for the Coulomb model and continuously yielding model Case 1, respectively.

4.2.3.3 Harmonic Loading

A sine-wave shear displacement is applied for the harmonic loading study. For both cases, the continuously yielding model displays a loss in shear strength upon cyclic shearing (Figure 4-9) while the Coulomb model does not display shear strength loss.

4-5
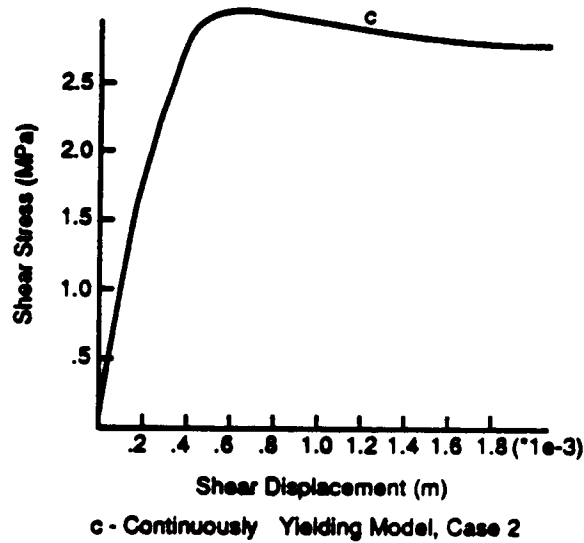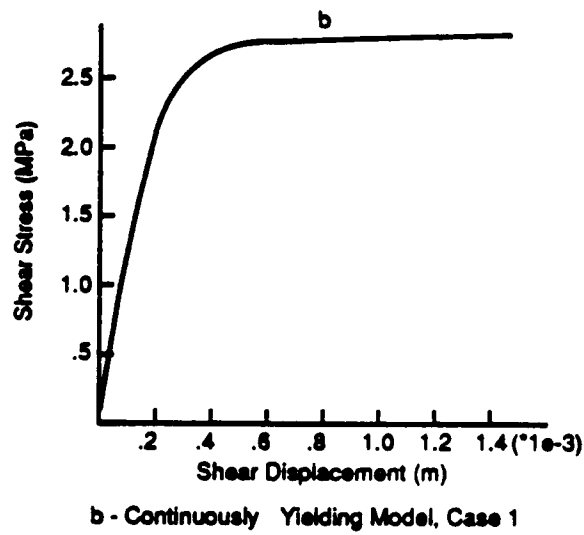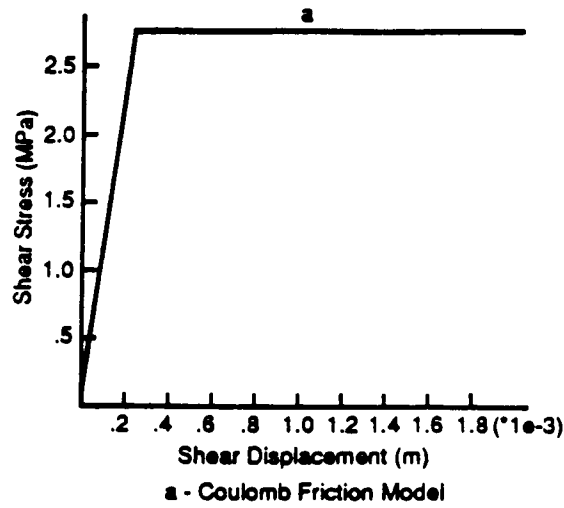
Figure 4-5. Shear stress-displacement curve for monotonic loading with Coulomb friction model and continuously yielding model Cases 1 and 2
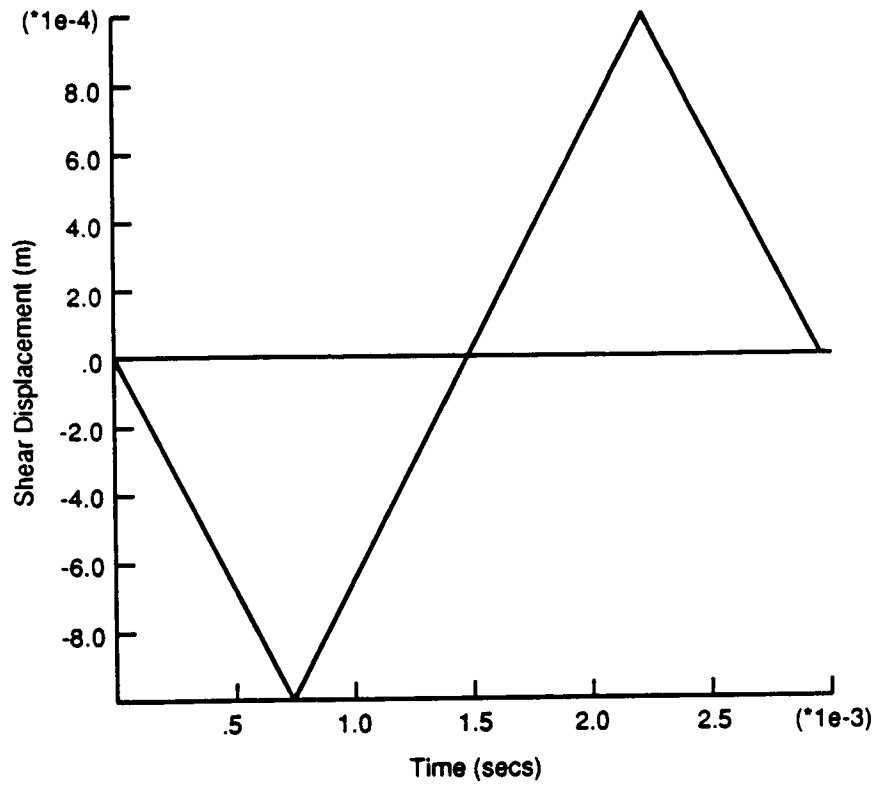
Figure 4-6. Shear displacement path for load reversal
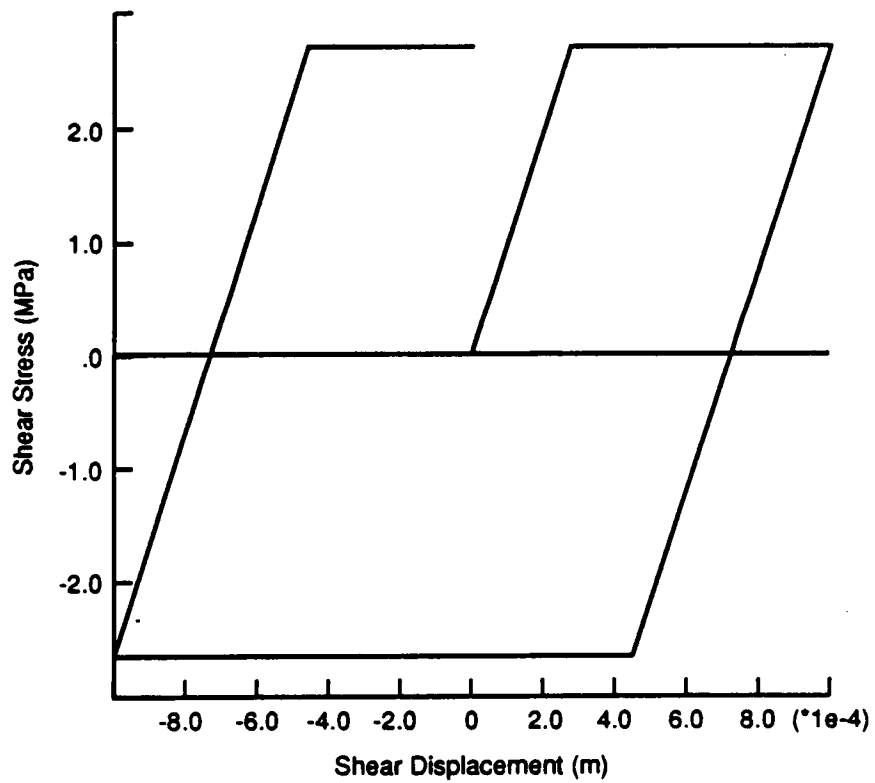
Figure 4-7. Shear stress-displacement curve for load reversal with Coulomb friction model

4-7
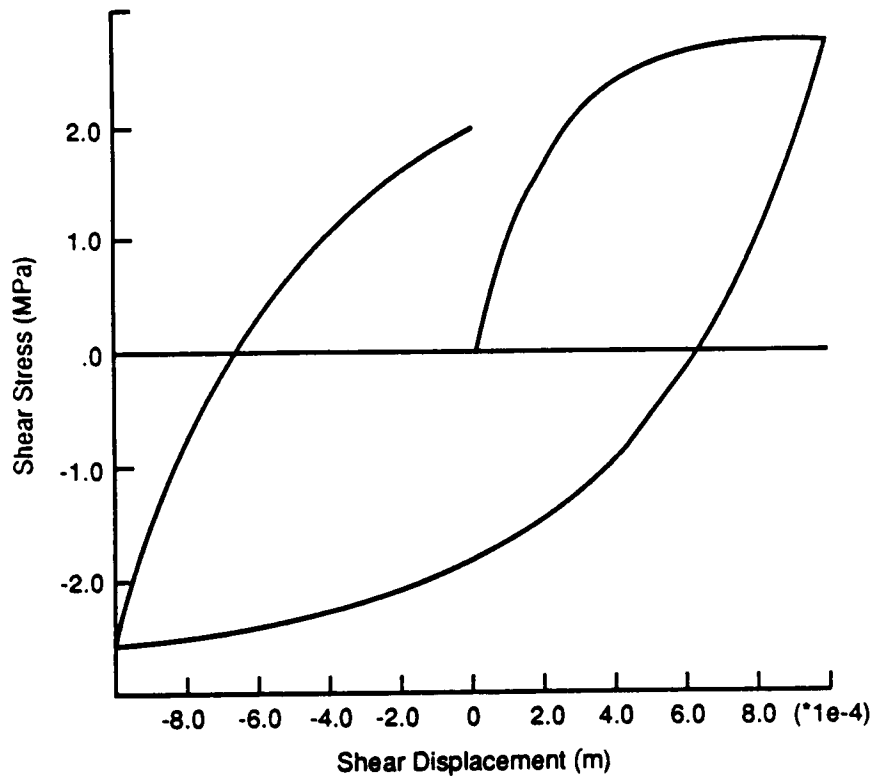
Figure 4-8. Shear stress-displacement curve for load reversal with continuously yielding model, Case 1
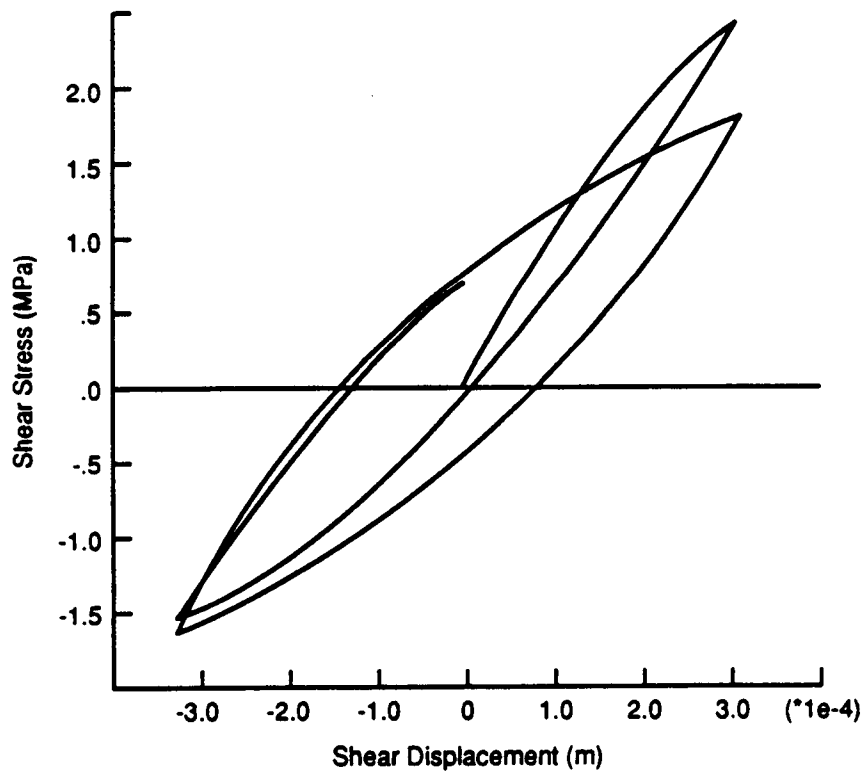
Figure 4-9. Shear stress-displacement curve for harmonic loading with continuously yielding model, Case 2

4-8

4.2.3.4 Earthquake Loading

The shear stress-displacement curve for the Coulomb model based on a typical earthquake velocity drive is shown in Figure 4-10. Slip occurs at 2.7 MPa for this model. The curve for the continuously yielding model Case 2 is given in Figure 4-11.

4.2.4 Influence of Test Conditions

Preliminary calculations were made to study the influence of the shear-box test setup on joint response. The objective was to determine the influence of input frequency on joint motion, taking into account the stiffness of the grout, shear box, and horizontal and vertical loading system. The full shear-box model shown in Figure 4-2 was used for the calculations.

4.2.4.1 3DEC Full Shear Box Model

The 3DEC model consists of blocks representing the tuff specimen with the same dimensions as the 3DEC base model, that is, a 1-inch-thick grout layer, a 2-inch-thick steel box, and horizontal and vertical loading blocks with stiffness approximating that of the load system. Figure 4-12 shows a vertical section through the 3DEC model and identifies the component materials. The bottom of the 3DEC model is fixed in all directions. After a normal stress of 5 MPa is applied to the top loading block, the top block is fixed in the vertical direction during the dynamic shear-load phase. The dynamic load is applied as a horizontal velocity to the left loading block. Displacements and stresses are monitored during the simulations at five locations denoted on Figure 4-12. Point A corresponds to the left loading block; point B to the top loading block; and points C, D, and E to points along the tuff joint plane through the center of the model. The tuff joint is assumed to be elastic for the majority of the simulations. Table 4-2 presents the properties assumed for this analysis.

Table 4-2. ASSUMED PROPERTIES FOR 3DEC FULL SHEAR BOX MODEL

Property	Young's Modulus (GPa)	Poisson's Ratio
Tuff Specimen	30.4	0.22
Grout	10.1	0.22
Steel	210.0	0.30
Left Loading Block	210.0	0.30
Top Loading Block*	210.0	0.30

*For one run, the Young's Modulus was 21 GPa to simulate a soft loading block.
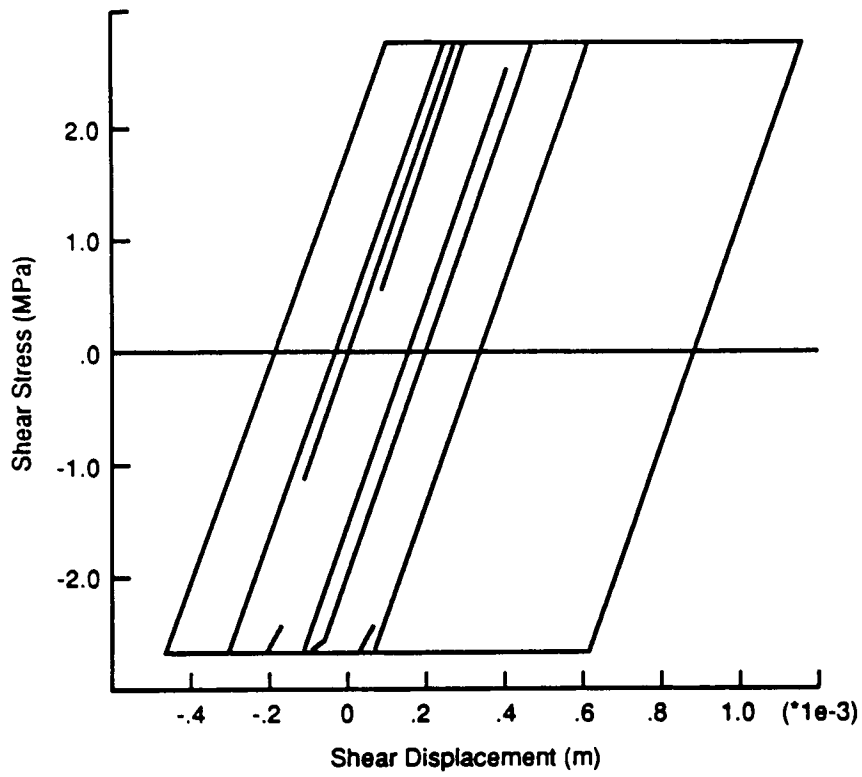
Figure 4-10. Shear stress-displacement curve for earthquake loading with Coulomb friction model
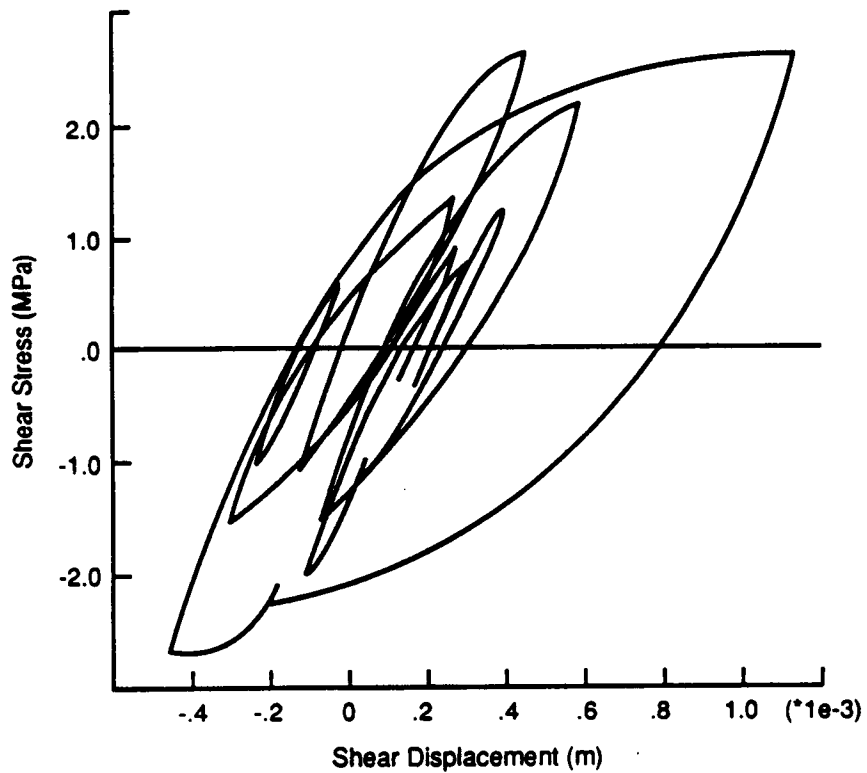
Figure 4-11. Shear stress-displacement curve for earthquake loading with continuously yielding model, Case 2

4-10
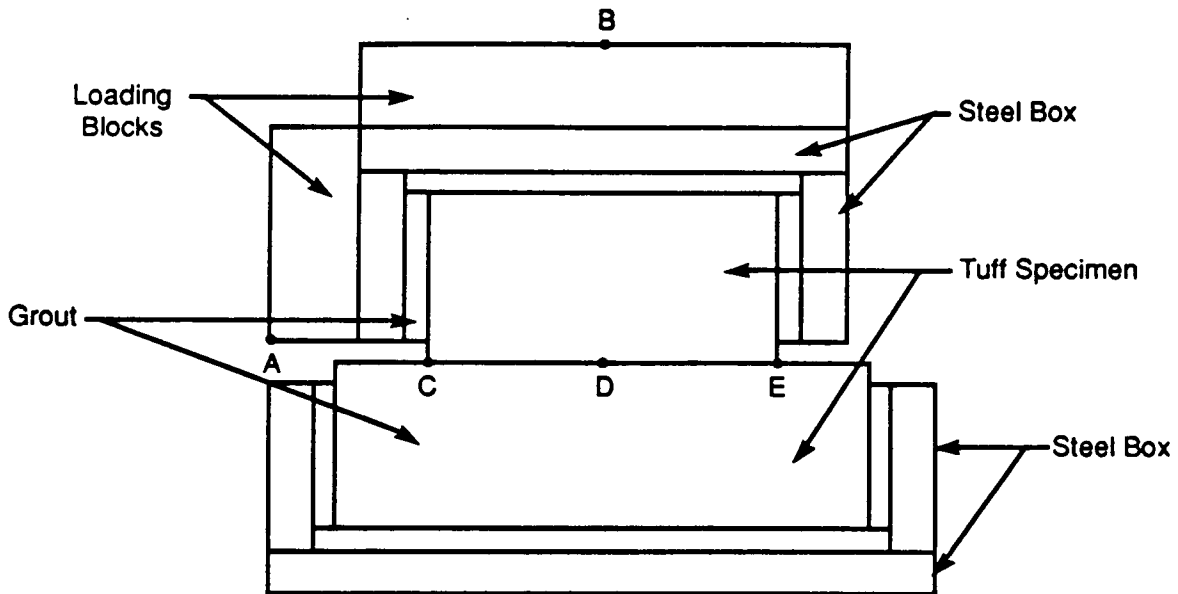
Figure 4-12. Vertical section through 3DEC full shear-box model

4.2.4.2 Dynamic Analysis

A sine-wave drive signal was applied to the left loading block to study dynamic effects. Different frequency conditions were investigated. The peak velocity was varied for each frequency so that the peak displacements at point A for all cases were the same.

The simulation results show an obvious deviation from the prescribed sine-wave input (Figure 4-13) as a consequence of the natural frequency of the model system. The influence of natural frequency decreases as input frequency decreases (compare Figures 4-13 and 4-14) and increases as the stiffness of the left loading block decreases. The normal stress across the joint was not uniform for these simulations. Normal stress at the center of the model was lower than that at the joint edges, and more slip was calculated at the center when the joint was allowed to slip.

4.2.5 Summary and Recommendations

The 3DEC base model can be used to investigate existing joint constitutive relations and identify conditions when joint model improvements are needed. As more information from the laboratory tests becomes available, the joint model can be improved or revised.
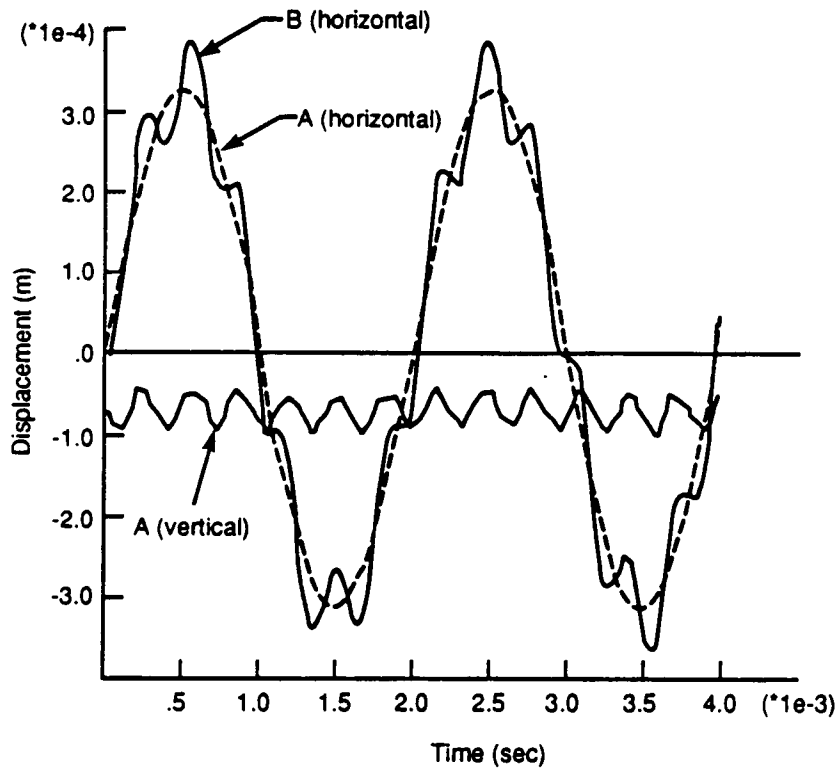
Figure 4-13. Horizontal and vertical displacement histories for 500-Hz input frequency
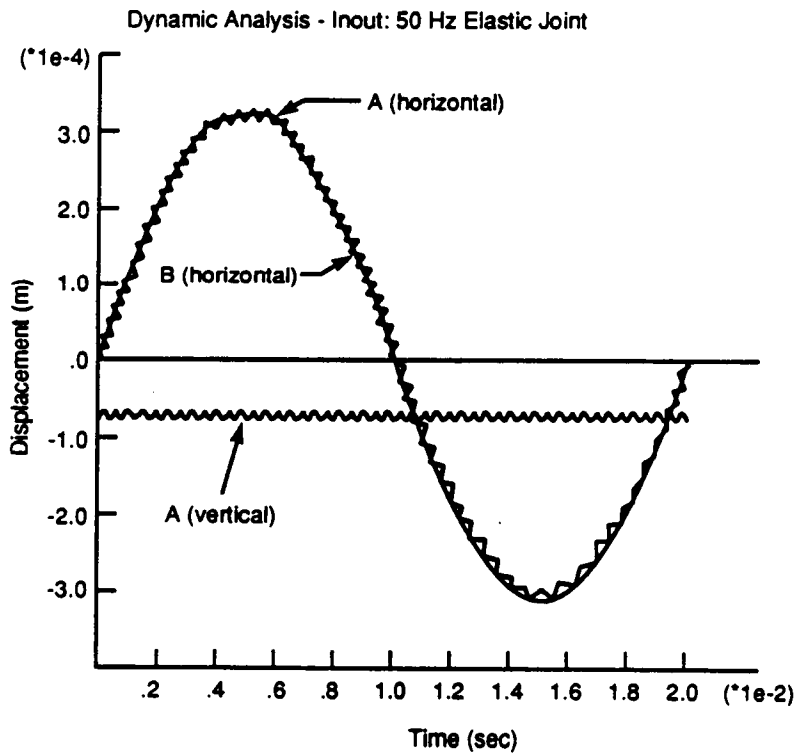
Figure 4-14. Horizontal and vertical displacement histories for 50-Hz input frequency

The 3DEC base model neglects inertial effects of joint behavior. Ascertaining the importance of velocity dependency on tuff joint response by means of laboratory testing is necessary. If inertial effects are important, modification to the Coulomb and continuously yielding model will be required.

For the typical range of frequencies of earthquake loadings (i.e., less than 50 Hz), the response of the shear-test apparatus, given the assumed properties, was found not to influence joint response significantly. However, information was not available on the actual stiffness of components of the test apparatus. A new set of simulations with a more complete material characterization is required.

If explosive shock loading is simulated, the presence of high-frequency components in the input pulse may affect joint response. This phenomenon should also be investigated.

4.3 LABORATORY CHARACTERIZATION OF JOINTED ROCK

The types of tests to be performed for jointed-rock characterization include: (1) basic material properties, (2) jointed tuff interface characterization, (3) joint response for pseudostatic direct shear, (4) joint response for harmonic load, (5) joint response for ground-shock load, and (6) joint response for earthquake load. The first three types of tests are aimed at determining basic tuff matrix and joint properties while the last three are performed for analyzing dynamic behavior of joints.

4.3.1 Specimen Preparation/Testing Activities

4.3.1.1 Direct Shear Specimen Preparation

During this reporting period, ten direct shear test specimens have been prepared. Specimen preparation is expected to continue at a rate of five specimens every 2 weeks.

4.3.1.2 Uniaxial and Triaxial Compression Specimen Tests

Forty-five uniaxial specimens and five triaxial specimens have been tested. The test results for the uniaxial and triaxial compressive tests are listed in Table 4-3 and 4-4, respectively.

Statistical analysis gives a mean uniaxial compressive strength of 23,255 psi (with a standard deviation of 3,750 psi) and a mean triaxial compressive strength of 28,674 psi (with a standard deviation of 2,743 psi) with 500-psi confining pressure. Typical values for Young's modulus and Poison's ratio of the Apache Leap tuff are 5.4 x 10^6 psi and 0.2, respectively.

4.3.1.3 Brazilian Disk Tension Specimen Tests

A total of 27 Brazilian disk tension specimens have been tested and the results are given in Table 4-5.

Table 4-3. UNIAXIAL COMPRESSIVE STRENGTH OF APACHE LEAP TUFF

Sample No.	Failure Stress (psi)	Sample No.	Failure Stress (psi)
SRM28.2.3-U-1	25,700	SRM10.1.1-U-2	22,180
SRM28.3.4-U-2	15,200	SRM10.1.1-U-1	24,100
SRM1.3.3-U-1	22,240	SRM26.2.3-U-1	23,820
SRM16.1.1-U-2	30,210	SRM13.3.4-U-2	27,240
SRM16.1.1-U-1	26,840	SRM22.1.1-U-1	25,210
SRM1.3.3-U-2	24,490	SRM27.3.4-U-3	27,660
SRM28.1.1-U-2	19,450	SRM28.3.4-U-1	16,430
SRM28.1.1-U-1	17,650	SRM28.1.2-1-U-1	17,760
SRM25.1.1-U-3	18,930	SRM17.2.3-U-2	22,400
SRM25.1.1-U-2	16,580	SRM28.2.3-U-2	23,790
SRM15.3.4-U-2	25,100	SRM15.3.4-U-1	25,160
SRM15.2.2-U-2	21,470	SRM23.1.2-U-1	23,050
SRM27.3.4-U-2	26,820	SRM23.3.4-U-1	25,260
SRM13.3.4-U-1	27,140	SRM23.3.4-U-2	20,180
SRM15.2.2-U-1	25,710	SRM1.2.2-U-1	24,360
SRM22.1.1-U-2	20,890	SRM22.5.5-U-2	31,660
SRM13.2.3-U-1	22,780	SRM1.1.1-U-2	23,660
SRM27.3.4-U-1	21,770	SRM15.2.3-U-1	23,800
SRM25.1.1-U-1	16,280	SRM1.1.1-U-1	25,080
SRM17.2.3-U-1	17,470	SRM26.2.2-U-2	24,570
SRM22.5.5-U-1	27,400	SRM26.2.2-U-1	25,730
SRM29.2.4-U-3	24,510	SRM29.2.4-U-2	25,520
		SRM29.2.4-U-1	22,330

Table 4-4. TRIAXIAL COMPRESSIVE STRENGTH FOR APACHE LEAP TUFF

Specimen No.	Confining Pressure (psi)	Failure Stress (psi)
SRM25.1.1-T-2	500	30,190
SRM17.2.3-T-1	500	24,780
SRM16.1.1-T-1	500	29,800
SRM23.3.4-T-1	500	31,600
SRM1.3.3-T-1	500	27,000

Table 4-5. UNIAXIAL COMPRESSIVE STRENGTH OF APACHE LEAP TUFF

Sample No.	Failure Stress (psi)	Sample No.	Failure Stress (psi)
SRM23.3.4-B-1	1,870	SRM1.3.3-B-2	790
SRM10.1.1-B-1	1,760	SRM1.3.3-B-1	825
SRM10.1.1-B-2	1,990	SRM17.2.3-B-1	1,730
SRM10.1.1-B-3	1.690	SRM17.2.3-B-2	1,470
SRM23.1.2-B-1	1,740	SRM17.2.3-B-3	1,440
SRM23.1.2-B-2	1,710	SRM13.5.7-B-3	2,320
SRM23.3.4-B-2	1,840	SRM13.5.7-B-1	1,460
SRM28.2.3-B-1	1,680	SRM13.5.7-B-2	1,580
SRM28.2.3-B-2	1,320	SRM21.1.2-B-1	1,810
SRM28.2.3-B-3	1,550	SRM21.1.2-B-2	1,510
SRM28.1.2-1-B-1	1,210	SRM16.1.1-B-1	2,355
SRM28.1.2-1-B-2	1,450	SRM16.1.1-B-2	1,455
SRM15.3.4-B-3	1,210	SRM15.3.4-B-2	1,440
SRM15.3.4-B-1	1,570	SRM16.1.1-B-2	1,570
SRM1.3.3-B-3	880	SRM16.1.1-B-4	1,190

4.3.2 Jointed Tuff Interface Characterization Tests

The parameters required for joint-interface characterization for various analytical joint models are different, and the methodologies for acquiring them also vary. One important parameter for characterizing the Barton-Bandis joint model is the joint-roughness coefficient (JRC). The determination of this parameter requires profile measurements of a rock-joint surface.

The "rock profiler" (Figure 4-15) is a noncontact surface-height gauging profilometer. It has been assembled primarily from off-the-shelf equipment including an Asymtek A-102B benchtop gantry-type X-Y-Z positioner and a Keyence LC-2100/2320 laser displacement meter. An LC-2320 red visible laser head, with specified displacement measurement resolution of about 0.5 micron, is attached to the Z-axis of the A-102B X-Y-Z gantry positioner.

A rock positioned beneath the A-102B is profiled by scanning the LC-2320 across the rock surface in the X- and Y-axis directions in a raster-scan pattern. The LC-2320 has a measurement window of about ±8 mm from a standoff position of about 50 mm. The LC-2100/2320 combination form the laser displacement meter, which operates on a principle of triangulation, i.e., the apparent shift in the position of a laser light spot, as the laser head is raised or lowered, indicates displacement.

The rock-profiler movements are controlled by PC/AT commands to the A-102B X-Y-Z table by way of a serial communications port. The A-102B table has a built-in computer for interpreting high-level commands from the PC/AT and then executing the
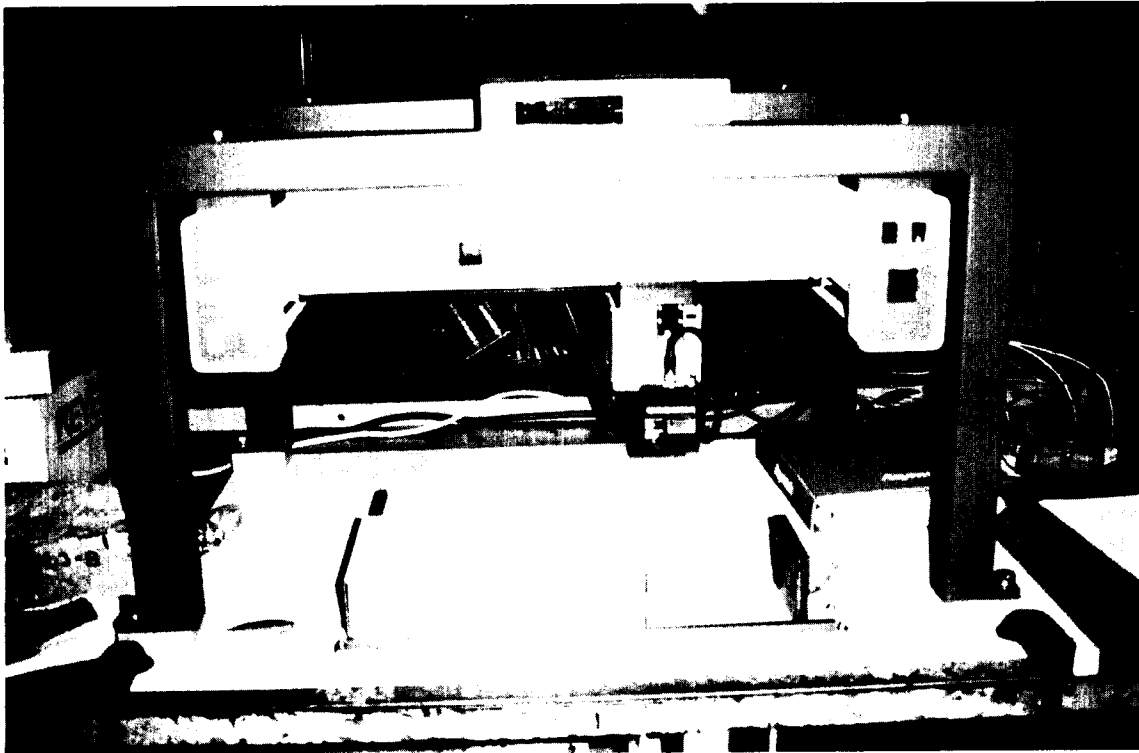
Figure 4-15. Profilometer for joint surface profile measurement

moves. A custom computer program written in Borland's TurboC, Version 2.0, issues movement commands to the A-102B to (1) read the displacement-measurement Z-axis movement from the LC-2100 and (2) format and store pertinent scanning and rock-profile displacement information to a PC/AT floppy or hard-disk data file. Additional software modifications were also made to further extend the rock-profiler measurement range from ±8 mm to about ±25 mm, as the rock-surface variations exceeded the originally assumed range of ±8 mm. The Z-axis of the A-102B is used to accomplish this greater range.

4.4 NEVADA TEST SITE DATA COLLECTION ON GROUND-SHOCK EXCITATION

Essential documents for the collection of Nevada Test Site (NTS) ground-shock data have been obtained. These documents contain the requisite data such as: (1) site geology and geometry of underground facilities, (2) block-motion observations, (3) ground motion, (4) material properties for both effective rock mass materials and discrete geologic features, and (5) tectonic stress-magnitude and direction measurements.

A significant body of block-motion data, resulting from high-explosive near-surface source events, was accumulated by the Air Force Weapons Laboratory (AFWL) during field tests of the high-explosive-simulation technique (HEST) and the direct-induced high-explosive-simulation technique (DIHEST). These tests used high explosives buried in a geometric array to produce desired particle velocity history at a given range from the array. A series of tests was carried out in three rock types: layered sedimentary, soft weathered tonalite or quartz diorite, and hard quartzite, in which block-motion data were recorded.

4-16

Several of these tests have been rated as having excellent to good quality block-motion data. Data from three of these tests (two in tonalite and the other in quartzite) will become part of this block-motion database.

Block-motion data were also observed on contained underground tests (UGTs) at the NTS, including events within the Tunnel Beds Formation of Rainier Mesa, which consists of partially saturated, zeolitized, bedded ashfall tuff. These tests used nuclear explosives buried in an underground tunnel or shaft to produce the shock wave. Data-collection efforts for nuclear tests where block motion was observed have concentrated on measuring the maximum extent, direction, and magnitude of relative displacements across geologic discontinuities. Among the tests, two have been selected as part of this block-motion database.

The five cases that are being summarized are listed in Table 4-6 below.

Table 4-6. FIELD TESTS FOR BLOCK-MOTION DATABASE

Event	Test Date	Rock Type	Number Observed	Event Yield	Saturation	Test Type
HANDEC II	8/69	Tonalite	3	very small	unsat.	DIHEST
ROCKTEST II	3/70	Tonalite	3	small	unsat.	DIHEST
STARMET	11/70	Granite	4	very small	unsat.	DIHEST
MIGHTY EPIC	5/76	Tuff	18	moderate	part. sat.	UGT
DIABLO HAWK	9/78	Tuff	30	moderate	part. sat.	UGT

During the late 1960s, AFWL was charged with the development of techniques using high explosives to simulate the airblast, airblast-induced, and cratering-induced ground motions as part of the Hard Rock Silo nuclear-design threat. HEST tests were used to simulate the airblast and airblast-induced ground motion and consisted of a cavity of uniform height bounded on the sides by a soil berm, above by a soil overburden of uniform thickness, and below by the testbed. DIHEST tests were used to simulate the cratering-induced motions and consisted of a series of collinear boreholes with multiple high-explosive charges equally spaced along each hole.

In the sequence of AFWL's test program, HANDEC II and ROCKTEST II tests were among the later tests conducted at the Cedar City, Utah, facilities. These tests were a combined HEST-DIHEST test which were to simulate a combined airblast overpressure and direct induced ground-shock pulse. The HANDEC II test was shot during August 1969, and ROCKTEST II was performed seven months later, in March 1970.

Data from these two tests include up to 2.8-foot joint displacements in silo walls, blocks thrust 2 feet bound by distinct joints, heaving of silo closure units by 3 to 4 feet,

opening and slipping upward of continuous cracks measuring up to 11 feet, and cratering near explosive array areas.

The third AFWL test selected for this block-motion database is from the STARMET test. This test was conducted in November 1970 at the Pedernal Hills test site in central New Mexico. The test occurred in a metamorphic quartzite rock formation. Only a DIHEST array was used and is the smallest in size of testbeds and pounds of explosives of the cases selected. What was different about this test was that the test-bed rock was quite strong; but it had about a 50-percent soil overlay, and displacement occurred primarily along a single feature delimiting a large thrust block. Table 4-7 summarizes the data from these three tests that are considered useful for the purposes of the study.

The other two cases selected for this database are UGTs from the Rainer Mesa Area of the NTS. The MIGHTY EPIC horizontal line of sight (HLOS) event was conducted on May 12, 1976; and nearly two and one-half years later on September 13, 1978, the DIABLO HAWK event was conducted in the same general vicinity. Part of the MIGHTY EPIC tunnel and support systems were designed to be reused by the DIABLO HAWK event. The concept afforded the DNA block-motion community the opportunity to study block-motion effects in previously loaded rocks. The tunnels were located 1300 feet below surface, and the water table was over 3000 feet below surface. Faults were extensively mapped on the surface and at depth for which nine were considered throughgoing. Extensive tests have been run on the tuff rocks; and, thus, intact material properties are considered to be well known. Fault and joint properties, on the other hand, have not been well characterized. Because of the depth of the test, *in situ* stresses were carefully measured in and around the test area. Table 4-8 gives a summary of block-motion data recorded from these two tests.

It is believed that the final document containing the block-motion database will be an unclassified document with unlimited distribution status. Effort is currently being spent assembling the document, which should be ready for review during the next quarter.

4.5 FIELD INVESTIGATION

The second CNWRA research program quarterly report (CNWRA, 1990) discussed the instruments to be installed at the Lucky Friday Mine. The instruments are used to study the effects of repetitive seismic events on the underground openings and long-term water-pressure changes in faults or other structural features in the rock mass. These instruments include extensometers to monitor long-term displacement of rock mass around underground openings, triaxial velocity gauges to determine the transient response of the rock at excavation surfaces, tape extensometer to monitor opening closure, piezometers to measure pore water-pressure changes in the packed-off regions of a borehole, and a hydrophone to monitor ground shock at a location in the borehole. Conceptual schematic diagrams for the data acquisition systems for extensometer and piezometer readouts and ground-motion monitoring are provided in Figures 4-16 and 4-17. During this quarter, calibration of ten 5-anchor extensometers and two triaxial velocity gauges has been completed.

Table 4-7. HANDEC II, ROCKTEST II, AND STARMET DATA SUMMARY

Item	Radial Range (ft)	Strike (deg)	Dip (deg)	Total (ft)	Component of Displ. (ft)	Comments
HANDEC II						
Silo S-1	115	N46W	25NE	2.6	2.4 LL,SS 1.5 R,DS	Movement along preexisting joint (jt.)
Silo S-2	95	N11E	65E	2.1	LL,SS	Movement along preexisting jt.
SW corner	120	NS	30W	2.62	NA	Testbed movement along low-angle jt.
Silo 5-11	105	N72W	29E	1.5	R,DS	Shear surface in structure
ROCKTEST II						
Joint	200	N10W	20	11.7	R,DS	Clay filled and/or iron stained
Silo S-05	125	N53W	Vert	>0	LL,SS	Joint in silo, clay filled
Joint B	130	N38W	28NE	0.58	R,DS	Not mapped pretest
STARMET						
Thrust block	55	N30E	67NW	5.6	2.5 RL,SS 5 R,DS	NW quadrant of testbed, avg. displ.
Silo W-5	35	N35E	67NW	5.4	R,DS	Joint iron-stained testbed ctr. line
Silo W-6	36	N35E	67NW	3.7	R,DS	Same as W-5, 10ft S testbed ctr. line
Silo W-7	45	N35E	67NW	2.3	R,DS	Same as W-5, 29ft S testbed ctr. line

LL = left lateral; SS-strike slip; R = reverse; DS = dip slip; Vert = vertical

Table 4-8. MIGHTY EPIC AND DIABLO HAWK DATA SUMMARY

Item	Radial Range (ft)	Strike (deg)	Dip (deg)	Total (ft)	Component of Displ. (ft)	Comments
MIGHTY EPIC						
Fault 5 bypass	332	NS	60E	2.2	1.6 R,DS 1.5 LL,SS	Damp gauge in fault 0.25 in. thick
Fault 5 B drift	407	NSW	70E	1.5	0.8 R,DS 1.3 LL,SS	Damp gauge in fault 0.25 in. thick
Tt3BC/3D	290	N85W	15S	>3	R,DS	Damp clay layer on contact 0.125 in. thick
A drift						
Fault A drift	290	N30E	72W	>0	R,DS,LL,SS	Fault through SRI structure
Fault LOS drift	243	NS	55W	>5.5	R,DS	Fault near #6 in LOS drift
Fault	383	N35E	68NW	2.9	1.5 NS,DS 2.5 LL,SS	Fault in interface drift
Fault 7 A drift	293	N15W	60SW	0	0	Tight and dry
Fault 8 A drift	295	N45W	68SW	0	0	Two planes tight and dry

Vert=vertical; NA=not measured; LL=left lateral; LOS=line of sight; SS=strike slip; R=reverse; DS=dip slip; N=north; E=east; S=south; W=west; ?=unknown; NS=normal slip; Horiz=horizontal

Table 4-8. EPIC AND DIABLO HAWK DATA SUMMARY (Cont'd)

Item	Radial Range (ft)	Strike (deg)	Dip (deg)	Total (ft)	Component of Displ. (ft)	Comments
Fault 7 B drift	404	N15W	70SW	0	0	Tight and dry
Fault 8 B drift	404	N40W	70SW	0	0	Two planes tight and dry
Fault 4 bypass	521	N15W	86W	0	0	Tight
Fault 3 bypass	710	N70E	80SW	0	0	Tight and dry
Fault 2 bypass	1091	N20W	67SW	0	0	Tight and dry
Fault 4 C drift	950	N15E	90W	0	0	Tight
Borehole MH-1	239	25 feet above 4.35 paleo colluvium		4 north 1.7 up		Water-saturated zone in tuff
Borehole MH-1	280	N90E	25S	1.72	1.4 north 1.0 east	At tuff paleo-colluvium interface
Borehole MH-2	310	N90E	25S	4.3	3.9 north 1.4 east	1.3 vert. at tuff paleo-colluvium contact
Borehole MH-2	403	N90E	25S	2.5	2.4 north 0.4 east	0.8 vert. at tuff paleo-colluvium contact

Vert=vertical; NA=not measured; LL=left lateral; LOS=line of sight; SS=strike slip; R=reverse; DS=dip slip; N=north; E=east; S=south; W=west; ?=unknown; NS=normal slip; Horiz=horizontal

Table 4-8. MIGHTY EPIC AND DIABLO HAWK DATA SUMMARY (Cont'd)

Item	Radial Range (ft)	Strike (deg)	Dip (deg)	Total (ft)	Component of Displ. (ft)	Comments
DIABLO HAWK						
Surface fracture	1227	N15W	vert.	1.7	NA	Fracture open at surface 0.1-6.0 in.
Fault 3BP	730	N35W	85W	0	NA	Tight and dry
Fault LOS	630	N25W	80W	0	NA	Tight and dry
LOS-1	530	N17E	65W	0.5	0.4 LL,SS 0.3 R,DS	Pin measurement
LOS-2	443	N47E	82SE	>1.0	>1.0 R,DS	Pin measurement, LOS pipe damage
CB-1	190	N21E	68NW	>1.7	>1.7 R,DS	Pin measurement
AB-1	255	N2E	66E	10.2	10 RL,SS 1.5-2 R,DS	Pin measurement
3BC/3D AB drift	165	N75E	18S	5 to 10	NA	Bedding plane in AB drift
3BC/3D O AX-2	305	N85E	15S	>0	NA	Damaged structure
Fault in AX-4	330	N26E	70W	5.2	NA	Damaged structure

Vert = vertical; NA = not measured; LL = left lateral; LOS = line of sight; SS = strike slip; R = reverse; DS = dip slip; N = north; E = east; S = south; W = west; ? = unknown; NS = normal slip; Horiz = horizontal

Table 4-8. MIGHTY EPIC AND DIABLO HAWK DATA SUMMARY (Cont'd)

Item	Radial Range (ft)	Strike (deg)	Dip (deg)	Total (ft)	Component of Displ. (ft)	Comments
Fault 0 CS 2+80	350	N20E	70W	1.5 to 10	NA	Damage in AB drift
Fault in CY-23	438	N10E	70W	0 to 1.0	NA	Damaged structure and cables
Fault 5 B drift	304	N5E	66E	>1.9	NA	Filled with damp gauge
Fault C drift	348	N30W	66NE	>0	NA	Fault severed TRW short cables
C1 bulkhead	223	N85E	17S	2.0 to 3.5	NA	Bedding planes in Tt4B formation
Fault D drift	290	N25W	75SW	2.0	NA	Secondary fault water tank structure
Fault D1 drift	320	N35W	75SW	1.7	NA	Secondary fault D1 ministructure
Fault 0 AZ5&AZ	350	N35W	75SW	1.1	NA	Movement between structures
Fault 4 O CZ1	282	N15E	80E	0.1 to 1.0	NA	Structure damaged tight and dry
Fault 4 E drift	410	N20E	80E	0.4	NA	E drift offset by tight and dry
Fault 0 Sta. CB1	315	N20E	75W	>1.7	NA	Fault in main reentry drift near sta. CB1
LOS-3	390	N25E	65E	0	NA	No LOS pipe damage pin measurement

Vert=vertical; NA=not measured; LL=left lateral; LOS=line of sight; SS=strike slip; R=reverse; DS=dip slip; N=north; E=east; S=south; W=west; ?=unknown; NS=normal slip; Horiz=horizontal

4-23

Table 4-8. MIGHTY EPIC AND DIABLO HAWK DATA SUMMARY (Cont'd)

Item	Radial Range (ft)	Strike (deg)	Dip (deg)	Total (ft)	Component of Displ. (ft)	Comments
BP-1	940	N25E	60E	0	NA	Pin measurement
CB-4	485	N35E	76SE	0	NA	Pin measurement
CB-5	496	N25W	66SW	0	NA	Pin measurement
CB-6	500	Due N	70W	0	NA	Pin measurement
AB-2	420	N30W	65SW	0	NA	Pin measurement
AB-3	434	N30W	68SW	0	NA	Pin measurement tunnel linear undamaged
AB-4	461	N25W	75SW	0	NA	Pin measurement tunnel linear undamaged
AB-5	589	N25W	85NE	0	NA	Pin measurement
AB-6	604	N15W	75NE	0	NA	Pin measurement
LOS-4	280	N40W	85NE	NA	NA	Inaccessible
BP-2	840	N10W	75E	NA	NA	Inaccessible

Vert = vertical; NA = not measured; LL = left lateral; LOS = line of sight; SS = strike slip; R = reverse; DS = dip slip; N = north; E = east; S = south; W = west; ? = unknown; NS = normal slip; Horiz = horizontal

Table 4-8. MIGHTY EPIC AND DIABLO HAWK DATA SUMMARY (Cont'd)

Item	Radial Range (ft)	Strike (deg)	Dip (deg)	Total (ft)	Component of Displ. (ft)	Comments
BP-3	793	Due N	65W	NA	NA	Inaccessible
BP-4	643	N35W	85NE	NA	NA	Inaccessible
Fault 2 BP-5	590	N35W	77W	NA	NA	Tight and dry inaccessible
Fault 2R BP-6	542	N10E	75E	NA	NA	Tight and dry inaccessible
BP-7	395	N45E	80SE	NA	NA	Inaccessible
BP-8	380	N15E	80E	NA	NA	Inaccessible
BP-8A	377	NA	NA	NA	NA	Inaccessible
Fault 3 BP-9	218	N35W	80SW	NA	NA	Tight and dry inaccessible
Fault 5 BP-10	203	N15E	76E	NA	NA	Damp gauge inaccessible
Fault 4 CB-2	220	N5E	80W	NA	NA	Tight inaccessible
CB-3	395	N10W	82E	NA	NA	Inaccessible
Fault 6 RE-1	258	N35E	88SE	NA	NA	Tight and dry inaccessible

Vert=vertical; NA=not measured; LL=left lateral; LOS=line of sight; SS=strike slip; R=reverse; DS=dip slip; N=north; E=east; S=south; W=west; ?=unknown; NS=normal slip; Horiz=horizontal
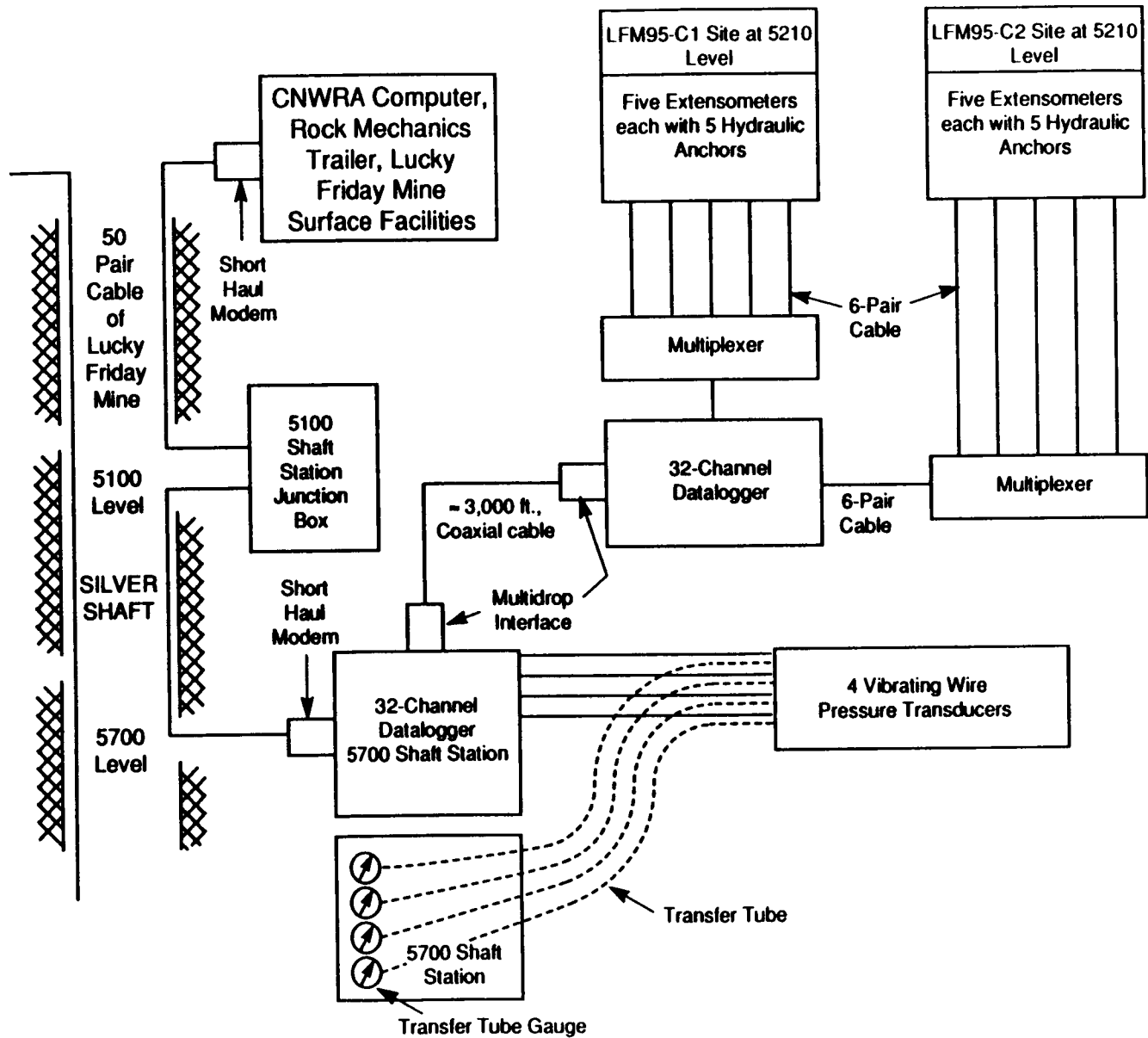
Figure 4-16. Schematic of extensometer and piezometer data acquisition system

50 Pair Cable of Lucky Friday Mine

5100 Level

SILVER SHAFT

5700 Level

U. S. Bureau of Mines Computer, Rock Mechanics Trailer, Lucky Friday Mine Surface Facilities

5100 Shaft Station Junction Box

U. S. Bureau of Mines Computer for Macro-Seismic Network

28 Volt DC Power Supply, Electro-Lab Model 2527

Anti-Aliasing Filter, 500 Hz HF Cutoff, Electro-Lab Model 402 AA

110 Volt DC Power Supply, Lucky Friday Mine

28 Volt DC Power Supply, Electro-Lab Model 28.1

101 Site at 5210 Level — Triaxial Velocity Gauge, Electro-Lab Model 1130 GS

95 Site at 5210 Level — Triaxial Velocity Gauge, Electro-Lab Model 1130 GS

Signal Amplifier, Electro-Lab Model 1131D

Signal Amplifier, Electro-Lab Model 1131D

≈1460 ft, 12 Twisted Pair Cable

≈1560 ft, 12 Twisted Pair Cable

Mine-Wide Macro-Seismic Network of U. S. Bureau of Mines

28 Volt DC Power Supply, Electro-Lab Model 28.1

≈1200 ft, 2 Twisted Pair Cable

Signal Amplifier, Electro-Lab Model 1127-1, 5700 Shaft Station

≈1200 ft, 3 Conductor Cable

Hydrophone, Wilcoxon Research Model H505

110 Volt AC Power Supply, Lucky Friday Mine

Figure 4-17. Schematic of seismic data acquisition system

4.5.1 Five-Anchor Extensometer Calibration

The five-anchor extensometers selected for the field study are Geokon Model A-6G, consisting of three basic components: (1) hydraulic borehole anchors, (2) 1/4-inch-diameter glass-fiber measurement rods and 1/2-inch protective plastic tubes, and (3) hydraulically anchored extensometer head assembly. The relative displacement between an anchor and the head assembly anchor is measured using a linear potentiometer with a maximum range of 2 inches. These devices provide measurements of relative movements along the borehole axis at approximately 5-foot intervals. Figure 4-18 presents one of the five-anchor extensometers.

The ten extensometers were calibrated one at a time through a data acquisition system to be used in the field (as shown schematically in Figure 4-16). Figure 4-19 displays the equipment used for data acquisition and extensometer calibration. The calibration was performed using a National Institute of Standards and Technology (NIST) traceable do-all gauge block set to provide known displacements. The glass-fiber measurement rods of an extensometer were released (disconnected) from the anchors and rigidly clamped into a circular plate at the head assembly end so that the five measurement rods could be calibrated as a unit through the programmed scanning of the datalogger. Gauge blocks with specified thickness were placed between the extensometer assembly head and the plate clamping device used to move the five measurement rods in unison. A total of ten measurements for each measurement rod were taken over a range of relative displacement of approximately 1.6 inches. The calibration was designed in such a way that measurements were taken in both directions with respect to the corresponding linear potentiometers.
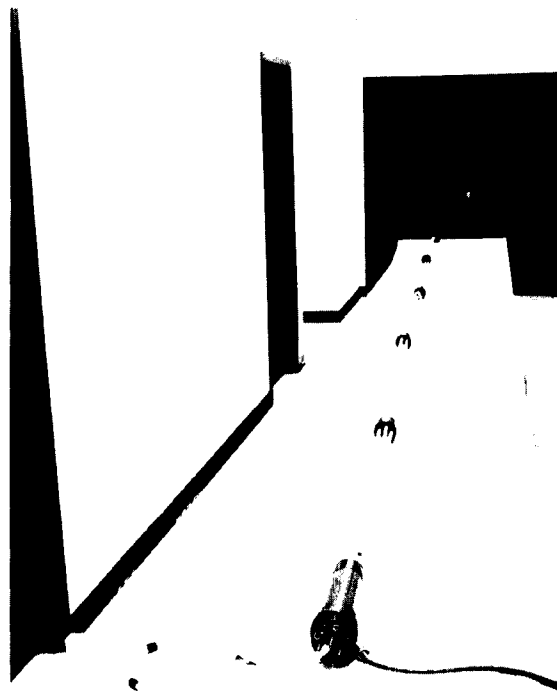
Figure 4-18. Five-anchor extensometer
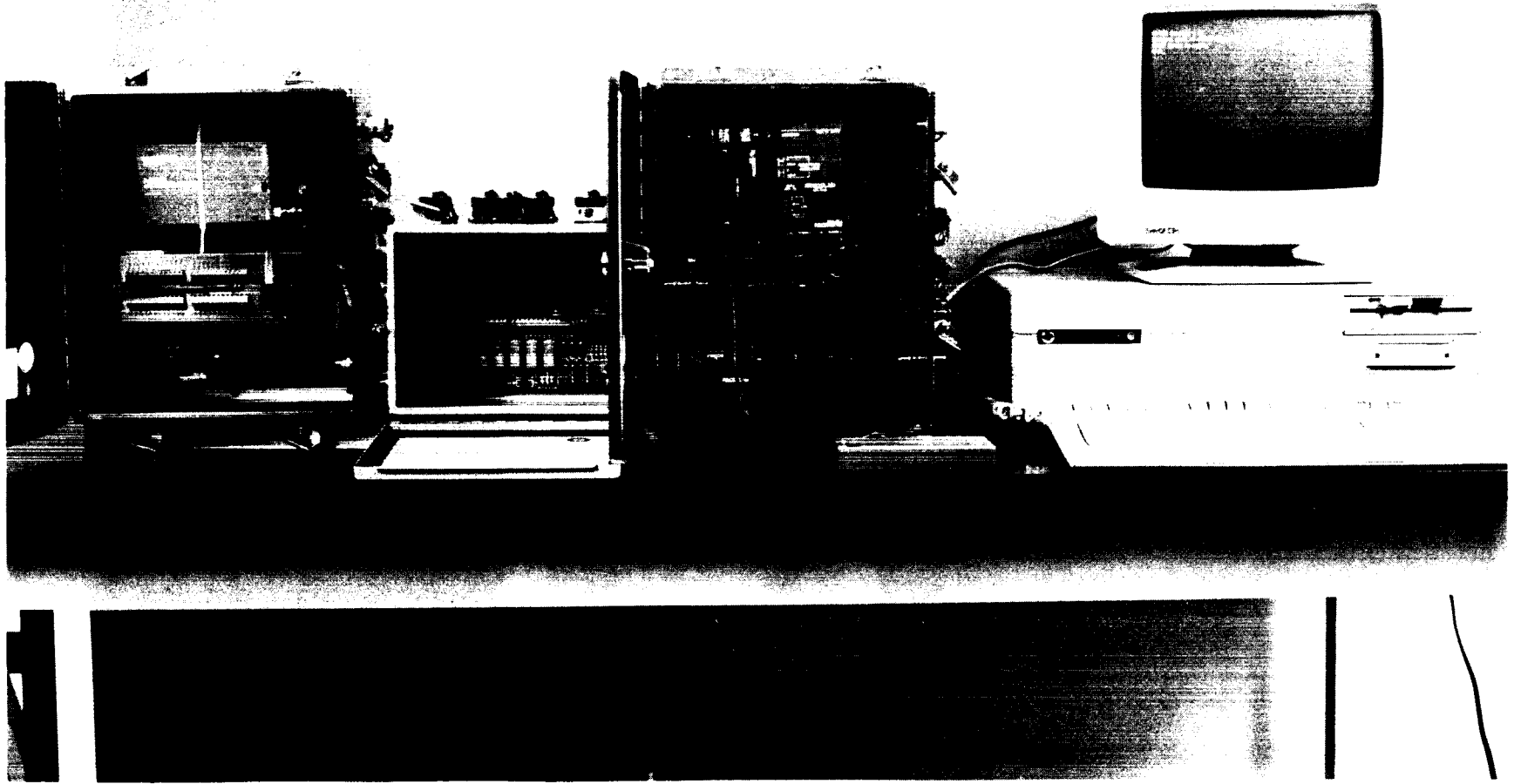
Figure 4-19. Field data acquisition station

After the calibration, data obtained for both gauge block and measurement rods were entered into a Lotus spreadsheet database and normalized against their initial readings. Linear regression analysis was then performed between the normalized gauge block and each measurement rod data set. Table 4-9 presents the calibration data and regression results for a typical five-anchor extensometer. The regression results indicated that, within the range of interest, all 50 linear potentiometers (five for each extensometer) show linear response with respect to rod displacement. The R-squared values are very close to 1.0 for all potentiometers while the corresponding estimated intercepts (listed as "Constant" in the table) are very small for all potentiometers and, therefore, may be negligible. In general, the tangent of the slope (listed as "X coefficient" in the table) for all linear potentiometers ranges from 0.956 to 0.996. These X coefficients will be used as correction factors during actual data collection in the field. Figures 4-20 and 4-21 show typical calibration curve plots.

4.5.2 Triaxial Velocity Gauge Calibration

The objective of the velocity-gauge calibration process was to define the voltage output of the velocity transducers in a defined frequency range for a known velocity input. The results of the calibration process were summarized as both plots and table of the voltage level for the primary and cross-axis terms at defined frequencies, normalized to an input of 1.0 in./sec velocity.

The equipment used in the calibration process can be divided into several basic groups. The first consists of the electrodynamic shaker, associated power amplifier, and servo controller. The electrodynamic shaker has the capability of both vertical and horizontal excitation with a slip table. In this way, the orientation of the test item could be maintained with respect to installation in the field. The servo controller and amplifier are utilized to provide input to the shaker for the closed-loop control process. The servo controller provides the logarithmic swept sinusoidal signal to drive the shaker.

The motion of the shaker was monitored using an accelerometer mounted in close proximity to the test item. For this testing, two accelerometers and associated amplifiers were used. The first was a reference standard accelerometer traceable to NIST. A second, with extended low-frequency and low-acceleration capabilities, was calibrated with respect to the standard accelerometer. Within the frequency and amplitude range of overlap of these two accelerometers, the resulting controls of velocity were identical.

Two triaxial velocity transducers, Electrolab Model 1130GS, were calibrated in the system schematically shown in Figure 4-22, each with a matched amplifier. Cabling was set up to provide a gain of 10dB on the amplifier. The velocity transducer was attached to the shaker through an interface plate, V-blocks, and clamps. The orientation of the velocity transducer was set to match required installation procedures.

The final set of instrumentation was associated with data acquisition, analysis, and display. This was a ZONIC 6088 FFT analyzer with display and printer. The frequency range of the analyzer was set to match the sweep range. The full-scale range and the engineering units per volt for each channel were set as required. The data type

Table 4-9. EXTENSOMETER CALIBRATION DATA CHART FOR MPBX NO. B
(all units are in inches)

Gauge Block		Pos#1		Pos#2		Pos#3		Pos#4		Pos#5	
Readout	Norm	Readout	Norm	Readout	Norm	Readout	Norm	Readout	Norm	Readout	Norm
2.385	0.000	0.21	0.000	0.185	0.00	0.183	0.00	0.172	0.00	0.192	0.00
2	0.385	0.589	0.379	0.562	0.377	0.561	0.378	0.549	0.377	0.569	0.377
1.6	0.785	0.985	0.776	0.957	0.772	0.959	0.776	0.943	0.771	0.963	0.771
1.2	1.185	1.37	1.16	1.34	1.155	1.34	1.157	1.33	1.158	1.35	1.158
0.8	1.585	1.76	1.55	1.73	1.545	1.74	1.557	1.72	1.548	1.74	1.548
1	1.385	1.57	1.36	1.54	1.355	1.54	1.357	1.53	1.358	1.55	1.358
1.4	0.985	1.18	0.97	1.15	0.965	1.15	0.967	1.14	0.968	1.16	0.968
1.8	0.385	0.796	0.586	0.768	0.583	0.77	0.587	0.753	0.581	0.773	0.581
2.2	0.185	0.389	0.179	0.362	0.177	0.361	0.178	0.349	0.177	0.37	0.178
2.385	0.00	0.21	0.00	0.185	0.00	0.181	-0.002	0.171	-0.001	0.191	-0.001

Regression Output for Pos#1

Constant	0.003108
Std Err of Y Est	0.005267
R Squared	0.999915
No. of Observations	9
Degrees of Freedom	7
X Coefficient(s)	0.978959
Std Err of Coef.	0.003417

Regression Output for Pos#2

Constant	0.002208
Std Err of Y Est	0.00512
R Squared	0.999919
No. of Observations	9
Degrees of Freedom	7
X Coefficient(s)	0.975866
Std Err of Coef.	0.003321

Regression Output for Pos#3

Constant	0.001958
Std Err of Y Est	0.005863
R Squared	0.999895
No. of Observations	9
Degrees of Freedom	7
X Coefficient(s)	0.980138
Std Err of Coef.	0.003804

Regression Output for Pos#4

Constant	0.001094
Std Err of Y Est	0.004184
R Squared	0.999946
No. of Observations	9
Degrees of Freedom	7
X Coefficient(s)	0.978553

Regression Output for Pos#5

Constant	0.001404
Std Err of Y Est	0.004018
R Squared	0.999995
No. of Observations	9
Degrees of Freedom	7
X Coefficient(s)	0.978299
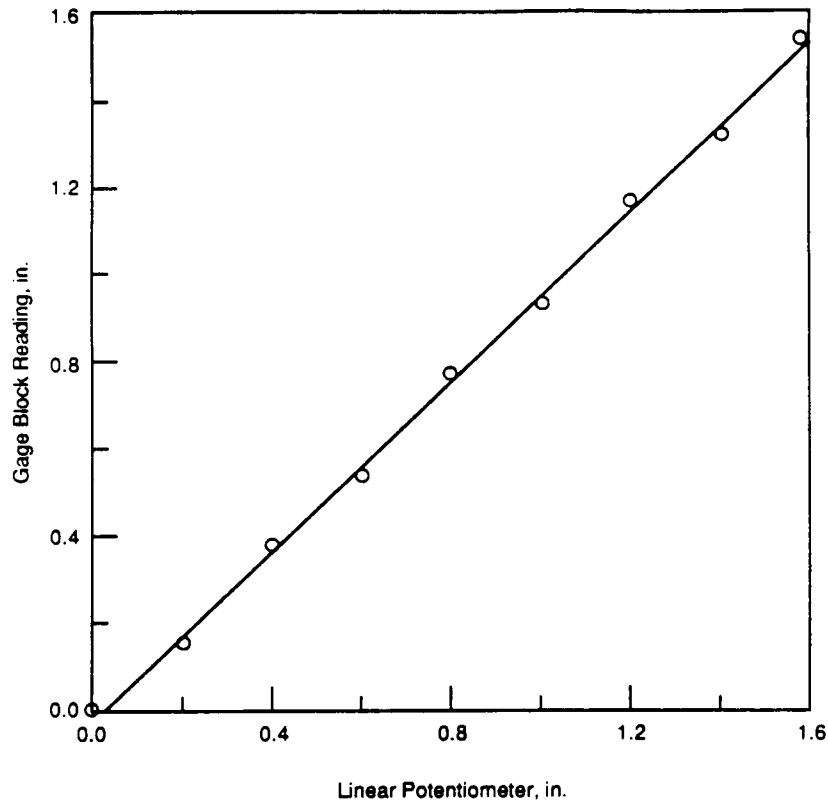
Figure 4-20. Extensometer calibration curve for MPBX No. B, position 3
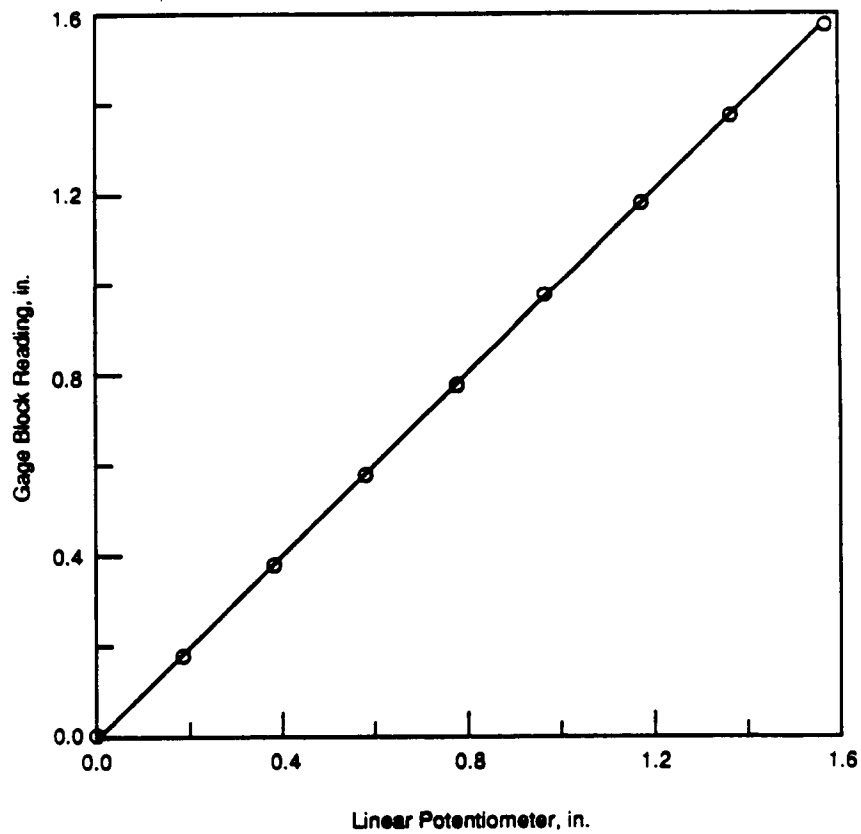
Figure 4-21. Extensometer calibration curve for MPBX No. E, position 3
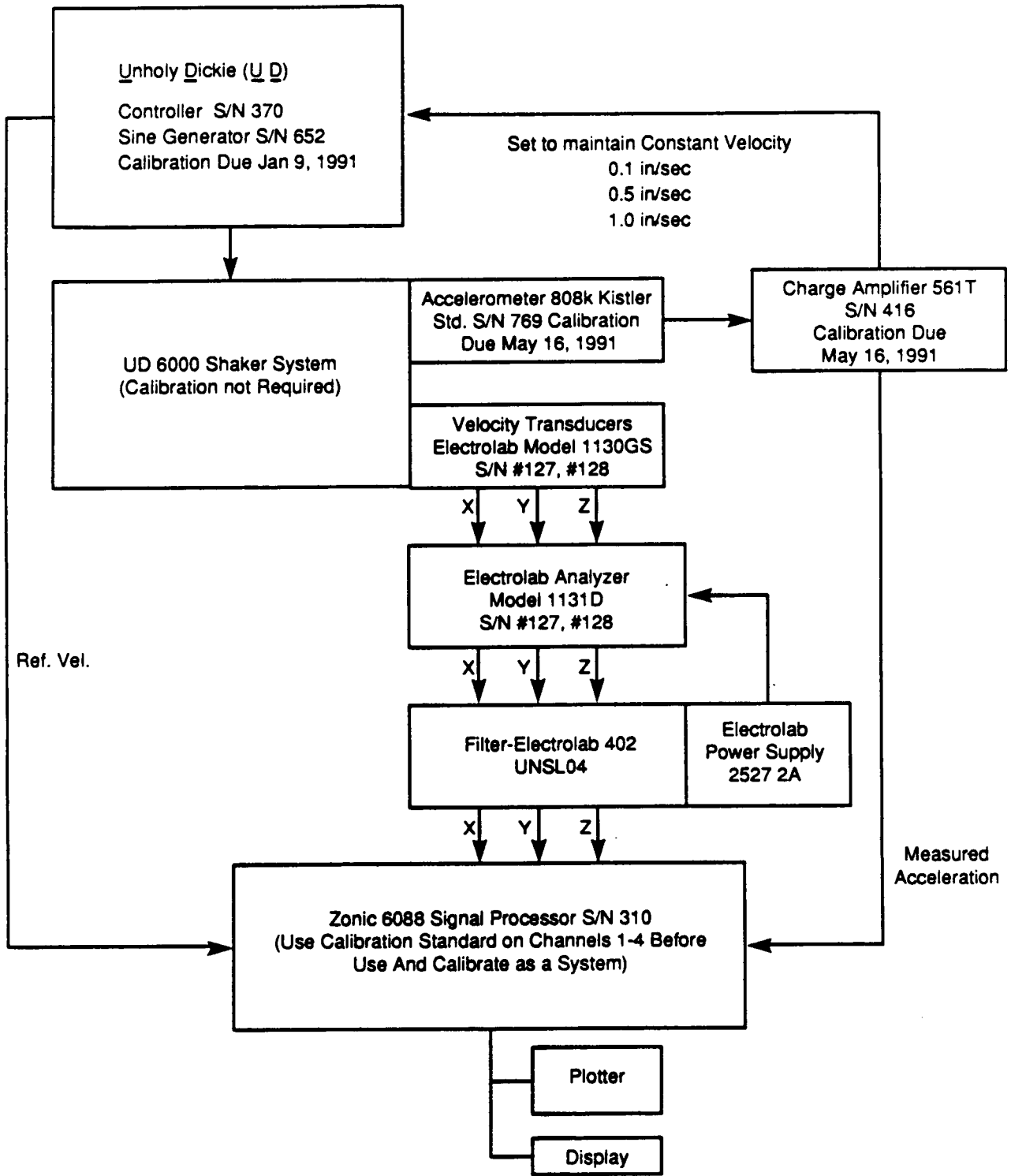
Figure 4-22. Calibration of Electrolab triaxial velocity transducers

was set to "periodic" with continuous sampling with no data overlap. The number of samples for a given test was a function of the sweep time and cutoff frequency range of the analyzer.

The majority of the data is presented in the frequency domain, i.e., amplitude as a function of frequency. The frequency-domain data are presented in terms of a transfer function relating the output voltage to a constant-amplitude sine-wave signal. For a logarithmic swept signal, a transfer function to obtain a flat output for a constant-level input because of the number of samples in each frequency interval. The level of the constant-amplitude sine wave was set such that the transfer function gave results in terms of volts for a velocity level of 1 inch per second.

Plots were obtained for the voltage output of the velocity transducer in the direction of excitation and the two cross-axis terms (Figure 4-23). In addition, tables were obtained for the voltage levels for primary axis as a function of frequency. Limited time-history output was provided to obtain some indication of the shape of the voltage output of the velocity transducer in relation to the input acceleration.
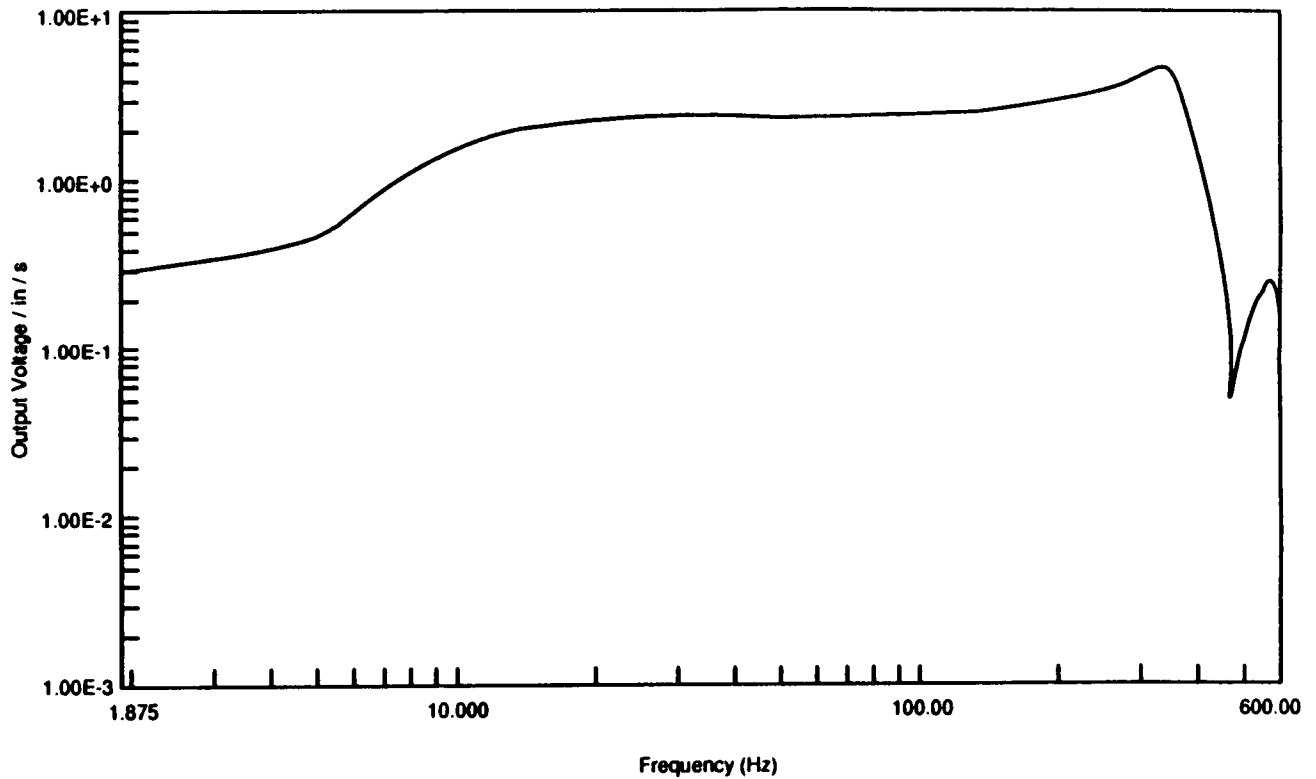
Figure 4-23. Output voltage in the principal excitation direction (X-axis for this plot) vs. frequency

The final calibration gave similar results for the primary sensitivity axis for each transducer. The voltage output is not constant for a constant-velocity input throughout the entire frequency range, nominally 2 to 500 Hz (Figure 4-23). Because of the design of the transducer, a low-frequency roll-off occurs below 20 Hz. In the high-frequency range, roll-off caused by the filters is evident. Between the high- and low-frequency roll-off points, the output voltage is fairly constant.

The transducer has a cross-axis response which, in most cases, is an order of magnitude below the primary axis response and can be ignored.

4.6 REFERENCES

CNWRA. 1990. *Report on Research Activities for the Quarter April 1 Through June 30, 1990.* CNWRA 90-02Q. San Antonio, Texas: CNWRA.

Cundall, P. A., and J. V. Lemos. 1988. "Numerical Simulation of Fault Instabilities with the Continuously Yielding Joint Model." *Proceedings 2nd International Symposium on Rockbursts and Seismicity in Mines.* Minneapolis, Minnesota: University of Minnesota.

Kana, D. D., B. H. G. Brady, B. W. Vanzant, and P. K. Nair. 1989a. *Critical Assessment of Seismic and Geomechanics Literature Related to a High-Level Nuclear Waste Underground Repository.* CNWRA 90-001. San Antonio, Texas: CNWRA: 150.

Kana, D. C., D. C. Scheidt, B. H. G. Brady, A. H. Chowdhury, S. M. Hsiung, and B. W. Vanzant. 1989b. *Development of a Rock Joint Dynamic Shear Test Apparatus.* CNWRA 90-005. San Antonio, Texas: CNWRA:27.

MacDougall, H. R., L. W. Scully, and J. R. Tillerson (compilers). 1987. *Site Characterization Plan Conceptual Design Report.* Sandia National Laboratories (SAND) 84-2641. Los Alamos, New Mexico: SAND.

5. INTEGRATED WASTE-PACKAGE EXPERIMENTS
by Gustavo Cragnolino and Narasi Sridhar

Investigators: *Gustavo Cragnolina and Narasi Sridhar*

5.1 TECHNICAL OBJECTIVES

The technical objectives of the Integrated Waste Package Experiments Project (IWPE) are planned to be accomplished by the following tasks, listed in accordance with the Revision 1 of the program plan:

- Task 1 - Collection and Review of Information for Assessment of Current Status of YMP Corrosion and Materials Program for Waste Package Containers
- Task 2 - Waste Package Experimental Programs
- Task 3 - General Support and Reporting

The current quarterly report follows the above task classification. A second revision of the IWPE program plan was submitted to the NRC on May 23, 1990. Following the approval of the second revision, future quarterly reports will reflect the Revision - 2 task classification.

5.2 WASTE-PACKAGE EXPERIMENTAL PROGRAMS

The objective of the waste-package experiment program task is to provide independently developed data for the NRC to use in the evaluation of information supplied by DOE regarding the degradation of waste package container materials. The experimental program has been divided into two major tasks: (1) corrosion of container materials in the tuff repository environment and (2) metallurgical stability of container materials in the tuff repository environment. The latter task includes studies of hydrogen absorption and embrittlement.

5.2.1 Corrosion of Container Materials in the Tuff Repository Environment

The main activities within the task to investigate corrosion of container materials in the tuff repository environment have been related to (1) performing the initial material and electrochemical characterization of the candidate alloys and (2) determining the effects of environmental variables on localized corrosion of these alloys. The initial material characterization is done to document the microstructural condition of the materials to be tested, the corrosion rate in some standard immersion tests related to intergranular corrosion, and any significant variations found on the surfaces of the materials that may affect long-range performance. The results of the initial material characterization tests were reported in the previous quarterly report (CNWRA, 1990). The electrochemical characterization of the candidate container materials has been designed to elucidate the range of performance of these materials as a function of environmental variables. Localized corrosion (crevice corrosion and pitting) is considered to be one of the most critical of the corrosion processes, and hence emphasis is placed on experimental investigation of these corrosion modes. The cyclic, potentiodynamic, polarization curve has been chosen as the test technique.

The effect of chloride ion concentration in simulated J-13 water on the localized corrosion of two materials, alloy 825 and AISI 304L stainless steel, were reported in the previous quarterly report (CNWRA, 1990). The effects of four environmental species--chloride, fluoride, sulfate, and nitrate--on the localized corrosion of alloy 825 is discussed in this report. These effects were investigated using a two-level, full-factorial experimental design that included a fifth variable, temperature. Additionally, more detailed experiments were conducted to examine the effect of temperature at various chloride levels.

5.2.1.1 Effect of Environmental Variables on Localized Corrosion of Alloy 825

Test Techniques. The specimen and cell configurations used for the tests were similar to those described in ASTM G-5. Platinum gauze was used as the counter electrode. Saturated Calomel Electrode (SCE) was used as the reference electrode, along with a long salt bridge with a Vycor tip so that the reference electrode was at ambient temperature. All potentials in this report will be referred to the SCE at room temperature. The correction for thermal liquid junction potential is estimated to be about 20 mV at 95^0 C and is not considered here. All tests were conducted using either a PAR 173/276 or a PAR 273 potentiostat with a PAR 342C software. In very low chloride environments, especially with the use of the PAR 273 potentiostat, a severe noise problem was encountered with the use of a salt bridge solution of the same composition as the test solution. In these cases, a higher concentration solution, usually a 0.5N KCl solution, was used to mitigate the noise. Following the test, the chloride content of the test solution was measured using a selective ion electrode; and no change in chloride concentration was noted. An Allihn condenser with drip tip and an outlet trap was used to minimize evaporative losses.

Cyclic polarization tests were carried out in accordance with Center's Technical Operating Procedure CNWRA TOP-008, which is similar to the ASTM G-61 procedure. The solutions for the factorial experiments were prepared in accordance with the Center's procedure CNWRA TOP-010. All salts were added as sodium salts to eliminate interference with other cations. The anions that were varied were chloride (6 and 1000 ppm), sulfate (20 and 1000 ppm), nitrate (10 and 1000 ppm), and fluoride (2 and 200 ppm). The lower levels of these anions correspond to the concentrations present in natural J-13 water. Bicarbonate was added to all these solutions to a level of 85.5 ppm. The initial pH at room temperature averaged 8.15 with a standard deviation of 0.08. The final pH at room temperature was 9.34 with a standard deviation of 0.27. As discussed by Murphy (this volume, Section 2.2), these values are in reasonably good agreement with the calculated values. The increase in pH results from ex-solution of CO_2 due to the combined effects of temperature and deaeration of the solution with Argon.

Factorial Design. A two-level, full-factorial design was adopted using five factors--Cl^-, SO_4^-, NO_3^-, F^--and temperature (T). The test trial order was randomized before testing. The five-factor interaction was established to form two blocks of experiments, one using the PAR 173/276 potentiostat and the other using the PAR 273 potentiostat. This approach speeded up the experimentation and at the same time enabled any systematic differences in the instrumental effects to be detected. However, in the eventual analysis, the instrumental differences were considered to be minimal; and four- and five-

factor interactions determined pooled variance. A description of the factorial design can be found in Mason et al. (Mason, 1989).

Electrochemical Observations. Selected polarization curves are shown in Figures 5-1 and 5-2 to illustrate the anodic behavior observed in these tests. As shown in Figure 5-1, nitrate has a major inhibitive effect on pitting in the high chloride environment, since practically no hysteresis was present in the 1000-ppm nitrate solution and the specimen exhibited no pitting. From many of the tests, a poor correlation clearly was evident between the parameters of the polarization curves and the visual evidence of
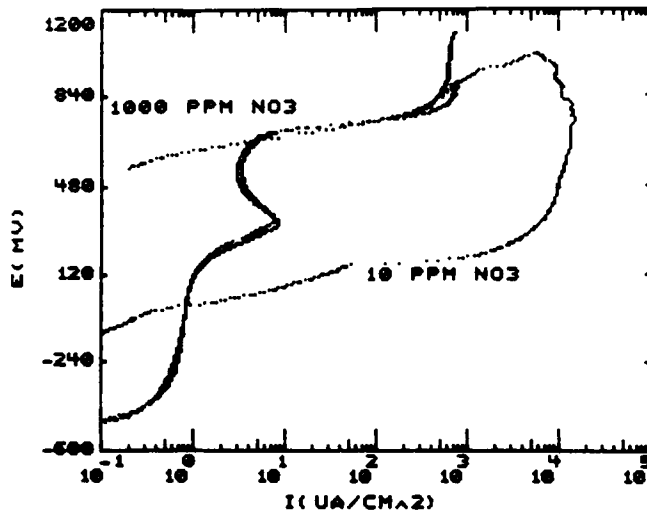

Figure 5-1. Typical cyclic polarization curves for alloy 825 at 95°C indicating the effect of nitrate at a chloride concentration of 1000 ppm
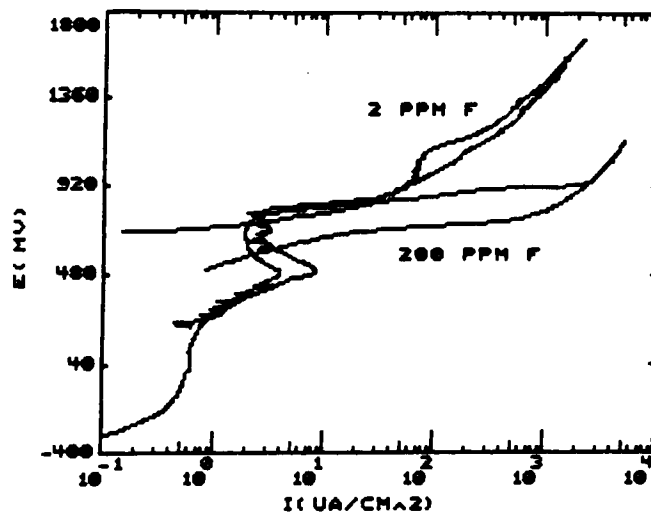
Figure 5-2. Typical cyclic polarization curves for alloy 825 at 95°C indicating the effect of fluoride at a chloride concentration of 6 ppm

5-3

pitting. This was especially true at low chloride contents and low temperatures. For example, as shown in Figure 5-2, the specimen tested in a solution containing 6-ppm chloride and 2-ppm fluoride showed a smaller hysteresis than another tested in a solution containing 6 ppm chloride plus 200 ppm fluoride. However, the former pitted while no pitting was found in the latter. Statistical analysis therefore using just the electrochemical parameters will result in misleading interpretation of environmental effects on pitting. This point is further amplified in later sections.

Visual and SEM Examination. Specimens were examined after the test under a low-power microscope (70X magnification). In selected cases, scanning electron microscopy (SEM) of the specimens was conducted. Five broad classifications were created as shown in Table 5-1. While these ratings are relative, a rating based only on the number of pits per unit area is insufficient to characterize the behavior, since both the depth of pits and type of corrosion products associated with the pits varied. The most severe cases (rating = 4) had not only deep pits, but also crevice corrosion. There were no thick corrosion products deposited on the pits. Specimens with a 3 rating also exhibited deep pits of a similar kind, but did not show extensive crevice corrosion. The pits were found to have considerable undermining beneath the surface.

In some specimens, the pits were quite numerous, but shallow and covered with a brown deposit. No crevice corrosion was observed in these specimens. These were given a rating of 2. Finally, in one specimen, the pits were found to be flat depressions surrounded by brown corrosion product. This specimen was given a rating of 1 to distinguish it from the shallow but narrow pits of rating 2. In the case of specimens exposed to high fluoride environments, a loosely adherent, yellowish film was found to have formed uniformly over the entire surface.

Table 5-1. RATING OF LOCALIZED CORROSION BY VISUAL EXAMINATION

Rating	Description	Corrosion Product
4	Severe pitting, crevice corrosion	Rich in Cr, Mo
3	Less severe pitting, no crevice	Rich in Cr, Mo
2	Shallow, numerous pits	Rich in Fe
1	Shallow, flat areas of corrosion	Rich in Fe
0	No localized corrosion	

The type of pits observed by SEM are shown in Figures 5-3 to 5-5. The case of a severe pitting (rating = 4) is shown in Figures 5-3a and 5-3b. A magnified image of the bottom of the pit indicates a step-type structure outlining the grains, indicating that the corrosion was greater in the grain interiors than the grain boundaries. The specimens rated 3 showed a very similar type of pitting, the essential difference being the lack of crevice corrosion. In an example of a 2 rating, shown in Figures 5-4a and 5-4b, the pits were covered by brownish deposits. A magnified view of one of the pits indicated considerable intergranular attack along with pitting. The specimen rated 1 is shown in Figures 5-5a and 5-5b. As in the case of specimens ranked 2, a brown deposit was found around the pits.
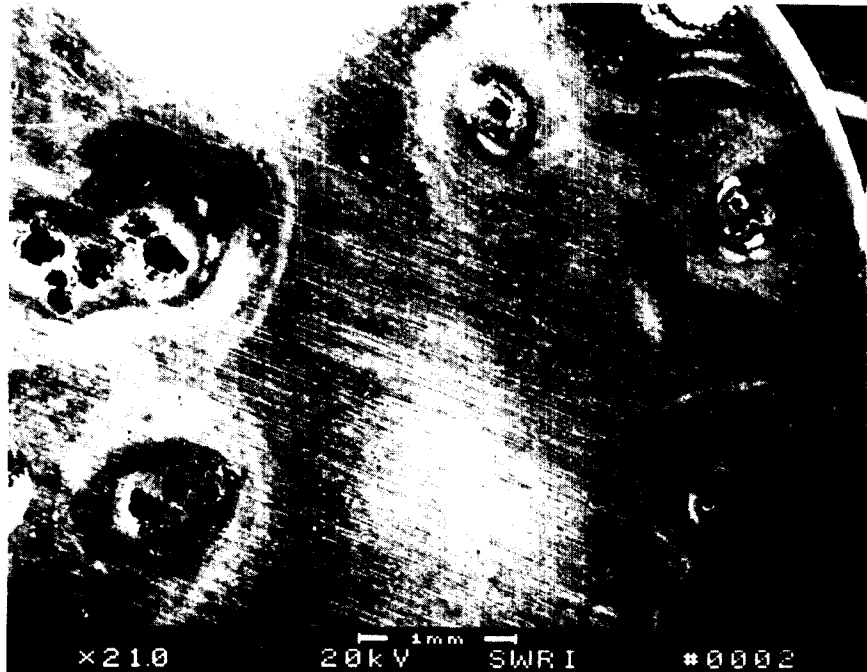
Figure 5-3a. Scanning electron microscope view of pits that were rated 4. Specimens rated 3 also pitted in a similar fashion but without crevice corrosion.
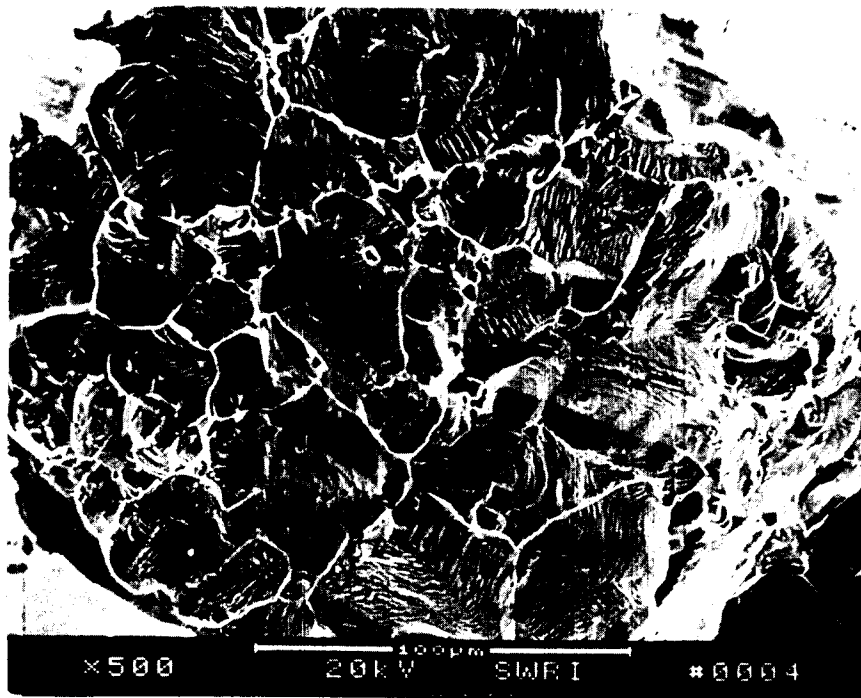
Figure 5-3b. Magnified view of the bottom of a pit shown above exhibiting a transgranular type of attack
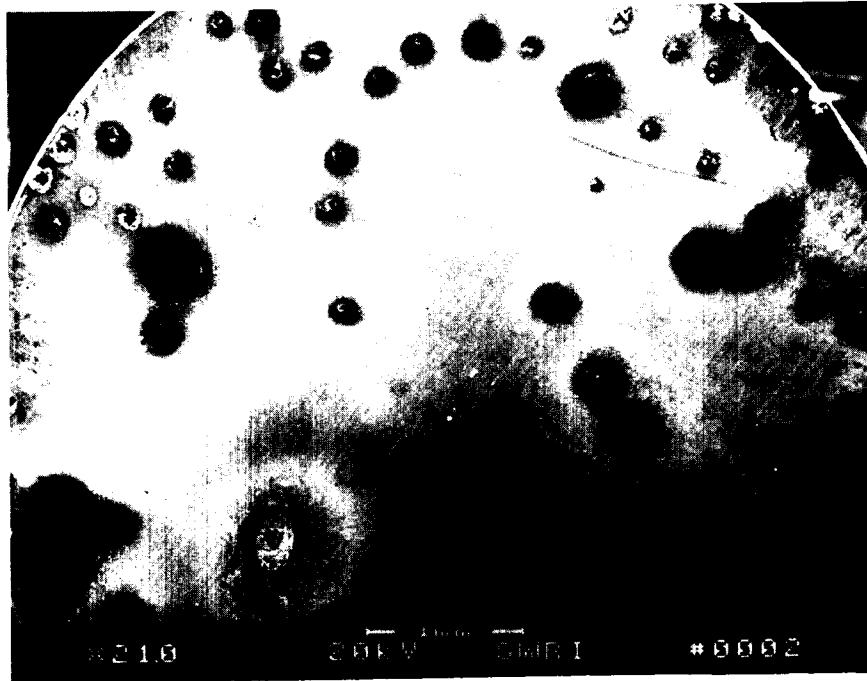
Figure 5-4a. Scanning electron microscope view of pits rated 2
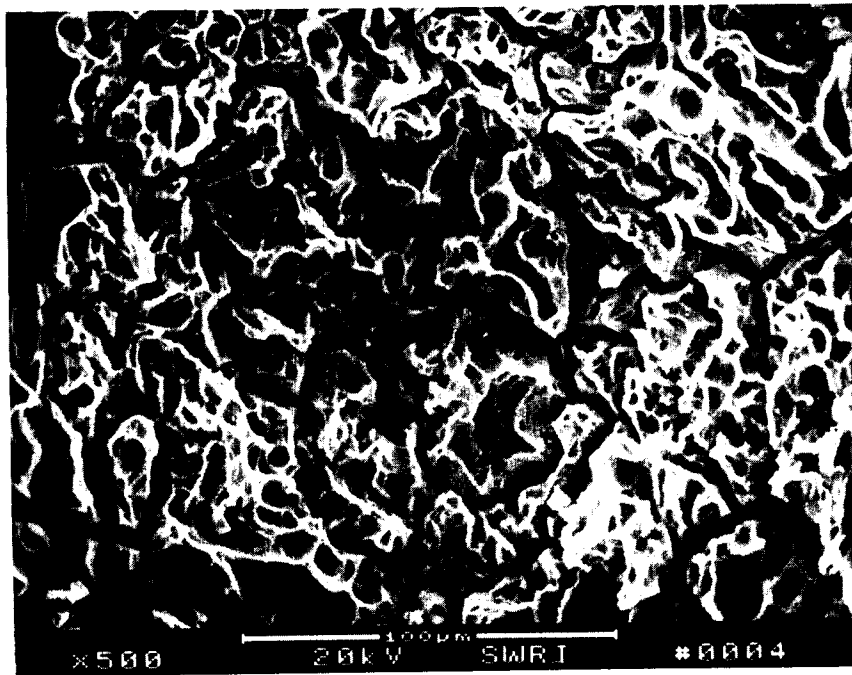
Figure 5-4b. Magnified view of the bottom of a pit shown above. Intergranular attack is evident in these pits.
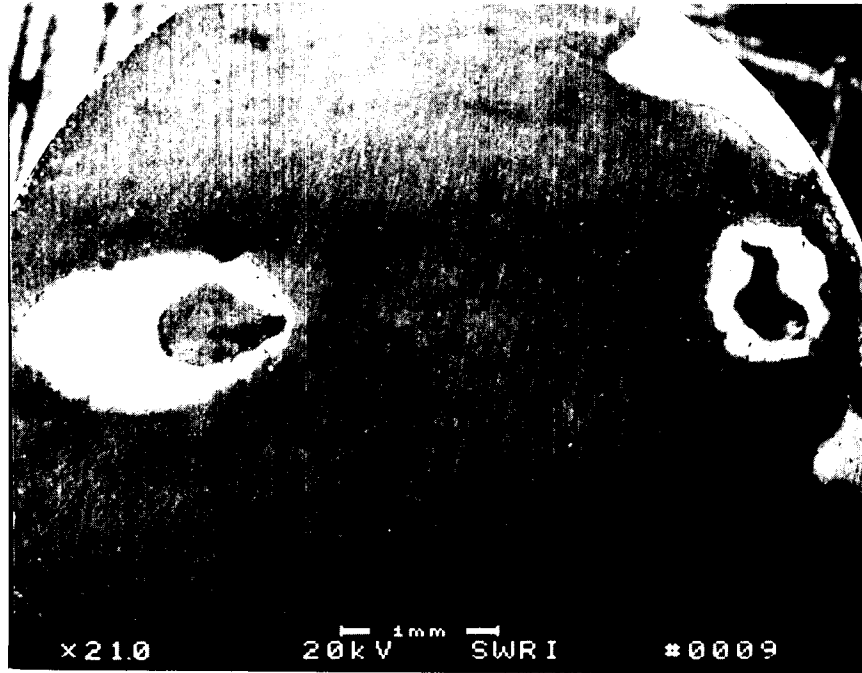
Figure 5-5a. Scanning electron microscope view of pits rated 1
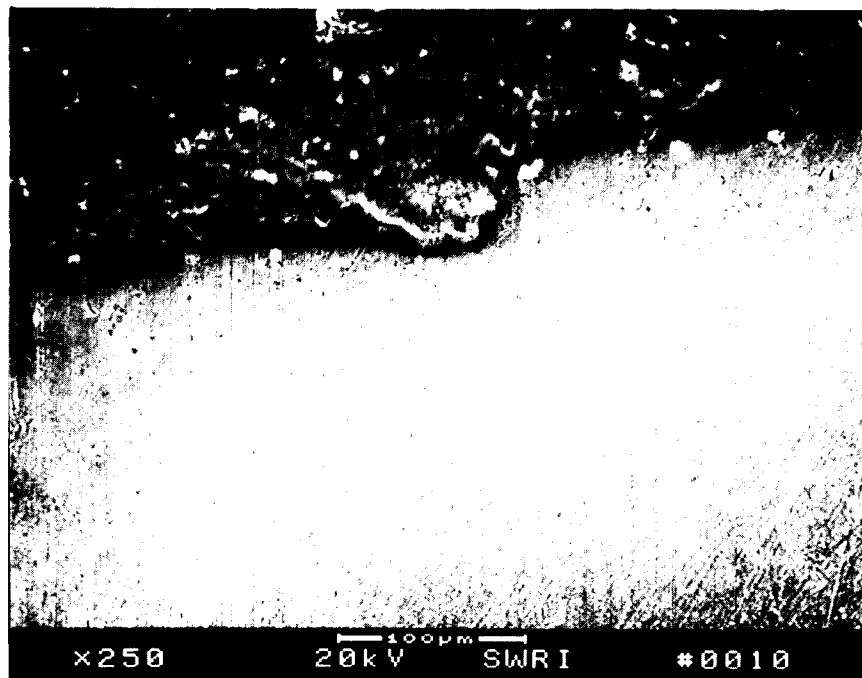
Figure 5-5b. Magnified view of the flat area inside one of the pits above exhibiting uniform corrosion surrounded by corrosion products

Energy dispersive x-ray (EDX) analysis was performed on these specimens. Essentially two types of localized corrosion behavior were observed. In the case of severe localized corrosion (ratings 4 and 3), the corrosion products at the edges of pits were high in Cr and Mo, low in Ni and Fe, and greenish blue in color. The analysis of the bottom of these pits (Figure 5-3b) was similar to that of the base metal. In the case of shallow pits (rating 2) covered by brown corrosion products, the corrosion products were high in Fe and low in Cr and Mo. The absence of Cr in the corrosion products on samples rated 1 and 2 may be related to the high anodic potentials at which these pits were observed. At these potentials, the stable Cr species are the highly soluble hexavalent Cr species, which result in a depletion of Cr at the surface of the sample. The ensuing dissolution causes an Fe-rich corrosion product.

Localized Corrosion Index. In the literature on localized corrosion, the hysteresis in the polarization curve reflected by E_p - E_{rp} is often considered to be a measure of the extent of localized corrosion. In the present investigation, however, this correlation was not always observed. This is illustrated in Figure 5-6 where the visual rating is plotted against the hysteresis, E_p - E_{rp}. A lack of correlation between these two parameters is evident, especially at intermediate and low values of hysteresis. Since both the electrochemical parameter (E_p - E_{rp}) and the visual rating carry part of the information required to characterize the localized corrosion behavior, an index called the localized corrosion index (LCI) was introduced as shown in Eq. (1).

$$LCI = (E_p - E_{rp})^* Visual\ Rating \tag{1}$$
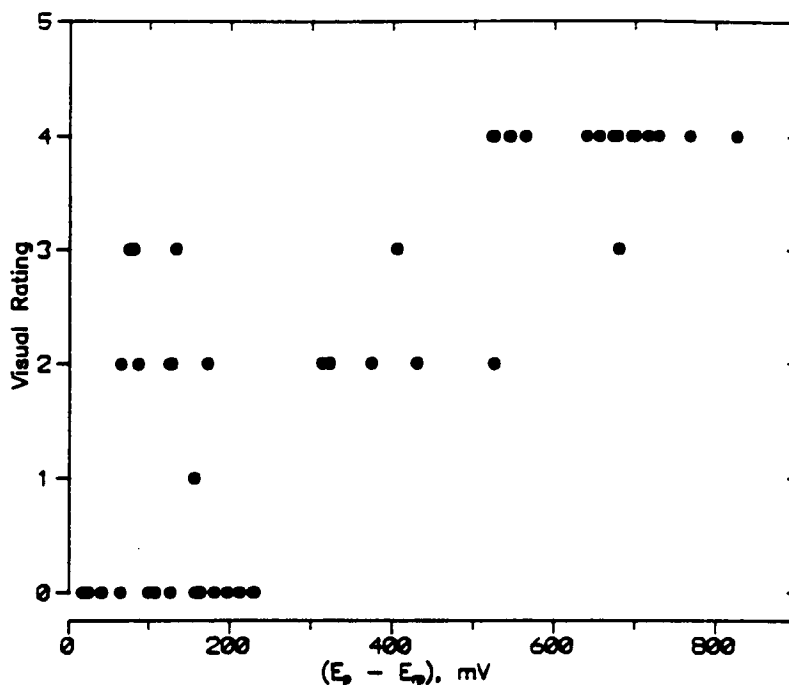
Figure 5-6. E_p - E_{rp} vs. visual rating of specimens indicating a lack of correlation between these two parameters

The LCI is zero in cases where no pitting was observed even if there were a sizable hysteresis. The index also differentiates cases where similar hysteresis is observed with widely varying severity of localized corrosion. The LCI was then used as the measured parameter for statistical analysis. The results of the tests along with the computed LCI are summarized in Table 5-2.

Statistical Analysis of Results. The initial approach was to consider only the main effects of the five variables and the two-factor interactions. The higher factor interactions were then pooled to calculate the variance in the results and to construct the 95-percent confidence intervals for the factor coefficients. Another approach was to consider not only the main effects and two-factor interactions, but also the three-factor interactions. Again, higher order interactions were used for pooled error calculations. Upon inspection of the second analysis, it was evident that the three-factor interactions were not significant, with the possible exception of the temperature-chloride-sulfate interaction term. The three-way interaction of temperature, chloride, and sulfate was dominated by the adverse effect of chloride. Additionally, the statistical model with three-factor interactions was determined to be more complicated than warranted by the test technique. Since the potentiodynamic test approach was expected to yield only trends in the behavior of the material and not life-time predictions, use of more complicated models is of marginal benefit. However, the pooled variance associated with the three-factor model was used in analyzing the results. The residuals from the model and actual measurements exhibited a normal distribution. The resulting equation for localized corrosion is shown in Eq. (2):

$$
\begin{aligned}
LCI = 660 &+ 591(X_{Cl}) - 23(X_T) - 76(X_F) - 587(X_{NO_3}) + 51(X_{SO_4}) \\
&+ 8(X_{Cl}X_T) - 26(X_{Cl}X_F) - 589(X_{Cl}X_{NO_3}) \\
&+ 49(X_{Cl}X_{SO_4}) + 64(X_TX_F) - 32(X_TX_{NO_3}) \\
&+ 41(X_TX_{SO_4}) + 3(X_FX_{NO_3}) + 17(X_FX_{SO_4}) \\
&- 72(X_{NO_3}X_{SO_4})
\end{aligned}
\tag{2}
$$

where LCI = $(E_p - E_{rp})$ * Visual Rating. Note that the parameters X_{Cl}, etc. refer to the coded values and not the actual values of these variables. For example, when the chloride concentration is at the lowest level used in the test matrix, X_{Cl} is -1; and at the highest chloride concentration, it is +1. To convert any concentration of a species A to its coded value, the following equation should be used:

$$
X_A = \frac{2(A - A_{avg})}{(A_{max} - A_{min})}
\tag{3}
$$

where A is the actual concentration of species A and A_{max}, A_{min}, and A_{avg} are the maximum, minimum, and average concentrations, respectively, of species A in the experimental matrix. The R^2 value for the statistical model shown in Eq. (2) was 0.993.

Table 5-2. SUMMARY OF RESULTS OF CYCLIC POLARIZATION TESTS ON ALLOY 825 USING A TWO-LEVEL FULL-FACTORIAL EXPERIMENTAL DESIGN

Trial	Cl^- (ppm)	T (°C)	F^- (ppm)	NO_3^- (ppm)	SO_4^{2-} (ppm)	E_{corr} (mV)	E_p (mV)	E_{rp} (mV)	E_p-E_{rp} (mV)	Visual Rating	LCI
1	6	60	2	10	20	-413	820	756	64	2	128
2	1000	60	2	10	20	-343	678	38	640	4	2560
3	6	95	2	10	20	-447	782	758	24	0	0
4	1000	95	2	10	20	-555	626	82	544	4	2176
5	6	60	200	10	20	-372	807	577	230	0	0
6	1000	60	200	10	20	-541	709	187	522	4	2088
7	6	95	200	10	20	-432	737	610	127	0	0
8	1000	95	200	10	20	-460	593	-87	680	3	2040
9	6	60	2	1000	20	-429	812	679	133	2	399
10	1000	60	2	1000	20	-453	1061	889	172	2	344
11	6	95	2	1000	20	-602	736	662	74	2	222
12	1000	95	2	1000	20	-509	712	672	40	0	0
13	6	60	200	1000	20	-461	776	612	164	0	0
14	1000	60	200	1000	20	-443	778	566	212	0	0
15	6	95	200	1000	20	-590	716	535	181	0	0
16	1000	95	200	1000	20	-593	717	560	157	0	0
17	6	60	2	10	1000	-428	769	644	125	2	250
18	1000	60	2	10	1000	-449	764	108	656	4	2624
19	6	95	2	10	1000	-647	715	715	0	0	0

Table 5-2. SUMMARY OF RESULTS OF CYCLIC POLARIZATION TESTS ON ALLOY 825 USING A TWO-LEVEL FULL-FACTORIAL EXPERIMENTAL DESIGN (Cont'd)

Trial	Cl^- (ppm)	T (^oC)	F^- (ppm)	NO_3^- (ppm)	SO_4^{2-} (ppm)	E_{corr} (mV)	E_p (mV)	E_{rp} (mV)	E_p-E_{rp} (mV)	Visual Rating	LCI
20	1000	95	2	10	1000	-492	713	-3	716	4	2864
21	6	60	200	10	1000	-609	765	568	197	0	0
22	1000	60	200	10	1000	-450	743	179	564	4	2256
23	6	95	200	10	1000	-419	730	574	156	1	156
24	1000	95	200	10	1000	-523	698	-2	700	4	2800
25	6	60	2	1000	1000	-471	895	815	80	2	240
26	1000	60	2	1000	1000	-474	759	631	128	2	256
27	6	95	2	1000	1000	-478	723	707	16	0	0
28	1000	95	2	1000	1000	-555	703	662	41	0	0
29	6	60	200	1000	1000	-437	776	548	228	0	0
30	1000	60	200	1000	1000	-419	666	567	99	0	0
31	6	95	200	1000	1000	-617	721	560	161	0	0
32	1000	95	200	1000	1000	-554	691	583	108	0	0
33	300	95	2	10	1000	-509	728	55	673	4	2692
34	1000	80	2	10	20	-503	686	-10	696	4	2784
35	1000	95	2	10	200	-470	751	-17	768	4	3072
36	1000	95	100	10	20	-545	725	-101	826	4	3304
37	1000	95	2	100	20	-488	709	-20	729	4	2916

Not all the factors in Eq. (2) are of significance, however. Analysis of variance (ANOVA) must be performed on the coefficients in Eq. (2) (Mason, 1989) to determine the statistical significance of the various factor effects. In performing this analysis, the confidence interval so determined is dependent on the standard deviation of the observed electrochemical parameters. This standard deviation can be determined by either repeated tests using a single combination of environmental factors or by assuming that all the higher order interactions involving three or more factors are really due to random errors in the experiments. In the current set of experiments, these two measures of error are approximately equal; and hence the latter was used for estimation of confidence intervals.

Figure 5-7 shows a plot of the coefficients of all the factors listed in Eq. (2) with their 95-percent confidence intervals. It can be seen that for the terms, T, $Cl*T$, $Cl*F$, $T*NO_3$, $T*SO_4$, $F*NO_3$, and $F*SO_4$, the 95-percent confidence intervals of the coefficients straddle zero, indicating that these factors may not be important. On the other hand, Cl, F, NO_3, $Cl*NO_3$, $T*F$, and NO_3*SO_4 are clearly important, since their confidence intervals are clearly displaced from zero. The terms SO_4 and $Cl*SO_4$ are borderline cases and may be included in a more detailed model. Based on the above analysis, a simplified equation for LCI can be expressed as:

$$LCI'' = 660 + 591(X_{Cl}) - 76(X_F) - 587(X_{NO_3}) - 589(X_{Cl} X_{NO_3})$$

$$-72(X_{NO_3} X_{SO_4}) + 64(X_T X_F)$$

(4)
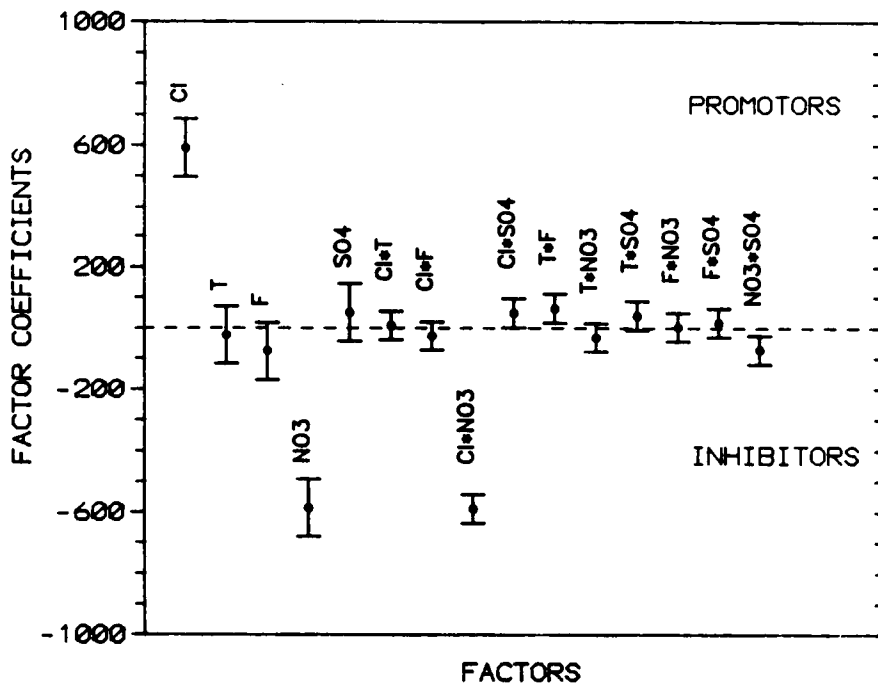
Figure 5-7. The coefficients in Eq. (2) plotted for various factors along with their 95-percent confidence levels

where LCI" has the same meaning as LCI, but the value computed from Eq. (4) will differ from that calculated from Eq. (2). Importantly, the approach used here is not a least squares fit where dropping of terms will be reflected in a change in the coefficients of the remaining terms. The design of the experiment implies orthogonality of all factors, so dropping of any factor will not affect the coefficients of the remaining terms. Dropping of terms, however, will affect the degree of fit of the statistical model to experimental data as reflected by the R^2 value. Thus the R^2 value for Eq. (4) is 0.984, which is still considered to be good.

These equations are valid only within the experimental range of the five factors considered. The interaction effects are exemplified graphically in Figures 5-8 and 5-9. As shown in Figure 5-8, for the low nitrate solutions increasing the chloride concentration increases the LCI; whereas for the high nitrate solutions, increasing the chloride content does not produce a significant change in LCI. If there were no interaction, the slope of the LCI vs. Cl line would be independent of nitrate concentration. The interaction between nitrate and sulfate is shown in Figure 5-9. This interaction is not as pronounced as the previous one.

The experimental design used above can only result in a linear relationship. The predictions from Eq. (2) agree reasonably well with the measured values when the variables are at the extremes of the matrix. However, the deviation from linearity can be visualized by comparing predicted and measured values of LCI at intermediate values of some of the variables using Eqs. (2) and (3) as shown below:
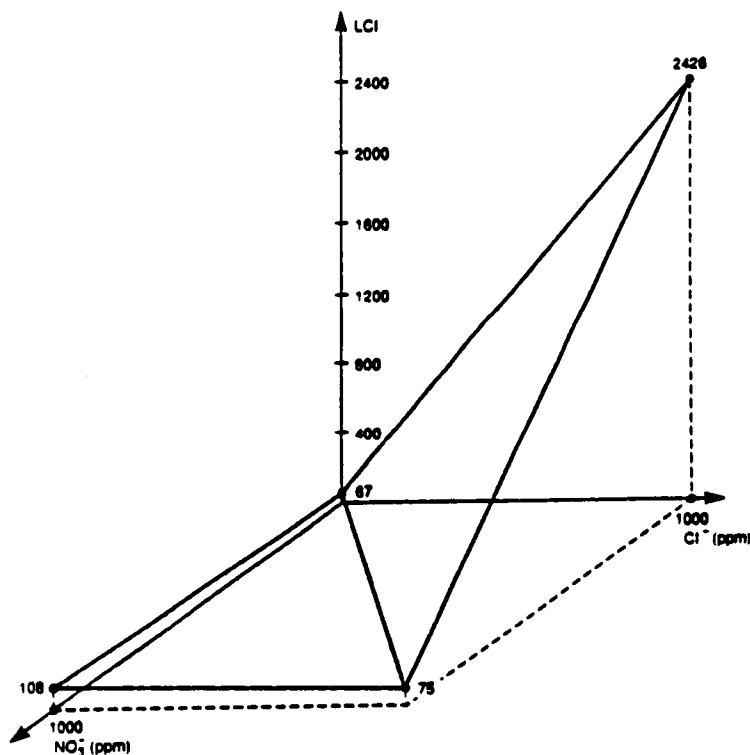
Figure 5-8. Illustration of the interaction between chloride and nitrate in inhibiting localized corrosion

5-13
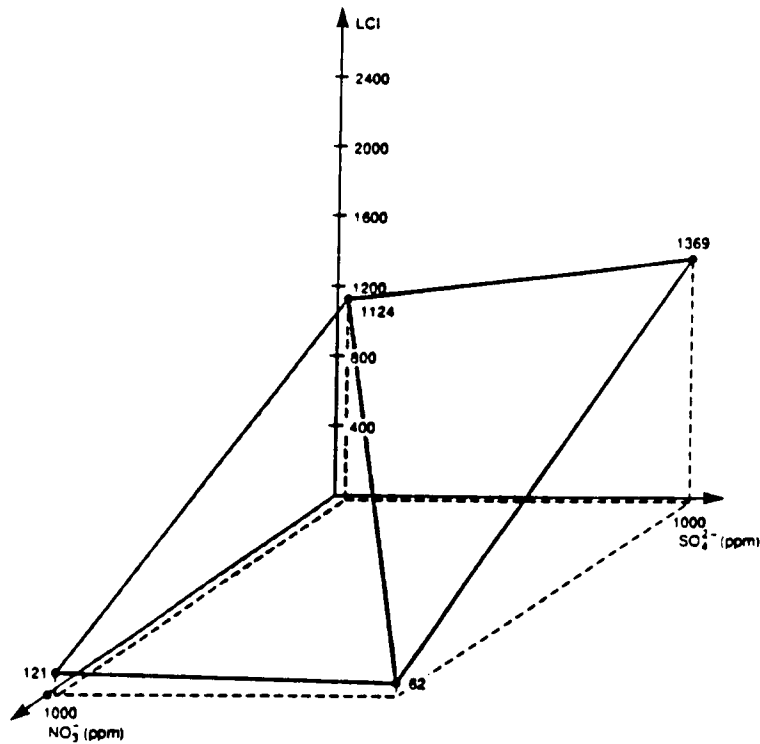
Figure 5-9. Illustration of the interaction between sulfate and nitrate

Case 1: Cl⁻: 300 ppm, T: 95 C, NO_3^-: 10 ppm, F⁻: 2 ppm, SO_4^{2-}: 1000 ppm
         Predicted LCI = 901; Measured LCI = 2692

Case 2: Cl⁻: 1000 ppm, T: 80 C, NO_3^-: 10 ppm, F⁻: 2 ppm, SO_4^{2-}: 20 ppm
         Predicted LCI = 2364; Measured LCI = 2784

Case 3: Cl⁻: 1000 ppm, T: 95 C, NO_3^-: 10 ppm, F⁻: 2 ppm, SO_4^{2-}: 200 ppm
         Predicted LCI = 2361; Measured LCI = 3072

Case 4: Cl⁻: 1000 ppm, T: 95 C, NO_3^-: 100 ppm, F⁻: 2 ppm, SO_4^{2-}: 20 ppm
         Predicted LCI = 2082; Measured LCI = 2916

Case 5: Cl⁻: 1000 ppm, T: 95 C, NO_3^-: 10 ppm, F⁻: 100 ppm, SO_4^{2-}: 20 ppm
         Predicted LCI = 2232; Measured LCI = 3304

        Case 1 shows that the variation of localized corrosion with chloride concentration is far from linear, since the predicted value was much lower than the observed value of LCI. This is discussed further in the next section. Since temperature did not have a significant effect, the predicted LCI at intermediate values of T (case 2) agrees reasonably well with observed values. For the cases of sulfate, nitrate, and fluoride, the deviation from linearity is smaller than observed for chloride (cases 3 through 5).

The results of the factorial experiments clearly illustrate the importance of environmental variables in the development of localized corrosion. The main effect of chloride was similar to that found in the experiments with simulated J-13 water reported in the previous quarterly report (CNWRA, 1990). The experiments revealed lack of a direct correlation, however, between electrochemical parameters (such as pitting potential, repassivation potential and the difference between them) and the visual evidence of pitting. This is particularly true at low chloride concentrations, as shown in Figure 5-2. Specimens without any sign of localized corrosion showed hysteresis values (E_p - E_{rp}) as great as 200 mV. On the other hand, specimens exhibiting a severe attack, as indicated by a rating value of 2, gave rise to polarization curves with relatively low hysteresis values (< 100 mV). Although generalizing these observations to other alloy/environment systems may be questionable, apparently for environments containing low chloride concentrations or certain combination of other anionic species, the simple approach of using electrochemical parameters for quantitative assessment of localized corrosion could be inappropriate. The introduction of the combined index, termed LCI, allows one to overcome that limitation and to establish an unambiguous, albeit subjective, rating for the statistical evaluation of the environmental effects.

As indicated by Eq. (1) and shown graphically in Figure 5-6, chloride and nitrate are the two dominant anionic species in terms of their effect on localized corrosion of alloy 825, chloride being a promoter and nitrate an inhibitor. This is similar to their effect on austenitic stainless steels (Szklarska-Smialowska, 1986). The interactive relationship between these two anionic species is clearly depicted in Figure 5-8, indicating that nitrate inhibits localized corrosion when the chloride concentration is high. In the 6-ppm chloride solution, nitrate does not appear to act as an inhibitor; but the pitting was shallow and different in type (rating 2) from the pitting in the high chloride solutions. Pitting in these solutions occurred at very high anodic potentials in the transpassive region, and a similar type of pitting was found in experiments with zero-ppm chloride solutions at 60°C. The mechanism for this type of pitting is not yet clear. Possibly pitting occurring at high potentials in these types of environments is a form of selective dissolution associated with the transpassive dissolution of Cr.

Eq. (4), a simplified form of Eq. (2), shows coefficients affecting the predominant environmental factors. In addition to the anionic species just discussed, fluoride had a slight inhibiting effect whereas nitrate interacted with sulfate to suppress its weak action as a promoter, as illustrated in Figure 5-9. The inhibiting effect of fluoride was found mainly in the low-chloride solutions (Table 5-2). In all solutions containing fluoride, a loose layer of corrosion product was observed. It is possible that fluoride, acting as a strong complexing agent, promotes uniform rather than localized corrosion. Sulfate was found to be a weak promotor of localized corrosion (Figure 5-6), mainly in high chloride concentrations (Table 5-2). The effect of sulfate found in this investigation is in contrast to the beneficial effect of sulfate found by Leckie and Uhlig (Leckie, 1966) for type 304 stainless steels.

5.2.1.2   Effect of Temperature on Localized Corrosion of Alloy 825

The effect of temperature on the anodic behavior of alloy 825 was studied in simulated J-13 water in which the chloride content was 6 ppm. Figure 5-10 shows a family of potentiodynamic polarization curves obtained at temperatures ranging
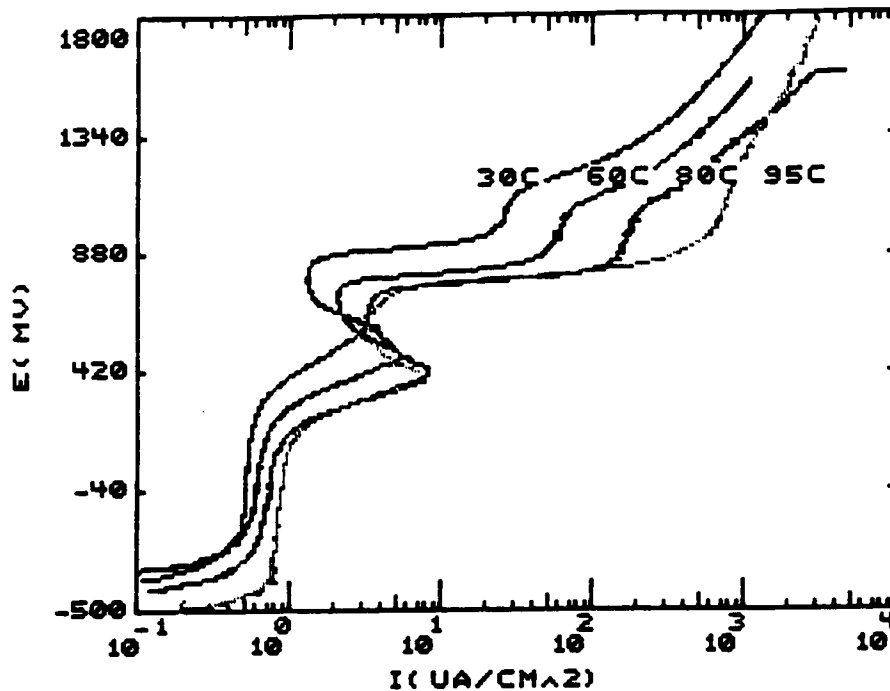
Figure 5-10. Effect of temperature on polarization curves of alloy 825 in a 6-ppm chloride solution

from 30 to 95°C using a scan rate of 0.167 mV/sec. The curves are similar, with the corrosion potential and the transpassive anodic peak displaced to lower potentials with increasing temperature. Also, at potentials above the potential at which the current increases abruptly from the oxygen evolution reaction (CNWRA, 1990), a quasi-limiting current density appears ("a" in Figure 5-10) followed by a region of increasing current. The value of the quasi-limiting current density increases with increasing temperature, but at 95°C this distinctive behavior is no longer observed.

The presence of pits was detected in the specimens tested at temperatures extending from 30 to 80°C. On the other hand, no pitting was observed at 95°C. The pits were quite shallow and covered by brown corrosion products, which were found to be enriched in iron. Intergranular attack was clearly noticeable at the bottom of the pits. According to the observations reported previously, this type of pitting can be classified within the 2 rating. The occurrence of this type of pitting is not related to a characteristic or critical potential, as it is in the case for the pitting observed in more concentrated chloride solutions (>100 ppm). It seems to occur at potentials above that corresponding to the oxygen evolution reaction, precisely within the potential range in which the quasi-limiting current density was observed. This shallow form of pitting was observed, even in the absence of chloride, in a solution of composition similar to simulated J-13 water in which chloride was replaced by sulfate to maintain adequate conductivity. Thus, it appears related to selective and localized transpassive dissolution at very high potentials rather than to localized breakdown of the passive film by the chloride anion. This phenomenon therefore is not realistic in practical terms because such high potentials are not attainable in natural environments even under highly oxidizing conditions.

5-16

The weak effect of temperature on the susceptibility to localized corrosion of alloy 825 within the 60 to 95°C range, as evaluated through the factorial experiments, seems to be related to the relatively high pitting potentials exhibited by this alloy in all the solutions tested. It is well known (Szklarska-Smialowska,1986; Cragnolino, 1987) that many metals and alloys exhibit a strong dependence of the pitting potential on temperature in the range of 25 to 150°C. The pitting potential decreases with temperature, reaching an almost constant value at even higher temperatures. The temperature range in which the pitting potential is a strong function of temperature is displaced to higher temperatures with increasing alloy resistance to pitting corrosion (Brigham, 1973). On the other hand, for a given alloy it is displaced to lower temperatures with increasing aggressiveness of the environment, as characterized, for example, by the increase in the chloride concentration. An alloy extremely resistant to pitting in a given solution exhibits a high pitting potential, in some cases unattainable within the range of stability of water as a solvent. For these highly resistant alloys, an increase in temperature or in the concentration of the aggressive species is required to promote the occurrence of pitting within the range of corrosion potentials prevailing in natural environments.

Since only a weak dependence of the pitting potential on temperature was observed in the solution containing 1000-ppm chloride, additional cyclic polarization curves were obtained in a 10,000-ppm chloride solution over the temperature range that extends from 30 to 95°C. For this purpose solutions containing 1000- and 10,000-ppm Cl^- with the addition of 20-ppm SO_4^{2-}, 10-ppm NO_3^-, 2-ppm F^-, 88-ppm HCO_3^- and Na^+ as a single cation were used to study the effect of temperature on the pitting and repassivation potentials. The results are summarized in Figure 5-11 where E_p and E_{rp} are plotted as a function of temperature for both chloride concentrations. The lines in the figure are linear regression fits. Both E_p and E_{rp} decreased with temperature with approximately the same slope for the 10,000-ppm chloride solution. The extremely weak dependence of E_p with temperature was confirmed for the 1000-ppm chloride solution. In this solution, E_{rp} also decreases with temperature but with a less pronounced slope than in the more concentrated chloride solution.

From this analysis, alloy 825 in the 1000-ppm chloride solution is concluded to be in the upper plateau region of the pitting potential vs. temperature curve, showing a behavior characteristic of a material with a relatively high resistance to pitting corrosion (Brigham, 1973). This conclusion explains the lack of temperature dependence observed by other authors (Glass,1984; Beavers, 1990) in solutions containing low chloride concentrations. In a more aggressive solution, such as that containing 10,000-ppm chloride, the pitting potential lies in the transition region where the dependence on temperature becomes dominant. The repassivation potentials, however, are quite low despite the relatively high pitting potentials measured at 95°C, even in the solution containing 1000-ppm chloride. The repassivation potential in the 10,000-ppm chloride solution at 95°C was -343 mV, which was close to the open-circuit potential measured in the deaerated solution. These results indicate that further studies are needed to evaluate the susceptibility to localized corrosion under potentiostatic conditions over the potential range that extends from E_{rp} to E_p. Results of these studies will be compared to those obtained under free corroding conditions that may be present in the repository environment.
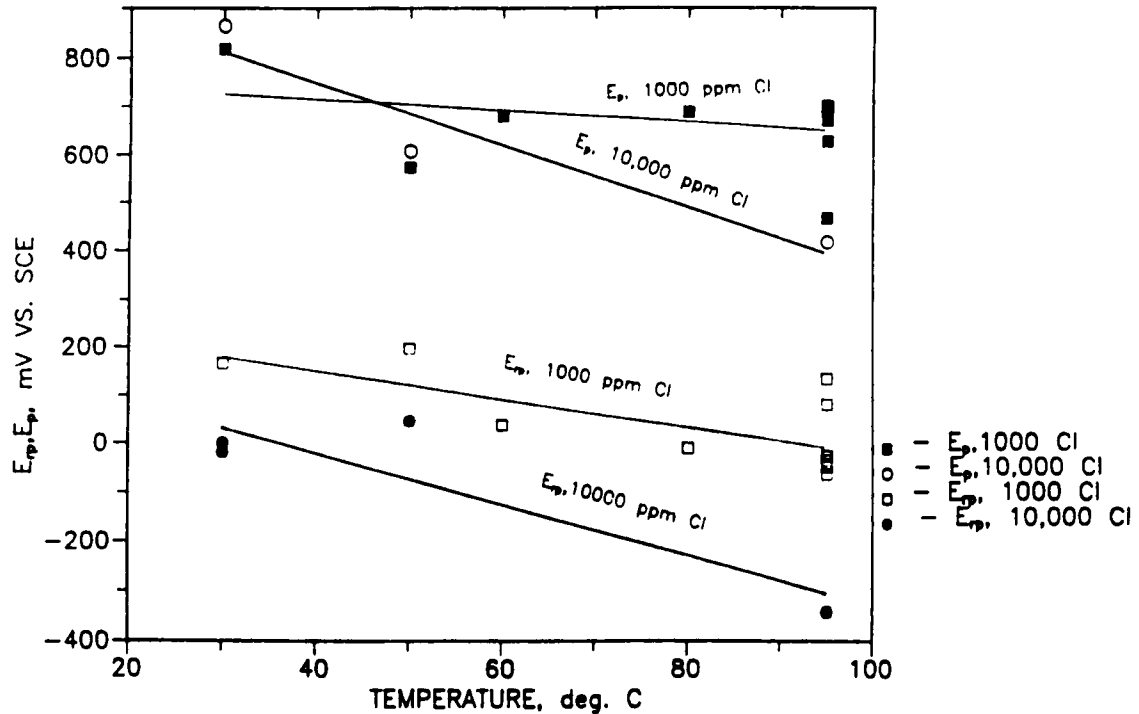
Figure 5-11. Effect of temperature and chloride concentration on E_p and E_{rp} of alloy 825

5.2.2 Summary

The focus of the investigations reported in this quarter was the response of alloy 825 to cyclic polarization as a function of environmental variables. These electrochemical studies indicate that:

(1) In the factorial experiments, especially in low chloride solutions, no correlation existed between the electrochemical parameters and visual evidence of localized corrosion. Using only the electrochemical parameters will result in a statistical analysis that is physically meaningless. Hence, a Localized Corrosion Index = Visual Rating * $(E_p - E_{rp})$ was used to analyze the results. Using this approach, a good fit between the experimentally observed values and those predicted by the statistical model was obtained ($R^2 = 0.993$).

(2) The analysis of the factorial experiments indicated that chloride is a promoter of localized corrosion; nitrate is an inhibitor of localized corrosion; and chloride and nitrate have a major interaction, i.e., nitrate is an effective inhibitor when the chloride level is high. The inhibitive effect of nitrate was found only above a concentration of 100 ppm. Fluoride was found to be an inhibitor of localized corrosion (evident mainly in the low chloride environment). Sulfate was found to be a mild promoter of localized corrosion. Temperature was found to have no significant effect within the range of temperatures studied.

(3)   In solutions with chloride concentrations ≤1000 ppm, both the pitting and repassivation potentials were relatively independent of temperature in the range of 50 to 95°C. In the 10,000-ppm chloride solution, both these potentials decreased with temperature. In the 6-ppm chloride solution, a small inverse temperature effect (greater localized corrosion with a decrease in temperature) was noted.

(4)   Considerable nonlinearity in the functional dependence of LCI on chloride was noted. The observed values of LCI at intermediate chloride concentrations were higher than predicted by the linear regression equation.

5.3   REFERENCES

Brigham, R. J., and E. W. Tozer. 1973. Temperature as a pitting criterion. *Corrosion.* 29(1):33.

Beavers, J. A., and C. L. Durr. 1990. Container corrosion in high-level nuclear waste repositories. *First Semi-Annual Report, Year 3.* NRC Contract No. NRC-04-87-009. Columbus, Ohio: Cortest Laboratories, Inc.

CNWRA. 1990. Integrated waste package experiments. *Report on Research Activities for the Quarter April 1 through June 30, 1990.* 90-02Q. San Antonio, Texas: CNWRA: 5-1.

Cragnolino, G. A. 1987. Review of pitting corrosion in high temperature aqueous solutions. *Second International Conference on Localized Corrosion.* Houston, Texas: National Association of Corrosion Engineers (NACE), to be published.

Glass, R. S., G. E. Overturf, R. E. Garrison, and R. D. McCright. 1984. *Electrochemical Determination of the Corrosion Behavior of Candidate Alloys Proposed for Containment of High-Level Nuclear Waste in Tuff.* UCID-20174. Livermore, California: LLNL.

Leckie, H. P., and H. H. Uhlig. 1966. Environmental factors affecting the critical potential for pitting in 18-8 stainless steel. *J. of Electrochemical Society* 113 (12):1262.

Mason, R. L., R. F. Gunst, J. L. Hess. 1989. *Statistical Design & Analysis of Experiments.* New York: John Wiley and Sons.

Szklarska-Smialowska, Z. 1986. *Pitting Corrosion of Metals.* Houston, Texas: NACE.

6. STOCHASTIC ANALYSIS OF UNSATURATED FLOW AND TRANSPORT
by Rachid Ababou

Investigator: *Rachid Ababou*

6.1 TECHNICAL OBJECTIVES

A quantitative characterization of large-scale flow and radionuclide transport through the heterogeneous unsaturated fractured rock of Yucca Mountain will be necessary to evaluate compliance with the siting criteria and performance objectives associated with the proposed Yucca Mountain HLW repository (10 CFR 60.112 and 60.113). The pertinent technical issues concerning radionuclide migration at Yucca Mountain must be understood so as to demonstrate that the hydrogeologic conditions at the repository site strongly inhibit radionuclide transport to the accessible environment and meet performance criteria. Realistic modeling of the complex, heterogeneous flow and transport processes at Yucca Mountain will require incorporating the effects of relatively small-scale space-time variability in modeling large-scale unsaturated flow and radionuclide transport.

The specific objectives of the Stochastic Analysis of Unsaturated Flow and Transport Project are as follows:

- To perform a review of the literature and assess available models and data relevant to the subject site,

- To select a global approach to model large-scale flow and transport in unsaturated fractured rock,

- To develop submodels for incorporation into the global model, and

- To perform large-scale simulations and participate in the validation of flow/transport models for the Yucca Mountain repository.

The project is divided in three tasks to accomplish the objectives.

(1) Task 1 - Review, Analysis, and Initial Development of Modeling Approach

(2) Task 2 - Stochastic Submodel Development and Implementation

(3) Task 3 - Large-Scale Flow/Transport Simulation and Data Analysis

Complete results of the literature review, initial data assessment, model selection, and first stages of model development will be presented in the Technical Report for Task 1.

6.2 RESEARCH ACCOMPLISHMENTS

Three major technical areas of development were presented in the previous quarterly report: (1) three-dimensional synthetic flow experiments, (2) numerical analysis of non-

linear unsaturated flow, and (3) unsaturated coefficients and statistical correlations. The latter topic was only briefly summarized and is developed in more detail in this report. The work accomplished during this quarter focused on the initial development and assessment of conceptual "submodels" (potential components of a large-scale flow-transport model). Assuming a statistical continuum model, two types of submodels, with either fine-scale (detailed) or coarse-scale (effective) material properties, were considered. The key features of the two submodels are discussed below. The models are preliminary and will require some refinements. Also not treated explicitly here is the case of a statistical discontinuum. Fracture network submodels and effective fracture/matrix properties submodels will be fully covered at a later stage of this research (Task 2).

6.2.1 Spatial-Statistical Distributions and Correlations

If detailed modeling is deemed computationally feasible, then a key question is assigning detailed material-property distributions, including unsaturated constitutive relations, that are compatible with site-specific and other field data. This quarter focused on identifying those statistical features that are likely to play a crucial role from the point of view of hydrodynamics. Research accomplished to date indicates that, besides anisotropy due to stratification, the existence of statistical cross-correlations among certain unsaturated flow parameters can also play an important role in macroscale flow behavior. By investigating randomly generated unsaturated conductivity curves and analyzing the family of curves, the existence of a crossing point at a critical pressure as well as the existence of an upper envelope has been established. In order not to obscure the present report with mathematical calculations, preliminary technical aspects of this research are given in Appendix A. Applications of similar concepts for flow in fractured unsaturated rocks will be explored in the future (Task 2).

6.2.2 Anisotropic Effective Conductivity

If detailed modeling appears computationally unfeasible, then a coarser model based on effective hydrodynamic properties may have to be developed. Conceptual models of effective hydrodynamic properties have been useful in the areas of oil-reservoir simulation and contaminant hydrology. During this quarter, the relation between anisotropic effective conductivity and spatial-statistical conductivity distribution was explored for the case of a fully saturated statistical continuum (R. Ababou, 1990). Because this paper is not widely available and the conference proceedings have not yet been published, the extended abstract is made available in Appendix B. The tensorial effective conductivity model was successfully applied using saturated flow data from the fractured granite Oracle Site (Arizona). The question remains whether a similar, effective conductivity model can be developed for unsaturated fractured rocks. This will be explored in Task 2.

6.3 REFERENCES

Ababou, R. 1990. Conductivity tensor in randomly heterogeneous and stratified aquifers. Presented at the 5th Canadian-American Conference on Hydrogeology: Parameter Identification and Estimation for Aquifer and Reservoir Characterization. Calgary, Alberta, Canada (to be published).

7. GEOCHEMICAL NATURAL ANALOGS
by English C. Pearcy and William M. Murphy

Investigators: *English C. Pearcy and William M. Murphy*

7.1 TECHNICAL OBJECTIVES

The Geochemical Natural Analog Project is designed to provide knowledge of the state of the art in natural analog studies applied to contaminant transport. Within Task 1 of the project, a literature review was conducted during the third quarter of 1990. Objectives of Task 1 include: compilation and evaluation of research conducted on natural analogs relevant to contaminant transport at the candidate HLW repository at Yucca Mountain; review of literature on potential sites for a natural analog study to be undertaken; and evaluation of these sites with respect to the degree of relevance to understanding contaminant transport at Yucca Mountain, possibility of constraining initial and boundary conditions, feasibility of research at the sites, and potential usefulness for unsaturated-zone contaminant-transport model validation.

7.2 RESEARCH ACTIVITY

During this quarter, work continued on literature identification and review. A draft of the *Geochemical Natural Analog Literature Review Report* (Task 1 milestone report 20-3704-061-003) was written. A summary of that draft report comprises this quarterly report.

7.3 GEOCHEMICAL NATURAL ANALOG LITERATURE REVIEW

The HLW literature has been reviewed for applications of natural analog studies. Processes and events likely to control contaminant transport at Yucca Mountain are identified herein, and those processes which are amenable to natural analog study are discussed. A set of criteria for the successful use of natural analog studies is presented. Descriptions of candidate natural analog sites relevant to the proposed HLW repository at Yucca Mountain and discussions of their potential usefulness are included.

Natural analogs are occurrences of a material or process in nature which may be viewed as comparable to some aspect of a system of interest. In this case, the system of interest is a high-level nuclear waste repository. Natural materials that approximate components of a repository may be studied to gain a better understanding of the behavior to be expected from the repository material. Similarly, a process that occurs (or has occurred) in nature and that may be significant to the performance of a repository may be investigated to learn of possible effects on a repository system.

Natural analog studies have been used for many years. Geologists have always been limited in their investigative approaches by the physical and temporal scales of many aspects of their subject. Mountains do not fit into a laboratory and the time and forces involved in building them are not available for experiments. In many cases, therefore, the only test of a geologic hypothesis is how well it fits with observations of nature's experiments.

Consequently, it is often difficult to prove a geologic hypothesis in the same sense that hypotheses in other disciplines can be proven through rigorous duplication of experiments by many investigators. Geologists instead rely on generalizations inferred from numerous observations of analogous rocks to test their ideas; that is, they use natural analogs.

7.3.1 Uses of Natural Analogs for HLW Repository Planning

Natural analog studies are necessary in the planning of geologic HLW repositories for many of the same reasons as they are necessary to much geologic investigation. The Environmental Protection Agency (EPA) rule 40 CFR Part 191 [section 191.13(a)] specifies that HLW must be isolated from the accessible environment for a period of at least 10,000 years. The NRC rule 10 CFR Part 60 [sections 60.21(c)(1)(ii)(F) and 60.101(a)(2)] calls for use of natural analog studies to "support" analyses and models that will be used to predict future conditions and changes in the geologic setting at a repository site over the period of regulatory interest. In addition to the great length of time under consideration, a geologic nuclear waste repository will constitute a system much larger than can be approximated by laboratory facilities. By studying natural systems which have operated for times comparable to radionuclide isolation requirements and which are of similar scale to a repository, some of the uncertainty inherent in projecting such large-scale processes so far into the future can be reduced.

Public perception is a difficult problem associated with nuclear waste disposal. It has been suggested (e.g., Winograd, 1986; Papp, 1987; Vovk, 1988; Chapman and McKinley, 1990) that natural analogs may be useful in conveying to the public a sense of the long-term stability possible in a geologic environment. For example, many studies consider uranium ore deposits as natural analogs of HLW repositories. The ability of these sites to contain substantial quantities of radioactive material for periods much longer than required for HLW isolation is an appealing intuitive argument for the possibility of safe nuclear waste disposal. However, these same ore deposits may be used to make arguments for massive transport of radioactive materials over large distances by natural processes (Sargent, 1990; Apted, 1990). The substantial quantity of uranium contained in these deposits was originally dispersed throughout some larger volume. Natural processes mobilized the uranium and transported it to the site of the present deposit; so uranium ore deposits do provide implicit evidence of the element's considerable mobility in the natural environment.

7.3.2 Limitations of Natural Analog Studies

Though natural analog studies extend the sort of investigations possible in the laboratory, they have a variety of inherent limitations. Chief among these is the incompleteness of the geologic record, at any geologic analog site, of all of the processes and events important (or potentially important) to the development of the analog. The existing record also may be uninterpretable. Erosion, metamorphism, hydrothermal or meteoric alteration, and structural disruption are all processes commonly responsible for erasing portions of the geologic record. Even if a given portion of the geologic record is not erased by a later event, the overlapping effects of subsequent phenomena may make it difficult or impossible to sort out the history of the area in detail. Consequently, it is generally difficult to adequately constrain the initial and boundary conditions for specific processes within natural geologic systems. Temperatures, pressures, fluid compositions, timing of process

onset, and duration--are all examples of factors that may only be indirectly estimable. Of course, limits may always be placed, but they may be broad. Quantification of effects to the degree desired is often difficult.

No natural analogs of an entire repository system are available. A given site will only be analogous to some portion of a repository or to a subset of the processes that will occur in a repository. Additional processes also will have occurred that are not characteristic of the repository, so choices must be made as to the processes of greatest relevance and the ability to isolate them for study.

The elements and materials involved in an analog study are, by definition, approximations of the materials and elements planned for placement in a repository. The approximations may be quite close; for example, uraninite is a good analog to the bulk composition and crystal form of spent fuel (Finch and Ewing, 1989), and basaltic and rhyolitic glasses hydrate similarly to vitrified HLW (Arai et al., 1988). Almost always, however, some deviation occurs; for example, uraninite does not contain the internal phase segregations present in spent fuel, and borosilicate nuclear waste forms have compositions substantially different from basaltic or rhyolitic glass. Some technological materials (e.g., cast steel) are particularly difficult to approximate with natural materials.

The 10,000-year period required for HLW isolation is difficult to approximate with natural analogs. Most ore deposits are much older (10^6 to 10^9 years), and most anthropogenic sites are much younger (0 to 10^3 years). To make the best use of an analog investigation, the process(es) studied should have occurred over an interval of 10^3 to 10^4 years.

7.3.3 Contributions of Natural Analog Studies

The above limitations notwithstanding, natural analog studies can make critical contributions. These contributions have been summarized notably by Petit (1990a and b) from which much of the following discussion is taken. Only through the use of natural analogs can an investigator identify and confirm that a process occurs in nature as well as in a laboratory or in theory. Natural analogs allow testing of the pertinence of individual processes over geologic time and the assessment of the relative importance of various processes as they interact in nature. Analog investigations may determine the conditions under which the processes occur, the effects of the processes, and the magnitude and duration of the phenomena.

Objection to the scientific use of natural analogs based on their generally qualitative nature is inappropriate for two reasons. First, in recent years new techniques and more rigorous efforts have produced substantial quantitative data from natural analog studies. Second, the supposed pre-eminence of quantitative data over qualitative data is questionable. Although it is often implied that qualitative data are inferior to quantitative data, the choices made in setting up a mathematical model generally are made on the basis of qualitative information; and it is only after those choices are made that quantitative data are introduced in the mechanical calculations. For example, performance assessment models are typically extremely quantitative. The choices, however, of what processes and components to include in the model and the point in the model at which to insert a process are all qualitative; and it is those qualitative determinations which control the model

predictions. The qualitative basis for the construction of the models, therefore, is as important as the quantitative data input later.

Mathematical models of natural phenomena are developed through a process of iterative interaction with natural analogs and laboratory and field experiments. There is no way to directly validate long-term predictions of models with laboratory or field experiments; and given the uncertainties involved in analog studies, validation of a given model may not be possible (in a strict sense) through the use of natural analogs. Natural analogs, however, provide the only means of testing models of long-term processes for pertinence. The International Atomic Energy Agency (IAEA) definition of validation of a model is:

"A conceptual model and the computer code derived from it are 'validated' when it is confirmed that the conceptual model and the derived computer code provide a good representation of the actual processes occurring in the real system. Validation is thus carried out by comparison of calculations with field observations and experimental measurements." (IAEA, 1982)

The results of short-term, small-scale laboratory experiments, and the long-term predictions of models based on the laboratory experiments may be compared to observations of natural systems that have operated for long periods at large scales (i.e., natural analogs). At the same time, while this process of testing by comparison constitutes validation of the model, the limitations of validation by comparison must be clearly understood. The comparisons are not expected to be exact; in fact, performance assessment models are typically conservative in their predictions and therefore deliberately differ from reality. Comparison of model predictions with the results of natural analog investigations in general will permit only confirmation that the model takes into account the appropriate processes in appropriate ways. Validation of a predictive model by such comparison results in reasonable assurance that the model accurately reflects future behaviors. This is the level of confidence required by 10 CFR Part 60 section 60.101(a)(2) which reads in part:

"Proof of the future performance of [a HLW repository] over time periods of many hundreds or many thousands of years is not to be had in the ordinary sense of the word. For such long-term objectives and criteria, what is required is reasonable assurance. . . ."

Regulation 10 CFR Part 60 does not use the word "validation" or "validate" except in section 60.131(b)(7), which refers to "experiments used to validate the method of calculation" to ensure nuclear "criticality control" in handling HLW.

7.3.4 Natural Analog Studies

This section contains examples of natural analog studies relevant to contaminant transport at the candidate HLW repository at Yucca Mountain, Nevada. The compilation is not intended to be exhaustive but to give an overview of the range of analogs considered. The studies are organized according to the type of site at which the study was conducted. The natural analog examples include: ore deposits, igneous contact zones, natural glasses, nuclear explosion sites, uraniferous nodules, sediment contacts, hydrothermal systems, mine tailings, rock alteration, archaeologic sites, and uraniferous veins.

For a complete listing and description of the sites identified, the reader is referred to the Task 1 milestone report 20-3704-061-003.

7.3.5 Processes and Events Likely to Control Contaminant Transport at Yucca Mountain

Processes and events that are likely to control contaminant transport at Yucca Mountain fall into two groups: (1) those generally important at any geologic HLW repository and (2) those peculiar to Yucca Mountain. Both are presented below.

Processes Important to Contaminant Transport at Any Geologic HLW Repository. Processes likely to be important in general to contaminant transport at geologic HLW repositories include:

- Mineral/container/waste form dissolution and/or precipitation
- Aqueous speciation of repository fluids (including organic complexing and radioelement speciation)
- Colloid transport and/or retardation of waste elements
- Microbial activity (redox controls, mineral precipitation/dissolution, and formation of organic colloids)
- Matrix and intra-crystalline diffusion of elements
- Fracture flow of fluids and gases
- Matrix flow of fluids and gases
- Changes in permeability due to thermal, chemical, or physical effects
- Redox equilibration (kinetics) and redox front migration
- Chemical species and mineral phase stability, solubility and metastability
- Radiolysis
- Thermally driven elemental diffusion
- Convective (buoyancy driven) fluid movement
- Alpha recoil effects
- Adsorption
- Ion exchange
- Coprecipitation
- Dispersion
- Radioactive decay chain

Processes and Events Which Are Peculiar to Contaminant Transport at Yucca Mountain. A number of processes important to contaminant transport result from the (1) occurrence of the proposed repository at Yucca Mountain in tuffaceous host rock, (2) chemically oxidizing environment of the site, and (3) partial hydrologic saturation of the proposed repository horizon. The host tuffs contain large amounts of glass fragments which interact readily with groundwater. This interaction may take the form of elemental exchange, dissolution of the glass, or alteration of the glass or its components to new minerals. Large volumes of the tuffs underlying the repository horizon have been altered so that they contain abundant zeolites; sorption onto these zeolites is likely to impede radionuclide transport. The response of these tuffs to thermal and hydrothermal alteration may change their sorptive capacity. Mineralogic alteration of the tuffaceous host rocks may also result in volume change which, in turn, could open fractures enhancing fluid flow and

contaminant transport. The oxidizing environment at the site will (1) increase the potential for the waste forms and waste containers to degrade by oxidation, (2) determine the oxidation state of the radioelements and the phases that control their solubilities and concentrations, and (3) increase mobility of contaminant species that are more soluble in an oxidized state. The lack of hydrologic saturation at the repository level means that unsaturated fluid flow will control contaminant transport (as long as partial saturation is maintained), including vapor phase ^{14}C transport. Partial saturation also means that the hydrostatic pressure is negative, increasing the tendency for water vaporization in the presence of a thermal pulse from the waste.

7.3.6 Geochemical Processes Amenable to Natural Analog Study

All of the processes listed above are potentially amenable to analog study. Choices among them depend on which processes are considered most important to contaminant transport at the proposed repository at Yucca Mountain, and which are well exhibited at identified natural analog sites.

7.3.7 Criteria for the Successful Use of Natural Analogs

Chapman et al. (1984) presented the following criteria for selecting analogs:

(1) The process involved should be clear-cut. Other processes that may have been involved in the geochemical system should be identifiable and amenable to quantitative assessment as well so that their effects can be 'subtracted.'

(2) The chemical analogy should be good. It is not always possible to study the behavior of a mineral system, chemical element, or isotope identical to that whose behavior requires assessing. The limitations of this should be fully understood.

(3) The magnitude of the various physico-chemical parameters involved (such as P, T, pH, Eh, and concentrations) should be determinable, preferably by independent means, and should not differ greatly from those envisaged in the disposal system.

(4) The boundaries of the system should be identifiable (whether it is open or closed and, consequently, how much material has been involved in the process being studied).

(5) The time scale of the process must be measurable, since this factor is of the greatest significance (the *raison d'etre*) for a natural analog.

Airey and Ivanovich (1985) added a requirement for transport analogs:

(6) A contaminant transport analog requires a spatial discontinuity across which to observe transport.

In addition to the above criteria, it is important that

(7)   The source term (e.g., the original distribution of the elements of interest) be well constrained, and

(8)   The environmental analog be close. The argument is inappropriate that an analog has suffered more extreme conditions than the system of comparison and therefore provides a conservative example. *More extreme* conditions are *different* conditions than those present in the system of comparison; such different conditions may include different processes or different combinations of processes than those at the site of interest.

7.3.8   Potential Sites for a Natural Analog Study

The uranium ore deposit at Peña Blanca, Mexico, and the archaeologic site at Santorini, Greece, have been identified as potential sites for a natural analog study. These sites were described in the quarterly report for April 1 - June 30, 1990 (CNWRA, 1990).

Briefly, the sites at both Peña Blanca and Santorini are in the hydrologically unsaturated zone of siliceous tuff sequences, and both sites occur in climates similar to that of southern Nevada. The past and present oxidation of uraninite at Peña Blanca constitutes an analog for the alteration of spent nuclear fuel. The processes of migration of uranium and other elements from sites of initial mineralization under unsaturated, oxidizing conditions at Peña Blanca are analogous to those that would occur in the Yucca Mountain repository. Studies using buried artifacts at the Santorini archaeological site as analogs of contaminant sources would permit analyses of the rates and mechanisms of trace elemental migration in a geologic setting analogous to Yucca Mountain. The initial and boundary conditions at Santorini could be especially well defined, and the time period since burial of the artifacts (3600 years) is comparable to the period of interest in radioactive waste management.

Though Peña Blanca and Santorini provide good analogs to some processes important to HLW containment, there are no perfect analogs. The source term and boundary conditions at Peña Blanca may be difficult to constrain closely because of the complexity of the original hydrothermal systems and subsequent alteration. Conversely, at Santorini (where the source term and boundary conditions are relatively well known) the material and elemental sources are not necessarily close analogs to spent fuel or vitrified waste forms. Nevertheless, the physical similarities between these sites and Yucca Mountain could permit identification and characterization of relevant waste form degradation and contaminant migration phenomena, and could aid in the development and validation of predictive models for performance assessments.

7.4   REFERENCES

Airey, P. L., and M. Ivanovich. 1985. Geochemical analogs of high level radioactive waste repositories. B. Come and N. Chapman, eds. *Commission of the European Communities Natural Analog Working Group, First Meeting.* Brussels: Commission of the European Communities (CEC).

Apted, M. J. 1990. Natural analogues for the predictive reliability of the engineered barrier system for high-level waste. *Fourth Natural Analogue Working Group Meeting, Pitlochry, Scotland, 18-22 June 1990, Final Meeting Report Pre-Print.* Brussels: CEC, n° EUR 13014 EN.

Arai, T., Y. Yusa, N. Sasaki, N. Tsunoda, and H. Takano. 1988. Natural analogue study of volcanic glass - a case study of basaltic glasses in pyroclastic fall deposits of Fuji Volcano, Japan. *Scientific Basis for Nuclear Waste Management XII - Materials Research Society Symposium Proceedings.* Pittsburgh: Materials Research Society: 73-80.

Chapman, N., and I. McKinley. 1990. Radioactive waste: back to the future? *New Scientist:* 54-58.

Chapman, N. A., I. G. McKinley, and J. A. T. Smellie. 1984. The potential of natural analogues in assessing systems for deep disposal of high-level radioactive waste. Swedish Nuclear Fuel and Waste Management Co. (SKB) and the Swiss Radioactive Waste Cooperative (NAGRA). NTB 84-41. KBS 84-16. Eir Ber 545.

CNWRA. 1990. *Report on Research Activities for the Quarter April 1 Through June 30, 1990.* 90-02Q. San Antonio, Texas: CNWRA.

Finch, R. J., and R. C. Ewing. 1989. Alteration of natural UO_2 under oxidizing conditions from Shinkolobwe, Katanga, Zaire: a natural analogue for the corrosion of spent fuel. Swedish Nuclear Fuel and Waste Management Company (SKB). Technical Report 89-37.

IAEA, 1982. Radioactive waste management glossary. IAEA Report IAEA-TECDOC-264.

Papp, T. 1987. The role of natural analogues in safety assessment and acceptability. B. Come and N. Chapman, eds. *Commission of the European Communities Natural Analogues in Radioactive Waste Disposal - A Symposium.* Brussels: CEC.

Petit, J. 1990. Reasoning by analogy (rational foundation of natural analogue studies). *Applied Geochemistry,* in press.

Petit, J. 1990. Design and performance assessment of radioactive waste forms: what can we learn from natural analogues? *Fourth Natural Analogue Working Group Meeting, Pitlochry, Scotland, 18-22 June 1990, Final Meeting Report Pre-Print.* Brussels: Commission of the European Communities: n° EUR 13014 EN.

Sargent, F. P. 1985. What can the earth scientists provide? B. Come and N. Chapman, eds. *Commission of the European Communities Natural Analogue Working Group, First Meeting.* Brussels: CEC:105-111.

Vovk, I. F. 1988. The IAEA report of the role of natural analogues in performance assessment. B. Come and N. Chapman, eds. *Commission of the European Communities Natural Analogue Working Group, Third Meeting.* Snowbird, Utah: CEC:140-144.

Winograd, I. J. 1986. Archaeology and public perception of a trans-scientific problem: disposal of toxic wastes in the unsaturated zone. U.S. Geological Survey. Open-file Report 86-136.

APPENDIX A

**Fine-Scale Spatial-Statistical Distributions and Correlations:
Effects of Cross-Correlations Between Intercept
and Slope of Unsaturated Log-Conductivity Field**

by R. Ababou

Fine-Scale Spatial-Statistical Distributions and Correlations: Effects of Cross-Correlations Between Intercept and Slope of Unsaturated Log-Conductivity Field

1. Introduction

In the statistical continuum approach to geologic heterogeneity, the geologic formation is assumed to behave like a porous continuum (porous medium). A detailed, fine-scale model of continuum heterogeneity can be obtained by representing each hydrodynamic parameter in the form of a random field. Both single- realization approaches (Ababou et al., 1989) and multiple Monte-Carlo realizations (Smith and Freeze, 1979) have been used in the context of saturated groundwater flow. Single-realization approaches for unsaturated flow were implemented in three dimensions by Ababou and Gelhar (1988) and in one dimensions by Yeh (1989). Multiple Monte-Carlo realizations of one-dimensional unsaturated flow, with only the saturated conductivity as random field, were used by Andersson and Shapiro (1983). In contrast, Ababou (1988, Chap. 7) and Yeh (1989) considered the case where the entire curve of unsaturated conductivity versus pressure varies randomly in space. This idea of a spatially variable nonlinear conductivity was implemented by assigning random field properties to both K_s, the saturated conductivity, and α, the slope of the curve relating log-conductivity to pressure.

The three-dimensional single-realization numerical experiments of Ababou (1988, Chap. 7) indicate that even a moderate coefficient of variation in the α-parameter can create highly heterogeneous moisture patterns. In addition, comparing the cases of perfectly correlated and perfectly uncorrelated Ks and α, Ababou (1988) found a significant sensitivity of flow heterogeneity to (Ks, α) cross-correlation. The most heterogeneous moisture patterns were obtained in the uncorrelated case. A similar conclusion was reached by Yeh (1989) based on more detailed one-dimension comparisons of the perfectly correlated and uncorrelated cases.

The purpose of this note is to elucidate and quantify analytically some of the cross-correlation effects uncovered by Ababou (1988, Chap. 7) and Yeh (1989), and to extend their analyses to the general case of imperfect cross-correlation between the saturated conductivity and slope of the unsaturated log-conductivity curve. The contribution is two-fold: (i) provide a parsimonious analytical model of spatially random unsaturated conductivity curves subject to correlation between intercept and slope; and (ii) provide a compact analytical characterization of heterogeneous unsaturated flow processes in relation to cross-correlations among hydraulic conductivity parameters. The first point is the object of the next section. The second point will be briefly summarized in the remaining section.

2. Random Field Model of Unsaturated Conductivity Curve with Imperfect Cross-Correlation

The present random field model of unsaturated conductivity is an extension of the one previously used in analytical and numerical studies of stochastic unsaturated flow (Mantoglou and Gelhar, 1987 a.b.c.; Yeh et al., 1985 a.b.c.; Ababou, 1988; and Yeh, 1989). Let h designate the water pressure head, and $\Psi = -h$ the suction head. As in the above-mentioned references, the spatially random nonlinear unsaturated conductivity is assumed to be of the form:

$$K(\Psi, x) = K_s(x) \exp(-\alpha(x)\Psi) \tag{1}$$

where the saturated conductivity $K_s(x)$ and the "slope" parameter $\alpha(x)$ are each spatially correlated random functions of space, i.e. random fields. Unlike the above-mentioned references, the cross-correlation between these parameters is modeled explicitly here.

First, the random unsaturated conductivity model (1) is expressed equivalently in terms of log-conductivity as follows:

$$Y(\Psi,x) = F(x) - \exp(A(x)) \, \Psi \tag{2}$$

where Y is the unsaturated log-conductivity:

$$Y(\Psi,x) = \ell n \, K(\Psi,x) \tag{3}$$

and all other quantities are as defined previously. The log-conductivity model given by equation (2) possesses two important features. First the unsaturated log-conductivities are linear functions of suction (Ψ), with random intercept (F) and random slope ($\exp(A)$) at each point in space. Secondly, since the slope of the unsaturated log-conductivity curve is given by $\exp(A)$, the slope is log-normally distributed and can never take negative values. This is in accordance with the intuitively reasonable requisite that conductivity must always decrease in a drying porous medium.

To complete the model (1)-(2)-(3), the two-point correlations and cross-correlations of the jointly gaussian random fields (F(x), A(x)) must still be specified. A special form of jointly gaussian random fields is selected that reduces the number of statistical parameters while retaining crucial features, spatial correlations and cross-correlations, as previously suggested in Ababou (1988, Chap. 7, eq.(7.7)). First, let:

$$F(x) = \bar{F} + f(x) \tag{4a}$$
$$A(x) = \bar{A} + a(x) \tag{4b}$$

where $(\bar{F},\bar{A})$ are the means and (f, a) the zero-mean perturbations of the random fields (F,A). The proposed simplified model is obtained by choosing a(x) to be a linear combination of two independent replicates of f(x). Let u(x) be a normally distributed zero-mean unit-variance random

field. Assign to u(x) the observed correlation structure of f(x). Then, construct f(x) and a(x) from two independent replicates $u_1(x)$ and $u_2(x)$ of u(x), as shown below:

$$F(x) = \sigma_f u_1(x) \tag{5a}$$

$$a(x) = \sigma_a(\rho u_1(x) + \sqrt{1-\rho^2}\ u_2(x)) \tag{5b}$$

Thus, (a,f) have the desired jointly gaussian distribution and correlation structure, and the coefficient ϱ uniquely characterizes the cross-correlation between the two random fields a(x) and f(x) (note: $-1 \leq \varrho \leq +1$).

In the forthcoming sections, a statistical characterization of the family of unsaturated log-conductivity curves $Y(\Psi, x)$ based on the previously defined model is developed. This model can capture complex features like three-dimensional anisotropic heterogeneity, and can take into account the often observed fact that coarser materials, with large K_s, experience a faster decrease of conductivity as they desaturate. The goal is to analyze the role of this phenomenon, represented by the cross-correlation parameter ϱ in naturally heterogeneous porous media.

3. Mean and Effective Unsaturated Conductivity Curves

Various types of mean unsaturated conductivity curves are computed by taking averages over the ensemble of random unsaturated conductivity curves. First, the geometric mean unsaturated conductivity curve, $K_G(\Psi)$, is obtained by computing the arithmetic mean of the log-conductivity curve (5) as follows:

$$\ln K_G(\Psi) = \ <Y(\Psi,x)> \ = \ln K_G - \alpha_G \exp(\sigma_A^2/2)\ \Psi \tag{6}$$

The first equality is an identity, and the second equality follows by taking the average of eq. (5) and taking into account the following identities:

$$<u_1> \ = \ <u_2> \ = \ <u_1 u_2> \ = 0 \tag{7a}$$

$$a = \sigma_A(\rho u_1 + \sqrt{1-\rho 2}\ u_2) \tag{7b}$$

$$<a> \ = 0; \quad <\exp(a)> \ = \exp(\sigma_A^2/2) \tag{7c}$$

More generally, other types of means conductivity curves, including arithmetic and harmonic means, can be computed based on power averaging formulas similar to those given by Ababou and Wood (1990). Without going into details, the reasons for investigating the power average conductivity can be explained as follows. The power average unsaturated conductivity $K(\Psi) = \ <K(\Psi,x)^p>^{1/p}$ can be used as a surrogate for the effective macroscale conductivity of quasi-steady unsaturated flow systems. Thus, in a distinctly stratified formation, the arithmetic mean (p = +1), is a surrogate for effective conductivity parallel to bedding, and the harmonic mean (p = -1) is a

surrogate for effective conductivity orthogonal to bedding. This idea is analogous to previously advocated models of unsaturated soil anisotropy (Zaslavasky and Sinai, 1981; Mualem, 1984). The geometric mean unsaturated conductivity (p = 0) can be viewed as a surrogate for effective conductivity in a non-stratified, structurally isotropic unsaturated formation.

It should be recognized, however, that computing the true effective conductivity for the macroscale unsaturated Darcy equation requires taking into account three-dimensional interactions between conductivity fluctuations and pressure gradient fluctuations. Interpreting arithmetic/harmonic mean conductivities as parallel/orthogonal effective conductivities can only be a rough "zero-order" approximation (whence the term "surrogate").

Computing the power-average conductivity as a function of suction revealed the possible effects of the cross-correlation coefficient ϱ on the (surrogate) effective conductivity of unsaturated geologic formations. First, in the case of structurally isotropic geologic formations, the effective conductivity (geometric mean p = 0) is equal to:

$$K(\Psi) = <K(\Psi,x)^P>^{1/P} \tag{8}$$

$$K(\Psi) \approx K_G(\Psi) \approx K_G(0)\exp\{-\alpha_G\exp/\alpha_A^2/_2)\Psi\} \tag{9}$$

Therefore, the effective conductivity does not depend on the cross-correlation coefficient ϱ in structurally isotropic media.

Second, in the case of structurally anisotropic stratified formations, the parallel (x) and orthogonal (z) effective conductivities are given by the arithmetic (p = +1) and harmonic (p = -1) means. These are of the form:

$$K_x(\Psi) \approx K_A(\Psi) \approx K_x(0) \exp\{-\alpha_x(\Psi) \Psi\} \tag{10a}$$

$$K_z(\Psi) \approx K_H(\Psi) \approx K_z(0)\exp\{-\alpha_z(\Psi) \Psi\} \tag{10b}$$

Finally, equations (10) can be used for computing an "effective" anisotropy ratio, namely:

$$\frac{K_x(\psi)}{K_z(\psi)} \approx \exp(+\sigma_F^2) \cdot \exp \{+ \alpha_G \exp(\sigma_A^2/2) \Psi (\sigma_A^2\alpha_G\Psi - 2\rho\sigma_A\sigma_F)\} \tag{11}$$

In view of eqs. (10)-(11), it appears that:

- The slopes of the parallel and orthogonal effective conductivity components, $\hat{\alpha}_z(\Psi)$ and $\hat{\alpha}_x(\Psi)$, both vary linearly with suction;

- The slope of the parallel effective conductivity, $\hat{\alpha}_x(\Psi)$, decreases as suction increases; this tends to encourage parallel flow at larger suctions;

- The slope of the orthogonal effective conductivity, $\hat{\alpha}_z(\Psi)$, increases with suction; this tends to block orthogonal flow at larger suctions;

- In the case of positive cross-correlation ($\varrho > 0$) the parallel/orthogonal anisotropy ratio increases with suction above a critical value ($\Psi > \Psi_c$), reaches a minimum at $\Psi = \Psi_c$, and decreases with suction below the critical value ($\Psi < \Psi_c$).

The critical suction corresponding to the minimum "effective" anisotropy ratio is easily obtained from eq. (11). It is given by:

$$\alpha_G \Psi_c = \rho \frac{\sigma_F}{\sigma_A} \tag{12}$$

In summary, a simplified model of spatially random unsaturated conductivity curves has been developed, and the special role played by the cross-correlation coefficient in anisotropic flow behavior has been indicated.

4. Statistical Characterization of the Intersecting Set of Unsaturated Conductivity Curves

In addition to the previous analysis, it has been shown that the critical suction Ψ_c of the effective anisotropy ratio, developed above, is in fact related to the density of intersections of the set of conductivity curves $K(\Psi,x)$. This is schematically illustrated by Figure 1. In addition, the set of curves possesses an upper envelope $K_{\text{sup}}(\Psi)$. This part of the research is currently being finalized. The combined results of the previous sections and the forthcoming statistical analysis will allow establishment of a direct link between the properties of intersecting sets of conductivity curves and the nonlinear effective conductivity behavior of highly heterogeneous unsaturated flow systems at the large scale. The model appears tractable enough to be considered as a potential candidate submodel for large-scale numerical flow modeling, possibly in a more refined and general form. Applications of similar ideas for unsaturated fractured media will also be explored along with single fracture models and fracture network models.

5. Preliminary Conclusions

The main conclusion at this point is that the unsaturated flow pattern may be quite sensitive to the assumed cross-correlation between intercept and slope of the unsaturated log-conductivity curve. This sensitivity is most apparent in the case of highly stratified formations, as it implies

a significant change in the behavior of the "effective" conductivity anistropy ratio with respect to suction. These preliminary findings need to be further confirmed by simulations and field data analyses. They indicate the importance of hydrodynamic characterization of the whole unsaturated conductivity curve, and of the degree of correlation between saturated conductivity and slope of the unsaturated conductivity curve, in the case of heterogeneous and/or stratified geologic media.

Anisotropy Ratio Versus Suction

Axz

Psi
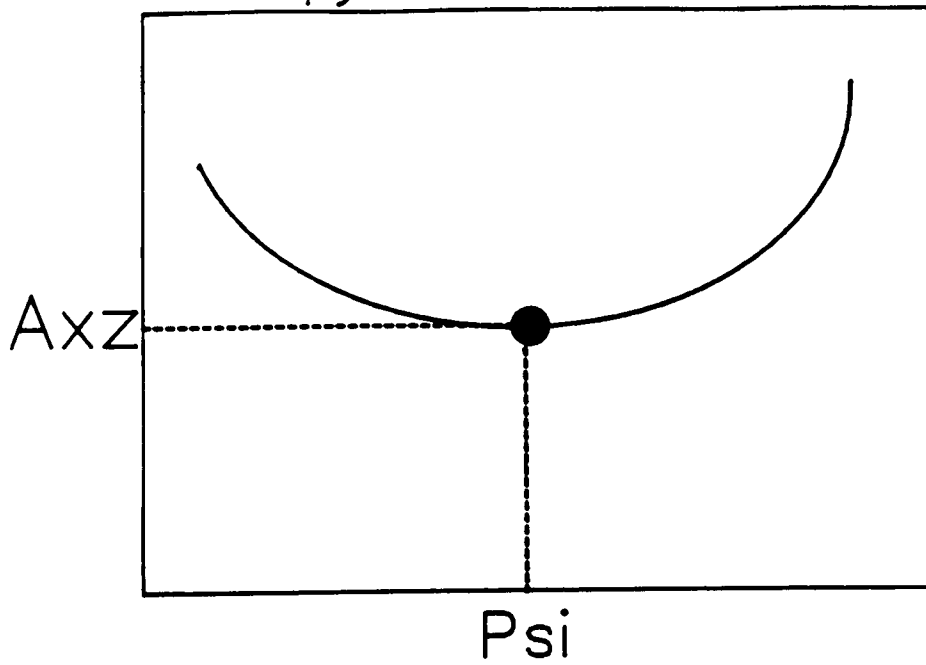
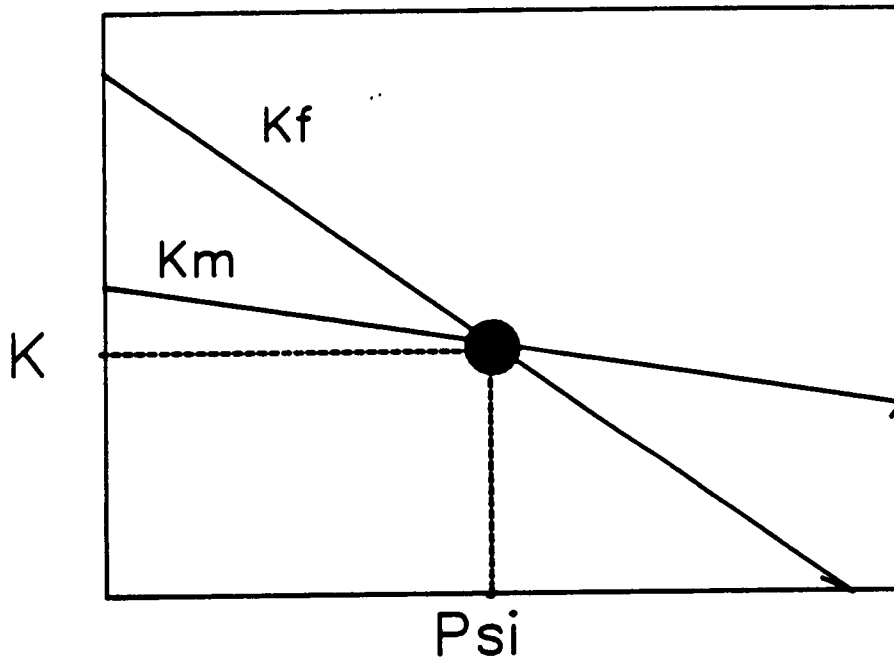# Conductivities Versus Suction

Kf

Km

K

Psi

Figure A-1.   Schematic representation of the critical suction in a heterogeneous or fractured unsaturated geologic medium: local minimum of effective anisotropy ratio (top); and intersection of conductivity curves (bottom).

References

Ababou, R. January 1988. Three-dimensional flow in random porous media. *PhD Thesis.*Department of Civil Engineering, Massachusetts Institute of Technology, Cambridge, Massachusetts, January 1988, 2 vols., 833 pp.

Ababou, R. and L. W. Gelhar. June 1988. A high-resolution finite difference simulator for 3D unsaturated flow in heterogenous media. *Computational Methods in Water Resources.* Elsevier and Computational Mechanics Publications. VOl. 1. 173-178.

Ababou, R.,D. McLaughlin, L. W. Gelhar and A. F. Tompson. 1989. Numerical simulation of three dimensional saturated flow in randomly heterogeneous porous media. *Transport in Porous Media.*, 4, 549-565.

Ababou, R. and E. F. Wood. Comment on "Effective Groundwater Model Parameter Values: Influence of Spatial Variability of Hydraulic Conductivity, Leakance, and Recharge" by J. Gomez-Hernandez and S. Gorelick, *Water Resources Research*, 26(8), 1843-1846.

Anderson, J. and A. M. Shapiro. 1983. Stochastic analysis of one-dimensional steady state unsaturated flow: a comparison of Monte-Carlo and perturbation methods. *Water Resources Research.* 19(1): 121-133.

Mantoglou, A. and L. W. Gelhar. 1987(a). Stochastic modeling of large-scale transient unsaturated flow systems. *Water Resources Research.* 23(1): 37-46.

Mantoglou, A. and L. W. Gelhar. 1987(b). Capillary tension head variance, mean soil moisture content, and effective specific soil moisture capacity of transient unsaturated flow in stratified soils. *Water Resources Research.* 23(1): 47-56.

Mantoglou, A. and L. W. Gelhar. 1987(c). Effective hydraulic conductivities of transient unsaturated flow in stratified soils. *Water Resources Research.* 23(1): 57-67.

Mualem, Y. 1984. Anisotropy of Unsaturated Soils, Soil Sci. Soc. Am. J., 48: 505-509.

Smith, L. and R. A. Freeze. 1979. Stochastic analysis of steady state groundwater flow in a bounded domain, 1: one-dimensional simulations. *Water Resources Research.* 15(3): 521-528.

Smith, L. and R. A. Freeze. 1979. Stochastic analysis of steady state groundwater flow in a bounded domain, 2: two-dimensional simulations. *Water Resources Research.* 15(6): 1543-1559.

Yeh, T. C. 1989. One-dimensional steady state infiltration in heterogeneous soils. *Water Resources Research.* 25(10): 2149-21.

Yeh, T.C., L. W. Gelhar and A. L. Gutjhar. 1985(a). Stochastic analysis of unsaturated flow in heterogenous soils: (1) statistically anisotropic media. *Water Resources Research.* 21(4): 447-456.

Yeh, T.C., Gelhar, L.W. and Gutjar, A. L. 1985(b). Stochastic Analysis of Unsaturated Flow in Hetergeneous Soils: (2) Statistically Anisotropic Media with Variable α, *Water Resources Research* 21(4): 457-464.

Yeh, T.C., L. W. Gelhar and A. L. Gutjar. 1985. Stochastic analysis of unsaturated flow in heterogeneous soils: (3): observations and applications. *Water Resources Research.* 21(4): 465-471.

Zaslavasky, D. and G. Sinai. Surface hydrology: III-causes of lateral flow. *J. Hydraulic Div.* ASCE, 107 (HYI): 37-52.

APPENDIX B

Identification of Effective Conductivity Tensor in Randomly Heterogeneous and Stratified Aquifers

by R. Ababou

IDENTIFICATION OF EFFECTIVE CONDUCTIVITY TENSOR

IN RANDOMLY HETEROGENEOUS AND STRATIFIED AQUIFERS[1]

Rachid Ababou

Southwest Research Institute,
Center for Nuclear Waste Regulatory Analyses,
San Antonio, Texas 78228, U.S.A.

EXTENDED ABSTRACT:

The effective macroscale hydraulic conductivity of heterogeneous and stratified geologic formations can be identified by ad hoc inverse methods, or by more generic, direct methods such as homogenization. Proposed here is a direct approach based on a simple homogenization relation expressing the effective conductivity tensor of randomly heterogeneous flow systems under certain conditions of statistical homogeneity and statistical anisotropy, given the microscale conductivity field $K(x_1,x_2,x_3)$. Imperfectly stratified and anisotropic geologic structures are described by means of directional fluctuation scales, while other features such as degree of variability, bimodality, etc, are conveyed by a probability distribution. The dimensionality of the flow system is also an important factor. Discussed below is the general case of a D-dimensional flow system (D = 1, 2, or 3).

The proposed homogenization relation expresses the principal components of the D-dimensional effective conductivity tensor by means of a tensorial power-average operator:

$$K_{ii} = \left\langle K^{p_i} \right\rangle^{1/p_i} \quad (i=1,...,D) \tag{1}$$

where the angular brackets < > designate the operation of averaging. In this equation, the p_i's are directional averaging exponents. They are expressed in terms of the directional fluctuation scales ℓ_i, as follows:

$$P_i = \frac{2}{D}\frac{\ell_H}{\ell_i} \qquad (i=1,...,D) \qquad (2)$$

Where ℓ_H is the D-dimensional harmonic mean fluctuation scale:

$$\ell_H = \left[\frac{1}{D}\sum_{i=1}^{i=D}\ell_i^{-1}\right]^{-1} \qquad (3)$$

Note that the averaging exponents are constrained to lie within the interval $[-1,+1]$, and that they sum up to D-2. To summarize, equations (1)-(3) give an analytical relationship for the D-dimensional effective conductivity tensor in terms of the single-point probability distribution, the principal directions, and the directional fluctuation scales of the microscale log-conductivity field. Note that the microscale data required for implementation of equations (1)-(3) are all of a statistical nature. For technical reasons, the statistics of log-conductivity rather than conductivity are preferred.

The power-average effective conductivity tensor (1)-(3) can be expressed in closed form for several usual types of log-conductivity distributions, such as gaussian, binary, etc. In the case of a "gaussian medium" with normally distributed ℓnK, applying equations (1)-(3) leads to:

$$\hat{K}_{ii} = K_g \exp\left\{\frac{\sigma_y^2}{2}\left[1-\frac{2}{D}\frac{\ell_H}{\ell_i}\right]\right\} \qquad (i=1,...,D) \qquad (4)$$

when σ_y^2 is the log-conductivity variance, and K_g is the geometric mean conductivity. This relation was initially developed by Ababou (1988, Vol. 1, Eq. 4.48) in the equivalent form:

$$\hat{K}_{ii} = (K_a)^{\alpha_i}(K_h)^{1-\alpha_i} \qquad (i=1,...,D) \qquad (5)$$

where $\alpha_i = D -(\ell_H/\ell_i)/D$, and K_a and K_h represent the arithmetic and harmonic mean conductivities, respectively. Another case of interest is that of a binary medium, made up of a mixture of two distinct conductive phases α and β, present in the proportions (ρ) and (1-ρ) respectively. For instance, phase α could be a sandstone matrix, and phase β a set of shale lenses or shale clast inclusions (Desbarats 1987, Bachu and Cuthiell 1990). The conductivity distribution of such a composite medium is of the form:

$$\text{Prob} \{K(x_1,x_2,x_3)=K_\alpha\} = \rho$$
$$\text{Prob} \{K(x_1,x_2,x_3)=K_\beta\} = 1-\rho \qquad (6)$$

As before, it is assumed that as a first approximation the spatial anisotropy of the random structure can be defined by three fluctuation scales ℓ_1,ℓ_2,ℓ_3. Specializing equations (1)-(3) for the binary distribution (6) gives:

$$\hat{K}_{ii} = \{\rho K_\alpha^{p_i}+(1-\rho)K_\beta^{p_i}\}^{1/p_i} \qquad (i=1,...,D) \qquad (7)$$

with averaging powers (p_i) are as given previously in equation (2). In the case of a three-dimensional isotropic binary medium, let $D = 3$ and $\ell_1 = \ell_2 = \ell_3$. This yields $p_i = 1/3$ ($i=1,2,3$) in equation (7). In the case of a two-dimensional isotropic binary medium, let $\ell_1 = \ell_2$ for horizontal isotropy, and $D = 2$ for restriction to two-dimensional space, or equivalently $D = 3$ with $\ell_3 \rightarrow +\infty$ for two-dimensional horizontal flow through a vertically homogeneous medium. Either case yields $p_i \rightarrow 0$ for $i = 1$ and 2. Inserting this in (7) and using Taylor developments leads to:

$$\hat{K}_{ii}=(K_\alpha)^\rho (K_\beta)^{1-\rho} \qquad (i=1 \text{ and } 2) \qquad (8)$$

where ρ represents the concentration of phase α, and $1-\rho$ the concentration of phase β.

Although the general form of the effective conductivity model (1)-(3) remains conjectural at this stage, many specialized forms of this relation appear to be confirmed by other results. The range of validity of the model is being explored in several ways: (1) by comparison with exact bounds and with available homogenization solutions in cases of lower dimensionality, statistical isotropy, symmetric distribution, binary distribution, etc; (2) by comparison with analytical solutions based on linearized and/or perturbation approximations; and (3) by comparison with direct numerical simulations of flow in randomly heterogeneous porous media. The preliminary results of such analyses are encouraging. Some of the relevant effective conductivity results used for comparisons can be found in Ababou (1988), Ababou et al. (1989), Desbarats (1987), Gelhar and Axness (1983), Kohler and Papanicolaou (1982), and Matheron (1967), among others.

Finally, some of the possible applications of the tensorial power-average conductivity model in the area of parameter estimation are briefly indicated. First, the model can be used as a convenient tool for direct identification of the effective conductivity tensor, given reasonable estimates of the microscale conductivity distribution, principal axes, and fluctuation scales. Unlike other approaches to inverse problems, the present approach does not require numerical procedures. Furthermore, the model can also be used to estimate geostatistical parameters from large-scale flow tests. To illustrate this second type of application, a parameter identification procedure previously developed for the Oracle fractured granite site by Neuman and Depner (1988)

was implemented. Their goal was to estimate the conductivity correlation scales (which play an important role in contaminant macrodispersion) based on a combination of "microscale" single-hole packer tests and "macroscale" cross-hole tests. The principal axes of macroscale anisotropy, as inferred from the cross-hole data, appeared to be directly related to the orientations of major fracture sets. Now, given the measured macroscale conductivity tensor and an independent estimate of vertical correlation scale, the remaining correlation scales of the Oracle site can be identified by inverting the effective conductivity model (1)-(3). Again, this is feasible without recourse to numerical optimization procedures.

SELECTED REFERENCES:

Ababou, R. January 1988. Three-dimensional flow in random porous Media. *PhD thesis*. Ralph Parsons Laboratory, Massachusetts Institute of Technology, Cambridge, Massachusetts, 2 Volumes, 833 pp.

Ababou, R., D. McLaughlin, L. W. Gelhar, and A. F. Tompson. 1989. Numerical simulation of three-dimensional saturated flow in randomly heterogeneous porous media. *Transport in Porous Media*. 4: 549-565.

Bachu, S. and D. Cuthiell. 1990. Effects of core-scale heterogeneity on steady-state and transient fluid flow in porous media: numerical analysis. *Water Resources Research*. 26(5), 863-874.

Desbarats, A. J. 1987. Numerical estimation of effective permeability in sand-shale formations. *Water Resources Research*. 23(2), 273-286.

Gelhar, L. W. and C. L. Axness. 1983. Three dimensional stochastic analysis of macrodispersion in aquifers. *Water Resources Research*. 19(1), 161-180 pp.

Kohler, W. and G. C. Papanicolaou. 1982. Bounds for the effective conductivity of random media, pp. 111-130, in *Macroscopic Properties of Disordered Media*. Lecture Notes in Physics, No. 154, Springer-Verlag, 307 pp.

Matheron, G. 1967. *Eléments Pour un Théorie des Milieux Poreux*. Masson et Cie, Paris, 164 pp.

Neuman, S. P. and J. S. Depner. 1988. Use of variable-scale pressure test data to estimate the log hydraulic conductivity covariance and dispersivity of fractured granites near Oracle, Arizona. *Journal of Hydrology*. 102, 475-501.